The effect of microstructural inertia on plastic localization and void growth in porous solids

N. Hosseini[a], T. Virazels[a], N. Jacques[b], J. A. Rodríguez-Martínez[a,*]

[a] *Department of Continuum Mechanics and Structural Analysis. University Carlos III of Madrid. Avda. de la Universidad, 30. 28911 Leganés, Madrid, Spain*

[b] *ENSTA Bretagne, CNRS UMR 6027, IRDL, 2 rue Francois Verny, F-29806, Cedex 9 Brest, France*

Abstract

This paper investigates the impact of microinertia on plastic localization, void growth, and coalescence in ductile porous materials subjected to high strain rates. For that purpose, we have performed finite element calculations on a flat double-notched specimen subjected to dynamic plane strain tension. The simulations employ three distinct approaches to model the mechanical behavior of the porous aggregate: (1) discrete voids within a matrix material governed by von Mises plasticity; (2) homogenized porosity represented using standard quasi-static Gurson-Tvergaard plasticity; and (3) homogenized porosity described with Gurson-Tvergaard plasticity extended by Molinari and Mercier (2001) to account for microinertia effects. The porous microstructures used in the simulations are representative of additive manufactured metals, featuring initial void volume fractions varying between 0.5% and 4%, and pore diameters ranging from 30 μm to 150 μm (Marvi-Mashhadi et al., 2021; Nieto-Fuentes et al., 2023). The applied tensile velocities ranged from 100 m/s to 1000 m/s, producing strain rates between 10^5 s^{-1} and 10^6 s^{-1}, and stress triaxiality values spanning from 4 to 30. The simulations with discrete voids validate the calculations performed using homogenized porosity and microinertia effects, demonstrating that higher strain rates and larger pore sizes lead to slower void growth and a delayed, regularized plastic localization. Conversely, the standard Gurson-Tvergaard model shows notable mesh sensitivity and fails to describe the influence of the loading rate on plastic localization. Ultimately, the comparison between finite element models with discrete voids and those with homogenized porosity illustrates the stabilizing effects of porous microstructure and multiscale inertia on dynamic plastic flow, while also highlighting the strengths of the constitutive model introduced by Molinari and Mercier (2001) for simulating engineering problems involving porous ductile materials subjected to high-velocity impacts.

Keywords:

Microstructural inertia, Porous solids, Void growth, Plastic localization, Ductile failure, Finite element simulations

1. Introduction

Ductile fracture is a prevalent mode of failure observed in materials that have the capacity for substantial plastic deformation, shear banding, or necking before eventually undergoing cracking or complete fracture (Needleman, 1972; Needleman and Rice, 1978; Needleman and Tvergaard, 1984; Tekoğlu et al., 2015; Vaz-Romero et al., 2016). The pioneering experimental studies by Rogers (1960), Beachem (1963), and Gurland and Plateau (1963) were the first

*Corresponding author. Tel. +34916249904. E-mail address:jarmarti@ing.uc3m.es

to document that this type of fracture occurs due to the nucleation, growth, and eventual coalescence of voids. In structural metals deformed at room temperature, voids usually form through secondary-phase particle decohesion or particle fracture. These voids then grow due to plastic deformation of the surrounding matrix. Void coalescence can occur through matrix material narrowing between adjacent voids or localized shearing between widely spaced voids (see introductory section in Benzerga et al. (2016)). Over the last half-century, the experimental investigation on ductile fracture has extensively relied on postmortem observations and interrupted-tests examinations of specimens with varying shapes, which were tested under different loading conditions. For example, one of the primary objectives of the experimental campaigns of Hancock and Mackenzie (1976), Johnson and Cook (1985), Bao and Wierzbicki (2004), Barsoum and Faleskog (2007) and Beese et al. (2010) was to identify the effects of triaxiality and Lode parameter on failure mechanisms. The prevailing idea is that the failure strain follows a monotonically decreasing trend with increasing stress triaxiality, whereas it demonstrates a minimum for Lode parameter corresponding to generalized shear (Ghahremaninezhad and Ravi-Chandar, 2013; Scales et al., 2016; Morin et al., 2018). Recently, techniques such as metallography, fractography and in-situ microscopy have been utilized to identify the initiation and progression of damage mechanisms throughout the process of deformation, plastic localization and eventual failure, and allowed estimation of local fracture strain levels based on change in grain size (Ghahremaninezhad and Ravi-Chandar, 2012; Haltom et al., 2013; Gross and Ravi-Chandar, 2016). The measurements performed at the length scale of the grains were notably higher than the strain-to-failure obtained from macroscale strain readings based on characteristic specimen dimensions, underscoring the importance highlighted by Ghahremaninezhad and Ravi-Chandar (2011, 2013) to assess the fracture strain at the microstructural level. In recent years, progress in X-ray micro-tomography techniques, alongside related synchrotron imaging methods, has facilitated time-resolved in-situ volumetric observations of damage development at the sub-micrometer scale, leading to a comprehensive understanding of fracture micro-mechanisms evolution during loading (Morgeneyer and Besson, 2011; Morgeneyer et al., 2016; Roth et al., 2018; Kong et al., 2022). For instance, Ueda et al. (2014) monitored the evolution of individual voids during the ductile tearing of aluminum 2139-T3 flat-notched specimens subjected to mode I fracture. They quantified the evolution of void volume and rotation at positions with distinct stress and strain histories on both flat and slant cracks. As another example, Tancogne-Dejean et al. (2021) observed and statistically tracked intermetallic particles and pre-existing voids in an aluminium 2024-T3 *smiley* shear specimen tested at low triaxiality. The study revealed that intermetallic particles fractured with cracks oriented perpendicular to the major principal stress direction, while pre-existing voids exhibited rotational motion and closure.

Expanding upon the foundational micromechanical studies of void growth developed by McClintock (1968) and Rice and Tracey (1969), a significant body of research has evolved over the last five decades, with the goal of modeling ductile fracture in metals and alloys. Notably, Gurson (1977) formulated what is arguably the most popular and widely utilized micromechanical yield criterion for porous solids containing spherical or cylindrical voids. The Gurson (1977) model was developed by conducting a limit-analysis on a finite-radius hollow sphere or cylinder surrounded by matrix material characterized using the von Mises (1928) criterion, subjected to a uniform boundary strain rate under quasi-static loading conditions. The limitations of the Gurson (1977) model in considering spherical or cylindrical voids and elastic perfectly-plastic isotropic materials have spurred numerous extensions of this yield criterion over recent decades, encompassing void nucleation (Chu and Needleman, 1980), void coalescence (Tvergaard and Needleman, 1984), effects of void shape and size (Thomason, 1985; Gologanu et al., 1997; Jackiewicz, 2011; Wen et al., 2005; Monchiet and Bonnet, 2013), and distinct features of the matrix material's constitutive model, such as strain hardening (Leblond et al., 1995), strain rate hardening (Duva, 1986; Gărăjeu et al., 2000), and plastic anisotropy (Benzerga and Besson, 2001; Stewart and Cazacu, 2011). Additionally, some efforts have aimed to integrate the Lode angle into the Gurson model, exploring the role of the third stress invariant in ductile fracture (Nahshon and Hutchinson, 2008; Benallal et al., 2014; Vadillo et al., 2016). However, none of these Gurson-type yield criteria consider the influence of inertia on the mechanical behavior of porous aggregates under dynamic deformations.

A robust and physically grounded constitutive framework for describing the macromechanical response of porous metals subjected to high strain rate impacts was pioneered by Molinari and Mercier (2001). Specifically, by building upon previous studies conducted by Carroll and Holt (1972), Klöcker and Montheillet (1991) and Wang (1994a,b, 1997), among others, Molinari and Mercier (2001) developed a micromechanical yield criterion for porous aggregates utilizing a dynamic homogenization approach which considers the influence of local acceleration fields that emerge around voids during high loading rate conditions (Ortiz and Molinari, 1992; Wright and Ramesh, 2008). This criterion assumes the total stress to be additively decomposed into static and dynamic components (Wang and Jiang, 1997). The static contribution is computed using any Gurson-type flow potential (outlined in the preceding paragraph), whereas the dynamic component is obtained from the solution governing the dynamic expansion of spherical voids within a finite medium (e.g., see Glennie (1972) and Tong and Ravichandran (1993, 1995)). The dynamic stress, often denoted as microinertia, highlights that the the initial void size serves as an inherent length scale governing the overall dynamic behavior of the material (Czarnota et al., 2006, 2008; Jacques et al., 2015). This essential feature is unaccounted for in the quasi-static formulations of the Gurson-type damage models, where porosity serves solely as the damage parameter, without taking into account the influence of void size. Czarnota et al. (2006) extended the formulation presented in Molinari and Mercier (2001) by introducing a tailored void nucleation model which presupposes a material initially devoid of pores, wherein voids arise from pre-existing sites once a critical cavitation pressure threshold is exceeded. To characterize the distribution of critical cavitation pressure among potential nucleation sites, a Weibull probability distribution was applied, while the influence of void interaction during damage evolution was modeled through the introduction of an effective interplay distance between voids. The theoretical predictions of Czarnota et al. (2006) accurately reproduced the phenomenon of direct impingement between adjacent voids observed in postmortem analyses of spall fractures resulting from plate-impact experiments on high-purity grade tantalum conducted by Roy (2003). Subsequently, Czarnota et al. (2008) expanded the void nucleation and growth model initially proposed by Czarnota et al. (2006) to consider an elastic–viscoplastic material response and integrated it into ABAQUS/Explicit to perform numerical simulations of the plate-impact tests carried out by Roy (2003). The model's predictions were validated against experimental free-surface velocity profiles, revealing a notable increase in maximum stress within the spall plane as the impact velocity increased, consistent with the experimental evidence reported in the literature (Romanchenko and Stepanov, 1980; Kanel et al., 1984; Kanel, 2010). Shortly after, Jacques et al. (2010) enriched the model of Czarnota et al. (2008) through the incorporation of a nonlinear elastic response formulation based on the Mie-Grüneisen equation of state, alongside a void nucleation law where the density of cavitation sites per unit initial volume is influenced by the applied pressure, the critical cavitation pressure, and a set of material microstructure-related parameters. The model developed by Jacques et al. (2010) was implemented into the ABAQUS/Explicit utilizing an integration algorithm closely resembling the approach developed by Czarnota et al. (2008). The resulting numerical simulations showed a robust correlation with a variety of post-mortem experimental measurements of spall fractures derived from the tests conducted by Roy (2003), encompassing mean void radius at varying impact velocities and spatial distribution of porosity near the spall plane. The numerical results were clearly affected by the stabilizing influence of microinertia, causing a reduction in the average void size at higher impact velocities due to its constraining effect on void growth.

The impact of microinertia on the ductile failure of materials under high strain rates has been investigated in recent papers using the dynamic homogenization approach of Molinari and Mercier (2001) to address problems other than spall fracture in plate-impact experiments. For instance, the effect of microinertia on the propagation of shock waves in porous ductile metals was examined in the studies of Czarnota et al. (2017, 2020). At low shock pressures, the shock structure was shown to be primarily governed by material strain rate sensitivity and initial void volume fraction. Nevertheless, the increase in shock amplitude was demonstrated to enhance the influence of microinertia, resulting in the initial void size shaping the shock front. Furthermore, the heightened acceleration fields around void boundaries have been shown to contribute to shock mitigation, reducing strain rate levels and slowing down the collapse rate of voids. As another example, Jacques et al. (2012a) investigated the role of microinertia in dynamic ductile crack growth in porous ductile materials. Finite element calculations on notched bars and edge-cracked specimens subjected to dynamic tension revealed that microinertia effects slows down void growth, leading to a delay in the strain localization process that precedes fracture, reducing crack speed, and increasing fracture toughness. Furthermore, the reduction in void growth rate naturally enlarges the size of the plastic localization zone near the crack, serving as an inherent regularization mechanism that mitigates pathological mesh sensitivity. Microstructural inertia effects were also found to influence void coalescence in porous materials (Jacques et al., 2012c; Molinari et al., 2015).

The papers discussed in the preceding two paragraphs highlight that the constitutive framework proposed by Molinari and Mercier (2001) predicts a notable influence of microinertia effects on the localization and fracture processes of ductile porous materials subjected to high strain rates and high stress triaxialities. However, the microinertia-based approach has not yet been validated against simulations replicating the underlying porous microstructure, particularly concerning the temporal evolution of specific micro-mechanical features such as void volume fraction and the development of plastic localization. This is precisely the objective of this paper in which finite element calculations performed with the dynamic homogenization model developed by Molinari and Mercier (2001) and implemented in ABAQUS/Explicit by Jacques et al. (2012a) are compared with simulations in which spherical pores are explicitly included in the finite element model. The problem addressed is a flat double-notched specimen subjected to dynamic plane strain tension. The calculations are performed with the initial void volume fraction in the notched section varying from 0.5% to 4%, and spherical pore diameters ranging from 30 μm to 150 μm. The applied tensile velocities span from 100 m/s to 1000 m/s, yielding maximum strain rates between 10^5 s^{-1} and 10^6 s^{-1}, and stress triaxiality values from 4 to 30. The initial void volume fractions and void sizes investigated are based on experimental measurements of additive manufactured metals (Marvi-Mashhadi et al., 2021; Nieto-Fuentes et al., 2023), while the range of strain rates are observed in dynamic fragmentation and plate-impact experiments (Kanel, 2010; Czarnota et al., 2017). The manuscript is organized as follows: Section 2 describes the fundamental aspects of the constitutive framework for porous materials subjected to dynamic loading formulated by Molinari and Mercier (2001), Section 3 details the finite element models created to investigate the effect of microstructural inertia on plastic localization and void growth, Section 4 presents the simulation results for various loading velocities, void sizes, and void volume fractions, and the main conclusions of this research are summarized in Section 5.

2. Constitutive framework

This section outlines the primary features of the constitutive framework for porous materials under high strain rate loading developed by Molinari and Mercier (2001), while a comprehensive description of the formulation can be found in the works of Czarnota et al. (2008) and Jacques et al. (2012a, 2015). Note that neither pore nucleation nor material fracture is taken into account in the present work. Additionally, all voids are initially uniform in size and shape (spherical). While these assumptions may seem restrictive, as they are not representative of most materials and applications, they align effectively with the purpose of this paper: investigating the influence of microinertia on void growth and plastic localization. Note that assuming all voids initially have the same size and shape is consistent with the simulations involving discrete pores presented in Section 4. The representative volume element of the porous material is modeled as a unit cell consisting of a hollow sphere with a central spherical void. Note that incorporating inertia effects into the modeling of a hollow sphere response causes the effective void size to influence the mechanical behavior of the unit cell. Therefore, the use of a single hollow sphere as the representative volume element under dynamic loading conditions is appropriate only when all voids are identical in size, as assumed in this work. The extension of the constitutive model to account for voids with varying initial sizes, using a two-step homogenization approach, can be found in Czarnota et al. (2008) and Jacques et al. (2012a, 2015).

The homogenized stress tensor at the level of the unit cell $\boldsymbol{\Sigma}$ is defined as:

$$\boldsymbol{\Sigma} = \boldsymbol{\Sigma}^{\mathrm{sta}} + \boldsymbol{\Sigma}^{\mathrm{dyn}} \tag{1}$$

where the static Cauchy stress tensor $\boldsymbol{\Sigma}^{\mathrm{sta}}$ is derived from the constitutive behavior of the matrix material, representing the response of the porous aggregate in the absence of microinertia effects, and $\boldsymbol{\Sigma}^{\mathrm{dyn}}$ is the dynamic Cauchy stress tensor arising from the local acceleration of the material within the hollow sphere.

The static stress is derived from an associated plastic flow rule:

$$\mathbf{D}^{\mathrm{p}} = \dot{\lambda} \frac{\partial \Phi}{\partial \boldsymbol{\Sigma}^{\mathrm{sta}}} \tag{2}$$

with $\mathbf{D}^{\mathrm{p}}$ being the plastic strain rate tensor, $\dot{\lambda}$ the rate of plastic multiplier and Φ the Gurson-Tvergaard flow potential (Gurson, 1977; Tvergaard, 1982):

$$\Phi = \left(\frac{\Sigma_{\mathrm{eq}}^{\mathrm{sta}}}{\sigma_Y} \right)^2 + 2\mathrm{q}_1 f \cosh\left(\frac{3\mathrm{q}_2 \Sigma_{\mathrm{m}}^{\mathrm{sta}}}{2\sigma_Y} \right) - 1 - (\mathrm{q}_1 f)^2 \tag{3}$$

where $\Sigma_{\mathrm{eq}}^{\mathrm{sta}} = \sqrt{\frac{3}{2}\, \mathbf{S}^{\mathrm{sta}} : \mathbf{S}^{\mathrm{sta}}}$ is the effective stress, with $\mathbf{S}^{\mathrm{sta}} = \boldsymbol{\Sigma}^{\mathrm{sta}} - \Sigma_{\mathrm{m}}^{\mathrm{sta}} \mathbf{1}$ being the deviatoric part of the static Cauchy stress tensor, and $\Sigma_{\mathrm{m}}^{\mathrm{sta}} = \dfrac{1}{3} \boldsymbol{\Sigma}^{\mathrm{sta}} : \mathbf{1}$ is the hydrostatic stress, with $\mathbf{1}$ being the second-order identity tensor. Moreover, q_1 and q_2 are material parameters, $f = \dfrac{a^3}{b^3}$ is the porosity in the unit cell, with a and b being the inner and outer radii of the hollow sphere, respectively, and σ_Y is the flow strength of the matrix material, defined by the following relationship:

$$\sigma_Y = \sigma_Y^0 + \sigma_K (\bar{\varepsilon}^p)^n \left(\frac{\dot{\bar{\varepsilon}}^p}{\dot{\varepsilon}_{ref}} \right)^m \left(\frac{T}{T_{ref}} \right)^\mu \tag{4}$$

where σ_Y^0 represents the initial flow strength, σ_K is the plastic modulus, n is the strain hardening exponent, m and μ are the strain rate and temperature sensitivity parameters, and $\dot{\varepsilon}_{ref}$ and T_{ref} are the reference strain rate and temperature, respectively. The effective plastic strain of the matrix material is $\bar{\varepsilon}^p = \int_0^t \dot{\bar{\varepsilon}}^p d\tau$ where $\dot{\bar{\varepsilon}}^p$ is the effective plastic strain rate. Moreover, T is the current temperature.

The dynamic stress is expressed as:

$$\boldsymbol{\Sigma}^{\mathrm{dyn}} = \mathrm{P}^{\mathrm{dyn}} \mathbf{1} \tag{5}$$

where the dynamic pressure $\mathrm{P}^{\mathrm{dyn}}$ is derived assuming that the voids remain spherical during loading (i.e., the constitutive model is valid for high triaxialities):

$$\mathrm{P}^{\mathrm{dyn}} = \rho a^2 \left[\dot{\mathrm{D}}^{\mathrm{p}}_{\mathrm{m}} \left(f^{-1} - f^{-2/3} \right) + (\mathrm{D}^{\mathrm{p}}_{\mathrm{m}})^2 \left(3f^{-1} - \frac{5}{2} f^{-2/3} - \frac{1}{2} f^{-2} \right) \right] \tag{6}$$

where $\mathrm{D}^{\mathrm{p}}_{\mathrm{m}} = \dfrac{1}{3}\, \mathbf{D}^{\mathrm{p}} : \mathbf{1}$ and ρ is the density of the matrix material (this expression relies on the assumption that the matrix material is incompressible, see Molinari and Mercier (2001)). Note that the dynamic stress depends on both the strain rate $\mathrm{D}^{\mathrm{p}}_{\mathrm{m}}$ and its time derivative $\dot{\mathrm{D}}^{\mathrm{p}}_{\mathrm{m}}$.

The formulation is completed with the Kuhn–Tucker loading–unloading conditions:

$$\dot{\lambda} \geq 0, \qquad \Phi \leq 0, \qquad \dot{\lambda}\Phi = 0 \tag{7}$$

2.1. Elastic behaviour

The strain rate tensor $\mathbf{D}$ is assumed to be the sum of an elastic part $\mathbf{D}^{\mathrm{e}}$ and a plastic part $\mathbf{D}^{\mathrm{p}}$:

$$\mathbf{D} = \mathbf{D}^{\mathrm{e}} + \mathbf{D}^{\mathrm{p}} \tag{8}$$

where the plastic part was defined in equation (2), and the elastic part is related to the rate of the stress by the following linear hypo-elastic law:

$$\overset{\triangledown}{\mathbf{\Sigma}} = \mathbf{L} : \mathbf{D}^{\mathrm{e}} \tag{9}$$

where $\overset{\triangledown}{\mathbf{\Sigma}}$ is an objective derivative of the Cauchy stress tensor, and $\mathbf{L}$ is the tensor of isotropic elastic moduli given by:

$$\mathbf{L} = \frac{E}{1+\nu}\mathbf{I}' + \frac{E}{3(1-2\nu)}\mathbf{1} \otimes \mathbf{1} \tag{10}$$

with E being the Young's modulus, ν the Poisson's ratio, $\mathbf{1}$ the unit second-order tensor (as mentioned before) and $\mathbf{I}'$ the unit deviatoric fourth-order tensor.

2.2. Evolution of the internal state variables

Assuming that the change in volume of the representative volume element is attributed solely to void growth (void nucleation is neglected), the evolution of porosity is as follows:

$$\dot{f} = 3\,(1-f)\,\mathrm{D}^{\mathrm{p}}_{\mathrm{m}} \tag{11}$$

with the evolution of the radius of the voids being:

$$\dot{a} = a\frac{\mathrm{D}^{\mathrm{p}}_{\mathrm{m}}}{f} \tag{12}$$

Moreover, the effective plastic strain rate in the matrix material is obtained assuming that the rate of plastic work in the representative volume element is equal to the rate of effective plastic work in the matrix material:

$$\dot{\bar{\varepsilon}}^{p} = \frac{\mathbf{\Sigma}^{\mathrm{sta}} : \mathbf{D}^{\mathrm{p}}}{(1-f)\,\sigma_Y} \tag{13}$$

Assuming adiabatic conditions of deformation (no heat flux) and considering that plastic work is the only source of heat, the evolution of the temperature is given by:

$$\dot{T} = \beta\frac{\sigma_Y\dot{\bar{\varepsilon}}^{p}}{\rho C_p} \tag{14}$$

where ρ is the density of the matrix material, C_p is the heat capacity of the matrix material and β is the Taylor-Quinney coefficient.

2.3. Material parameters

The material parameters utilized in the finite element simulations presented in Section 4 are outlined in Table 1. The numerical values of mass density, specific heat, elastic constants and parameters of the flow strength of the matrix material correspond to AISI 430 steel (Vaz-Romero et al., 2015). The parameters β, q_1, and q_2 are assigned standard values commonly found in the literature. The constitutive framework has been implemented in ABAQUS/Explicit (2019) through a user subroutine VUMAT using the integration algorithm developed by Jacques et al. (2012a).

3. Finite element model

The problem addressed is that of a flat double-notched specimen subjected to dynamic plane strain tension, see Fig. 1. The sample has initial length of $L^0 = 20$ mm and initial width of $W^0 = 18$ mm. Different values of the initial thickness within the range 0.566 mm $\leq H^0 \leq$ 5.656 mm are considered depending on the initial void volume fraction and void size, with the aim of including eight layers of voids throughout the specimen's thickness (refer to subsequent paragraphs for detailed information regarding the dimensions of the voids and the corresponding void volume fractions analyzed). The U-shaped notch, centrally located along the specimen's length, has a depth of $S^0 = 4$ mm and a width of $F^0 = 4$ mm. This specimen design is chosen due to the development of elevated stress triaxiality within the notched region (see Section 4), which fosters the growth of voids. Moreover, in order to decrease the computational time of the calculations, we have modeled only one-eight of the sample and implemented symmetry boundary conditions. Material

Symbol	Property and units	Value
ρ	Mass density (kg/m^3), Eq. (14)	7740
C_p	Specific heat (J/kg K), Eq. (14)	460
E	Young's modulus (GPa), Eq. (10)	200
ν	Poisson's ratio, Eq. (10)	0.3
σ_Y^0	Initial yield strenght (MPa), Eq. (4)	175.67
σ_K	Strain hardening modulus (MPa), Eq. (4)	530.13
n	Strain hardening exponent, Eq. (4)	0.167
$\dot{\varepsilon}_{ref}$	Reference strain rate (s^{-1}), Eq. (4)	0.01
m	Strain rate sensitivity exponent, Eq. (4)	0.0118
T_{ref}	Reference temperature (K), Eq. (4)	300
μ	Temperature sensitivity exponent, Eq. (4)	-0.51
q_1	Material parameter, Eq. (3)	1.25
q_2	Material parameter, Eq. (3)	1
β	Taylor-Quinney coefficient, Eq. (14)	0.9

Table 1: Material parameters utilized in the finite element simulations reported in Section 4. The numerical values of initial density, elastic constants and parameters of the flow strength of the matrix material correspond to AISI 430 steel (Vaz-Romero et al., 2015). The parameters β, q_1 and q_2 take standard values used in the literature.

points are referred to using a Lagrangian Cartesian coordinate system (X, Y, Z) with origin located at the bottom left corner of the finite element model (i.e., at the center of mass of the specimen if no symmetry boundary conditions are applied). The sample is under plane strain constraint in the Z-direction (therefore, we could have included a single layer of voids throughout the thickness of the sample; however, the aim was to observe the direct interaction between voids). The finite element calculations are performed with ABAQUS/Explicit (2019) under the following imposed initial conditions:

$$\begin{aligned} V_Y(X,Y,Z,0) &= \dot{\varepsilon}^0_{YY} Y, \quad \text{for} \quad 0 \leq Y \leq \frac{F^0}{2} \\ V_Y(X,Y,Z,0) &= \dot{\varepsilon}^0_{YY}\frac{F^0}{2} = V, \quad \text{for} \quad \frac{F^0}{2} \leq Y \leq \frac{L^0}{2} \\ T(X,Y,Z,0) &= T^0 = T_{ref} \end{aligned} \tag{15}$$

and boundary conditions:

$$\begin{aligned} U_X(0,Y,Z,t) &= 0 \\ U_Y(X,0,Z,t) &= 0 \\ U_Z(X,Y,0,t) &= U_Z\left(X, Y, -\frac{H^0}{2}, t\right) = 0 \\ V_Y\left(X, \frac{L^0}{2}, Z, t\right) &= \dot{\varepsilon}^0_{YY}\frac{F^0}{2} = V \end{aligned} \tag{16}$$

with $\dot{\varepsilon}^0_{YY}$ being the imposed initial strain rate and V the corresponding imposed loading velocity, see Fig. 1. In the calculations presented in Section 4, the applied velocities are changed across a range from 100 m/s to 1000 m/s, which correspond to average strain rates in the gauge section spanning between 10^5 s^{-1} and 10^6 s^{-1}, leading to values of the stress triaxiality in the notched section ranging from 4 to 30 (see Section 4). The calculations are performed for the initial void volume fraction varying in the notched section from 0.5% to 4%, with pores of diameter ranging from 30 μm to 150 μm (the specimen features porosity within the notched region while being fully dense outside this area). The initial void volume fractions and void sizes considered are representative of 3D printed metals (Marvi-Mashhadi et al., 2021; Nieto-Fuentes et al., 2023), while the selection of strain rates corresponds to dynamic fragmentation and plate-impact experiments (Kanel, 2010; Czarnota et al., 2017). Moreover, the applied initial conditions serve to mitigate the propagation of stress waves within the specimen resulting from the sudden motion of the strip at $t = 0$. Without these conditions, the waves generated by the velocity boundary condition could trigger immediate plastic localization at the specimen surface where the loading velocity is applied (Needleman, 1991; Xue et al., 2008).

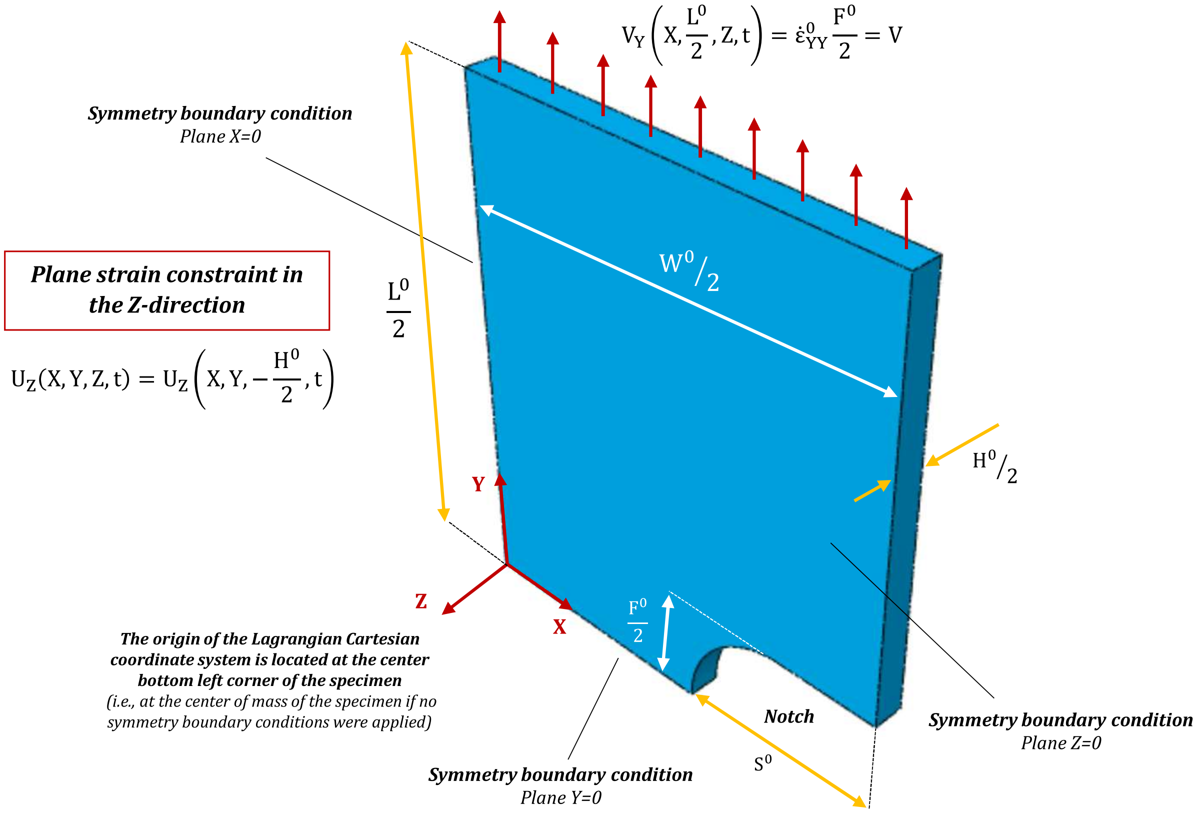

Figure 1: Schematic of the geometry and boundary conditions of the problem addressed: a double-notched specimen subjected to dynamic plane strain tension. The sample has initial length of $L^0 = 20$ mm, initial width of $W^0 = 18$ mm, and initial thickness of $H^0 = 1.188$ mm. The U-shaped notch, centrally located along the specimen's length, has a depth of $S^0 = 4$ mm and a width of $F^0 = 4$ mm. The model consists of one-eight of the sample with symmetry boundary conditions. Material points are referred to using a Lagrangian Cartesian coordinate system (X, Y, Z) with origin located at the bottom left corner of the finite element model (i.e., at the center of mass of the specimen if no symmetry boundary conditions were applied). The velocity loading condition is $V_Y\left(X, \frac{L^0}{2}, Z, t\right) = \dot{\varepsilon}^0_{YY}\frac{F^0}{2}$. The sample is under plane strain constraint in the Z-direction.

Note that Jacques et al. (2012a, 2015) employed an asymmetric finite element model of a notched specimen with circular cross-section and subjected to dynamic tension to study plastic localization and fracture of porous materials. However, in this paper, we have opted for a 3D specimen with a rectangular cross-section subjected to plane strain tension. This allows for an explicit description of the material's porous microstructure to be incorporated into the finite element model.

3.1. Actual porosity

The finite element model includes discrete voids in the notched area –see Fig. 2– following the methodology put forth by Marvi-Mashhadi et al. (2021) and later adopted by Nieto-Fuentes et al. (2022) and Vishnu et al. (2022a,b) to study the role of actual porous microstructures on the formation of necks and shear bands under dynamic loading (our previous research involving dynamic simulations that incorporate actual pores did not investigate the influence of microinertia on void growth and plastic localization). Recall that the specimen only features porosity within the notched region while being fully dense outside this area. The mechanical behavior of the material is modeled using von Mises plasticity, associated flow rule and isotropic hardening defined by equation (4), i.e., we consider the material to be described by the constitutive framework given in Section 2 imposing that $f = 0$. The incorporation of actual voids within the finite element model ensures that the effect of microinertia is inherently considered in the simulations. The pores are assumed to be initially spherical, consistent with findings from X-ray tomography measurements of additive manufactured metals conducted by Nieto-Fuentes et al. (2023), and all are considered to have the same size. Note that for this range of pore diameters, 30 μm $\leq \phi \leq$ 150 μm, microinertia is expected to play a significant role in void dynamics (Wilkerson and Ramesh, 2014; Wilkerson, 2017). The number of voids in the model is contingent on the pores' diameter and the void volume fraction, which also determine the specimen thickness. The simulations represent a periodic microstructure comprising an array of unit cells with the same initial void volume fraction. The number of voids included in these calculations, along with the voids dimensions and the corresponding initial void volume fraction and specimen thickness, are presented in Table 2. We have imposed four layers of voids across half of the sample thickness.

Initial void volume fraction, f^0 (%)	0.5			2			4		
Voids diameter, ϕ (μm)	30	50	150	30	50	150	30	50	150
Number of voids, N^{total} (num.)	2332	832	88	5620	2056	248	8928	3116	364
Initial specimen thickness, H^0 (mm)	1.132	1.886	5.656	0.712	1.188	3.564	0.566	0.942	2.828

Table 2: Porous microstructures investigated in the finite element calculations with discrete voids. Initial void volume fraction, $\left(f^0\right)$, voids diameter (ϕ), number of voids $\left(N^{total}\right)$ and initial specimen thickness $\left(H^0\right)$.

The specimen has been discretized using ten-node quadratic tetrahedral elements, referred to as C3D10 in ABAQUS notation. The total number of elements varies between 1415765 and 5782312, depending on the number and the size of voids included in the model. The smallest elements near the voids have a characteristic length of approximately 3 μm (for the simulations containing voids of 30 μm diameter). We conducted a mesh sensitivity analysis by increasing the number of elements and confirmed that the numerical results in Section 4 are hardly affected by the discretization. Note that

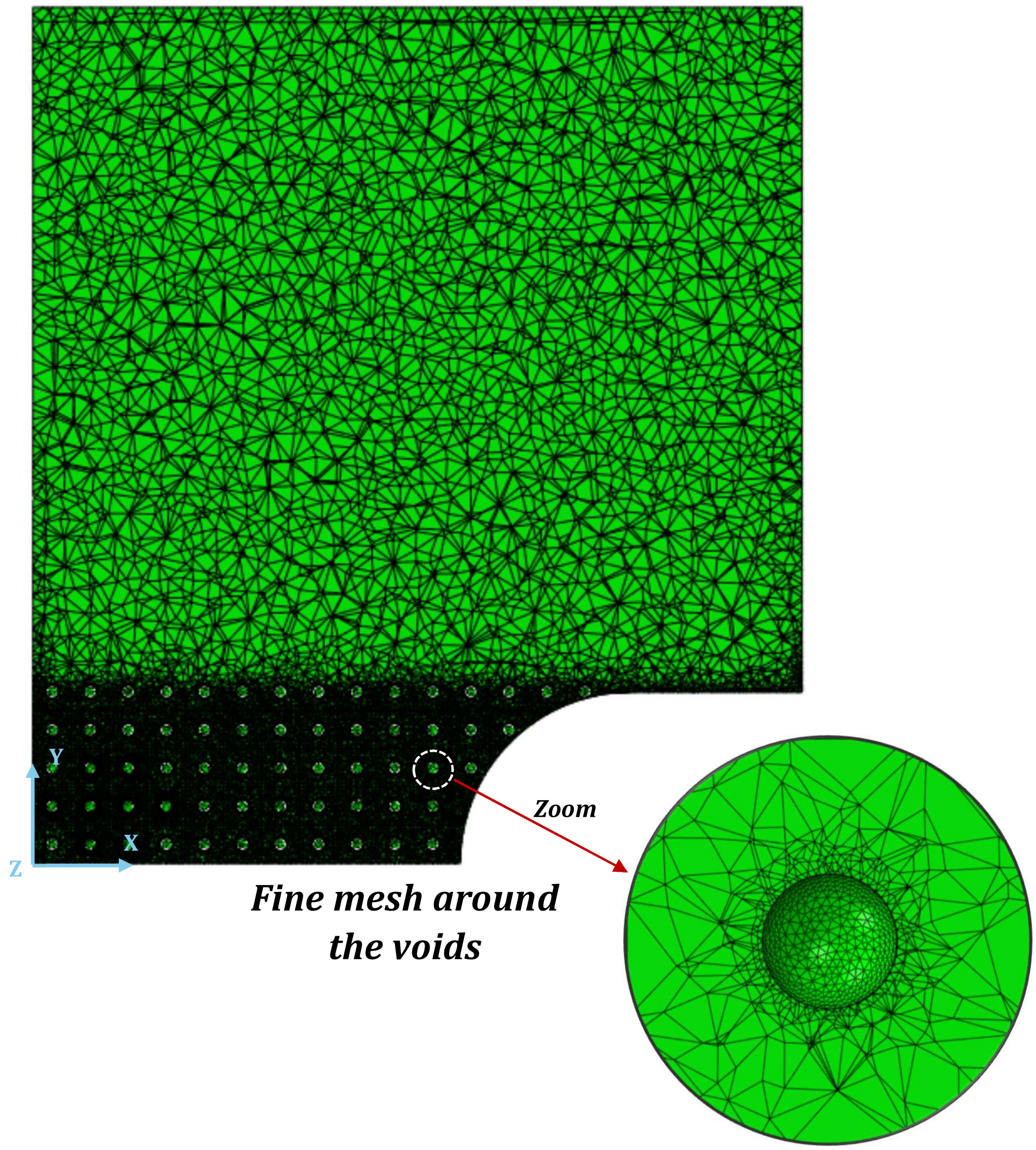

Figure 2: Finite element model developed in ABAQUS/Explicit (2019) to investigate the effect of microinertia on plastic localization and dynamic void growth in a double-notched specimen subjected to plane strain tension. The model consists of one-eighth of the sample with symmetry boundary conditions, see Fig. 1. The specimen features actual pores within the notched region while being fully dense outside this area. The sample has initial thickness of $H^0 = 3.564$ mm, with initial void volume fraction in the notched region of $f^0 = 2\%$ and initial voids size of $\phi = 150$ μm. All the pores have the same size. Four layers of voids are included across half of the sample thickness. Cross-section view at $Z = -0.223$ mm. The mechanical behavior of the material is modeled utilizing the constitutive framework given in Section 2 imposing that $f = 0$ (i.e., the mechanical behavior of the material is described using von Mises plasticity, associated flow rule and isotropic hardening defined by equation (4)). The model is meshed using ten-node tetrahedron elements with hourglass control (C3D10 in ABAQUS/Explicit (2019) notation). The characteristic length of the smallest elements within the notched section is ≈ 3 μm. Note the close-up view of the mesh in the notched region illustrating the size of the elements near the void.

inertia, strain rate sensitivity and the explicit description of the porous microstructure serve as effective regularization factors that mitigate the impact of discretization in the numerical simulations. The computations were performed on a workstation with an AMD Epyc 7413 processor running at 2.75 GHz with 48 cores. The computational time for each simulation presented in this paper ranged from 5 to 30 days, depending on the specific porous microstructure and applied velocity boundary conditions.

The calculation of void volume fraction evolution within the notch during loading follows the two-step methodology introduced by Vishnu et al. (2022b, 2023):

- The volume of the matrix material at each time step (MMV) is derived by summing the volumes of the individual elemental components ($EVOL$):

$$MMV = \sum_{n=1}^{n_{elem}} EVOL_n \tag{17}$$

  where n_{elem} is the total number of elements in the model.

- The coordinates of the nodal points on the outer surfaces of the notch are exported to MATLAB® at each time step. Subsequently, the *convhull* function is utilized to determine the total volume of the notch (TVN).

Afterwards, the void volume fraction at each time step (f) is calculated as follows:

$$f = \frac{TVN - MMV}{TVN} \tag{18}$$

Furthermore, we have examined the evolution of individual void volumes using the Quickhull algorithm (Barber et al., 1996) available within MATLAB®, which calculates the smallest convex set that encompasses the nodal coordinates of the void surface at each time step.

3.2. Homogenized porosity

The finite element model does not contain explicitly resolved voids, see Fig. 3. The mechanical behavior of the material is modeled with the dynamic homogenization approach presented in Section 2. The specimen features porosity within the notched region while being fully dense outside this area. We performed computations with voids of uniform size that can be directly compared with the simulations of actual porosity. Recall that despite the voids are not explicitly represented, the diameter of the pores is an input parameter to be defined in the dynamic homogenization model. The void dimensions, initial void volume fraction, and specimen thickness are the same as those used in the calculations with discrete pores.

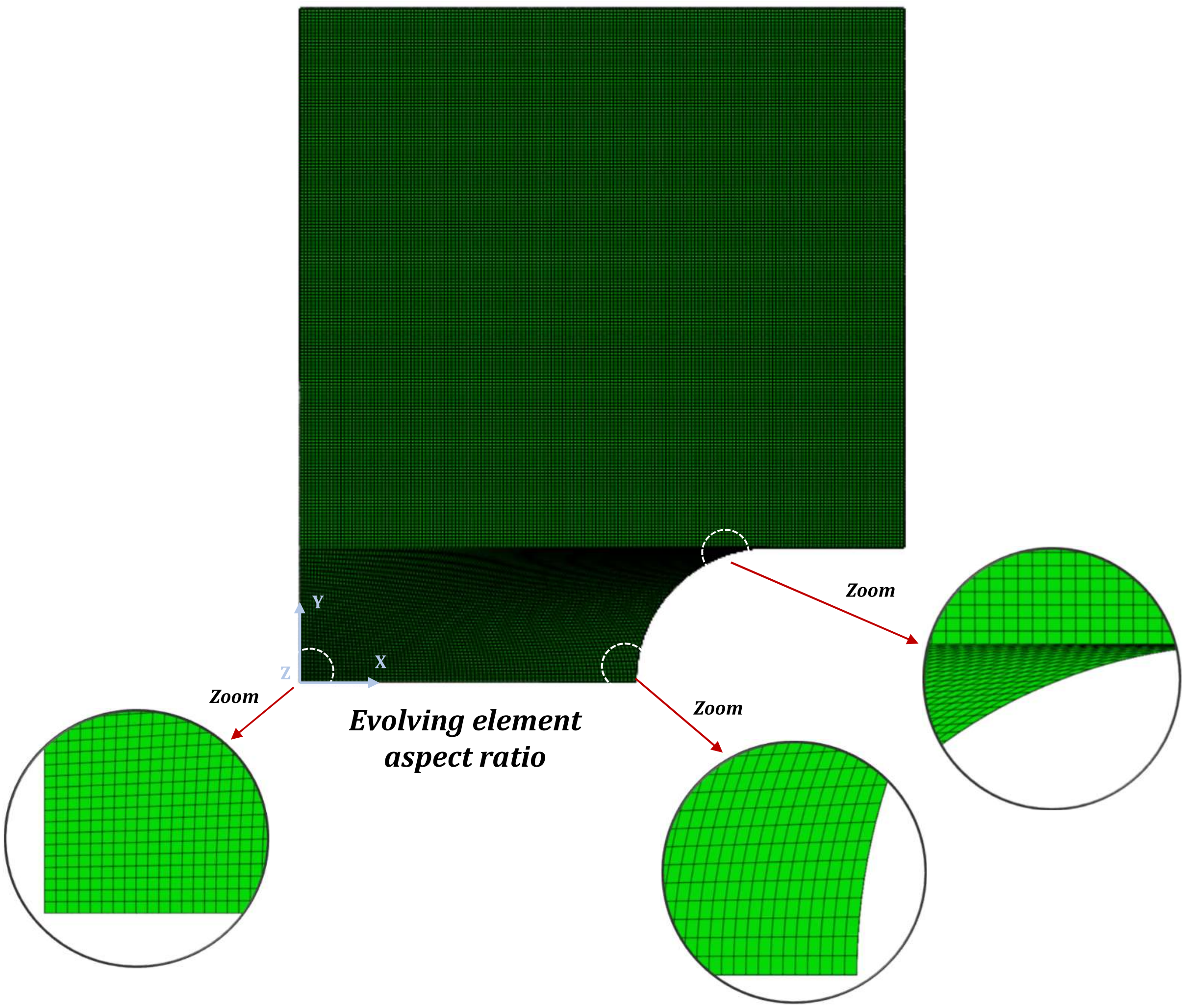

Figure 3: Finite element model developed in ABAQUS/Explicit (2019) to investigate the effect of microinertia on plastic localization and dynamic void growth in a double-notched specimen subjected to plane strain tension. The model consists of one-eighth of the sample with symmetry boundary conditions. The sample has initial thickness of $H^0 = 3.564$ mm, with initial void volume fraction in the notched region of $f^0 = 2\%$ and initial voids size of $\phi = 150$ μm. Cross-section view at $Z = -0.223$ mm. The mechanical behavior of the material is modeled with the dynamic homogenization approach presented in Section 2. The specimen features porosity within the notched region while being fully dense outside this area. The model is meshed using eight-node linear brick elements with reduced integration and hourglass control (C3D8R in ABAQUS/Explicit (2019) notation). The characteristic length of the smallest elements within the notched section is ≈ 60 μm. Note the close-up views of the mesh in various sections of the notched region illustrating the evolving aspect ratio of the elements.

The specimen has been discretized using eight-node linear brick elements with reduced integration and hourglass control, referred to as C3D8R in ABAQUS notation. The total number of elements ranges from 229019 to 1864869, depending on the initial void volume fraction and the size of the voids included in the model (i.e., depending on the initial thickness of the sample). The smallest elements within the notched region have a characteristic length of approximately 60 μm. The shape and size of the elements varies in different zones of the notched section, see Fig. 3. We have performed a mesh sensitivity analysis increasing the number of elements, and checked that the numerical results presented in Section 4 including microinertia are hardly dependent on the discretization for most of the loading velocities investigated (for the lowest loading velocity of 100 m/s, the effect of microinertia is small, leading to the formation of a localization band confined within a single layer of elements, see Section 4.2). Microstructural inertia serves as an effective regularization factor, mitigating the effects of discretization in numerical simulations (Czarnota et al., 2008; Jacques et al., 2012a; Versino and Bronkhorst, 2018). In contrast, the calculations performed with the standard Gurson-Tvergaard model without microinertia show pathological mesh dependency, see Section 4. The computations were performed using a laptop computer with processor Intel(R) Core(TM) i9 − 9900U CPU running at 3.10 GHz with 8 cores. The computational time for each simulation ranged from 10 minutes to 9 hours, depending on the specific porous microstructure considered and the applied velocity boundary conditions. Note that these calculations are significantly faster than the simulations with the explicitly resolved pores.

4. Results

The presentation of results is divided into four parts. Section 4.1 describes the methodology developed to compare void growth and plastic localization from calculations involving: (i) actual pores and material modeled using von Mises plasticity, (ii) homogenized porosity and material modeled using Gurson-Tvergaard plasticity including microinertia effects, and (iii) homogenized porosity and material modeled using Gurson-Tvergaard plasticity without microinertia effects (removing the contribution of dynamic stresses from the formulation described in Section 2 to recover the quasi-static Gurson-Tvergaard model). Moreover, Sections 4.2, 4.3 and 4.4 include simulations for various loading rates, void sizes and void volume fractions to investigate the influence of microinertia on the collective behavior of voids under high strain rates.

4.1. Salient features

Figure 4 shows contours of effective plastic strain $\bar{\varepsilon}^p$ for different imposed displacement values: (a)-(a')-(a") $U_Y = 0.05$ mm, (b)-(b')-(b") $U_Y = 0.125$ mm, (c)-(c')-(c") $U_Y = 0.25$ mm, (d)-(d')-(d") $U_Y = 0.375$ mm, and (e)-(e')-(e") $U_Y = 0.5$ mm. The plots correspond to a cross-sectional view at $Z = -0.074$ mm, see the Lagrangian coordinate system in Fig. 1. The color coding of the isocontours maps effective plastic strains from 0 to 2 on a blue-to-red scale, with strains above 2 remaining red (note that the same color scale has been consistently applied across all contour plots presented in this paper, see Figs. 11, 14, 17, 24, 27, 34 and 36). The imposed loading velocity is $V = 500$ m/s, the initial void volume fraction in the notched region is $f^0 = 2\%$ and the initial diameter of the voids is $\phi = 50$ μm. This combination of applied velocity, initial porosity, and void size is used as the reference configuration for the analysis. Higher and lower values of V, ϕ and f^0 will be used in the calculations presented in Sections 4.2, 4.3 and 4.4, respectively.

Subplots 4(a), ..., (e) correspond to a simulation with actual pores and material modeled with von Mises plasticity. The contours show the central section of a layer of pores (this is the reason for displaying a cross-sectional view at $Z = -0.074$ mm). For $U_Y = 0.05$ mm, greater plastic deformation is observed on the surface of the pores compared to the matrix material (the material between the pores), which remains practically undeformed. The pores maintain their initial spherical shape (further elaboration on this matter will be provided later in the text). The deformation is relatively uniform across all pores, except for those in the layers closer to the free surface and farther from the central section of the notch –see green arrows in 4(a)–, where lower hydrostatic stress slows their growth. For a larger imposed displacement of 0.125 mm, the effective plastic strain on the surface of the voids approaches 1, which is approximately ten times greater than in the intervoid material. The voids develop an ellipsoidal shape, elongated in the direction perpendicular to the applied load (more detailed discussion on this topic will be included later in this paragraph). The deformation of all pores is relatively uniform, with exceptions in layers closer to the free surface and farther from the center of the notch. The observation that void layers nearer to the free surface and further from the center of the notch are less deformed holds consistently across all calculations involving actual voids presented in this paper, and will not be reiterated in the manuscript to avoid redundancy. When the imposed displacement reaches 0.25 mm, the pores develop a markedly elongated shape perpendicular to the loading direction, driven by tensile stresses along the X-direction opposing the reduction of the notched cross-section. Note that we have observed similar behavior of the voids when examining specimen cross-sections at $X =$ constant: the pores elongate along the Z-direction due to tensile stresses induced by the plane strain constraint (the results are not shown for the sake of brevity). For $U_Y = 0.375$ mm, the elongation of the pores along the X-direction has significantly reduced the intervoid ligaments stretching parallel to the loading direction, resulting in substantial plastic deformation along rows of pores located at planes $Y =$ constant. In addition, the variability in pore growth is significant, with considerable differences in size among individual voids. The distribution of void sizes is accompanied by heterogeneous patterns of effective plastic strain, with some voids exhibiting high strain values exceeding 2 on their surface. For $U_Y = 0.5$ mm some pores have been observed to continue growing, developing nearly square cross-sections due to the coalescence of adjacent voids caused by the narrowing of the intervoid ligament (no *actual* pore union has occurred as no fracture criterion has been applied), while others have unloaded, maintaining the same shape and size as in previous loading stages. Coalescence resulting from internal necking of the intervoid ligament is commonly observed in ductile fracture process (Benzerga and Leblond, 2010). It will be shown in Section 4.2 that a different coalescence mechanism –direct impingement– occurs for higher applied velocities. The growth of pores generates localization bands along planes where $Y =$ constant, with the thickness of these bands determined by the current size of the voids. The pores regularize the localization process, which is largely insensitive to the mesh but strongly influenced by the porous microstructure. Among all the pores, those situated in the third row furthest from the central section of the notch exhibit the most significant growth (recall that the central section of the notch corresponds to the plane $Y = 0$). Plastic deformations exceed 4 on the surface of these voids and reach 3 in the intervoid ligaments. A more detailed illustration of the evolution of the size and shape of the pores during loading is provided in Figs. 5 and 6, which present 3D reconstructions of the surfaces of voids 1 and 2, respectively, as indicated in subplot 4(a). The void geometry is visualized by displaying the convex hull encompassing the void's surface. The origin of the Cartesian coordinate system (X', Y', Z') is located at the center of the void, with X', Y' and Z' being parallel to the loading axes X, Y and Z. Voids 1 and 2 exhibit similar growth up to an imposed displacement of 0.25 mm. The initially spherical pores elongate along the X' and Z' axes, developing an ellipsoidal morphology flattened in the loading direction. However, as the imposed displacement increases beyond 0.25 mm, void 2 demonstrates a more rapid growth rate, adopting a prismatic-like configuration with quasi-planar faces, while void 1 retains its ellipsoidal shape. Figs. 7(a) and 7(b) show the evolution of the ratios $\frac{b}{a}$ and $\frac{c}{a}$ with the imposed displacement for the voids shown in Figs. 5 and 6, respectively, where a, b, and c represent the distances between material points on the surface of the voids connected along the X', Y', and Z' axes, respectively. The yellow markers represent the imposed displacement values used in the 3D reconstructions shown in Figs. 5 and 6. The results for void 1 shown in Fig. 7(a) illustrate that the ratio $\frac{c}{a}$ remains roughly 1 throughout the entire loading process, indicating uniform growth in the X' and Z' directions. In contrast, the ratio $\frac{b}{a}$ exhibits a nonlinear evolution with the imposed displacement. Initially, $\frac{b}{a}$ decreases until stabilizing at approximately 0.72 for displacements exceeding 0.25 mm, when the void stops growing. The results presented in Fig. 7(b) show that for void 2, the ratio $\frac{c}{a}$ also remains constant at 1 throughout the entire loading process. However, unlike for void 1, the proportion $\frac{b}{a}$ reaches a minimum of 0.72 at a displacement of 0.3 mm, and then increases. This increase of $\frac{b}{a}$ indicates that the void has coalesced with adjacent pores along the X' and Z' directions and is now growing faster along the Y' direction, consistent with the observations in subplots 4(a), ..., (e) and Fig. 6.

Subplots 4(a'), ..., (e') correspond to a calculation with homogenized porosity and material modeled with Gurson-Tvergaard plasticity and microinertia effects. For $U_Y = 0.05$ mm, the plastic deformation in the specimen reaches approximately 0.052 (the contours of plastic deformation appear slightly lighter blue in the notched section). In the absence of discrete pores, deformation remains uniform across the entire notch. The stress triaxiality within the notch reaches 4 (although triaxiality contours are not shown, the stress triaxiality value is provided for completeness). Increasing the imposed displacement to 0.125 mm raises the effective plastic strain to 0.12. Recall that for the same imposed displacement, in the calculation with actual voids the plastic strain on the surface of the pores is nearly ten times greater. This occurs because, in simulations incorporating homogenized porosity, plastic strain is a macroscopic measure that represents the average value at the unit cell scale. In contrast, simulations with discrete voids allow direct observation of the microscopic plastic deformation field surrounding individual voids (a detailed comparison between the macroscopic plastic strain fields obtained from simulations with discrete voids and those with homogenized porosity is presented later in this section). Further increases in the imposed displacement to 0.25 mm and 0.375 mm result in incipient heterogeneity in the plastic strain field of the notched section. Near the free surface, the plastic strain is reduced (see green arrow in subplot (c')), while a localized deformation band, illustrated by a light bluish color, appears at the same location where the largest void growth was observed in the calculation with discrete voids. The plastic localization band has a finite width due to the regularization effect of microinertia (further elaboration on this matter will be provided later in the text). The band extends across several elements of the finite element grid. For $U_Y = 0.5$ mm, the effective plastic strain and the stress triaxiality within the localized band reach 0.6 and 15, respectively. While this value of plastic strain is approximately 7 times smaller than the largest plastic strain attained on the pores surface in the calculation involving discrete voids (see previous paragraph), it should be noted that the distributions of plastic deformation within the notch in simulations with explicit pores, and with homogenized porosity accounting for microinertia, are qualitatively similar (compare subplots (e) and (e')).

Subplots 4(a"), ..., (e") correspond to a simulation with homogenized porosity and material modeled with Gurson-Tvergaard plasticity and without microinertia effects. Recall that the standard Gurson-Tvergaard model predicts that the mechanical behavior of the material is independent of void size. For an imposed displacement of 0.05 mm, the effective plastic strain contours in the notched section are uniform, showing a plastic strain of 0.047, slightly smaller than the result obtained with microinertia. An increase in the imposed displacement to 0.125 mm results in the effective plastic strain in the notched section increasing to 0.12 (the same value reached in the simulation with microinertia). For 0.25 mm, a narrow localization band appears at the same position observed in the microinertia calculation (where the largest void growth occurred in the discrete pores simulation). The maximum plastic strain within the band is approximately 1, and unlike in the calculation with microinertia, the band width consists of only 1 element, indicating that neglecting microinertia leads to mesh-sensitive results for localization predictions. Further increase in the imposed displacement to 0.375 mm demonstrate the spurious development of the localization band, which shows a zigzag irregular path as it jumps from one row of elements to another. For a displacement of 0.5 mm, the maximum strain within the band exceeds 1.5, three times higher than in the simulation with microinertia.

Further analysis of the impact of the actual porous microstructure and microinertia on plastic strain development within the specimen is presented in Fig. 8, which illustrates the evolution of the effective plastic strain $\bar{\varepsilon}^p$ along the Lagrangian coordinate Y for the same simulations shown in Fig. 4. The results from the calculation with actual pores represent the volume-averaged effective plastic strain in unit cells with centers located at $X = 0.074$ mm and $Z = -0.074$ mm (there are 14 unit cells along the notch in the Y direction). The volume-averaged plastic strain is obtained by weighting the local plastic strain of each grid element by its volume and integrating over the entire unit cell. The results from the homogenized porosity calculations are obtained from elements along the path defined by $X = Z = 0$. Note that the plastic strains outside the notched region are nearly zero.

Subplot 8(a) corresponds to an imposed displacement of 0.05 mm —see 4(a)-(a')-(a"). The calculations using both actual voids and homogenized porosity yield qualitatively similar results, with the effective plastic strain within the notch

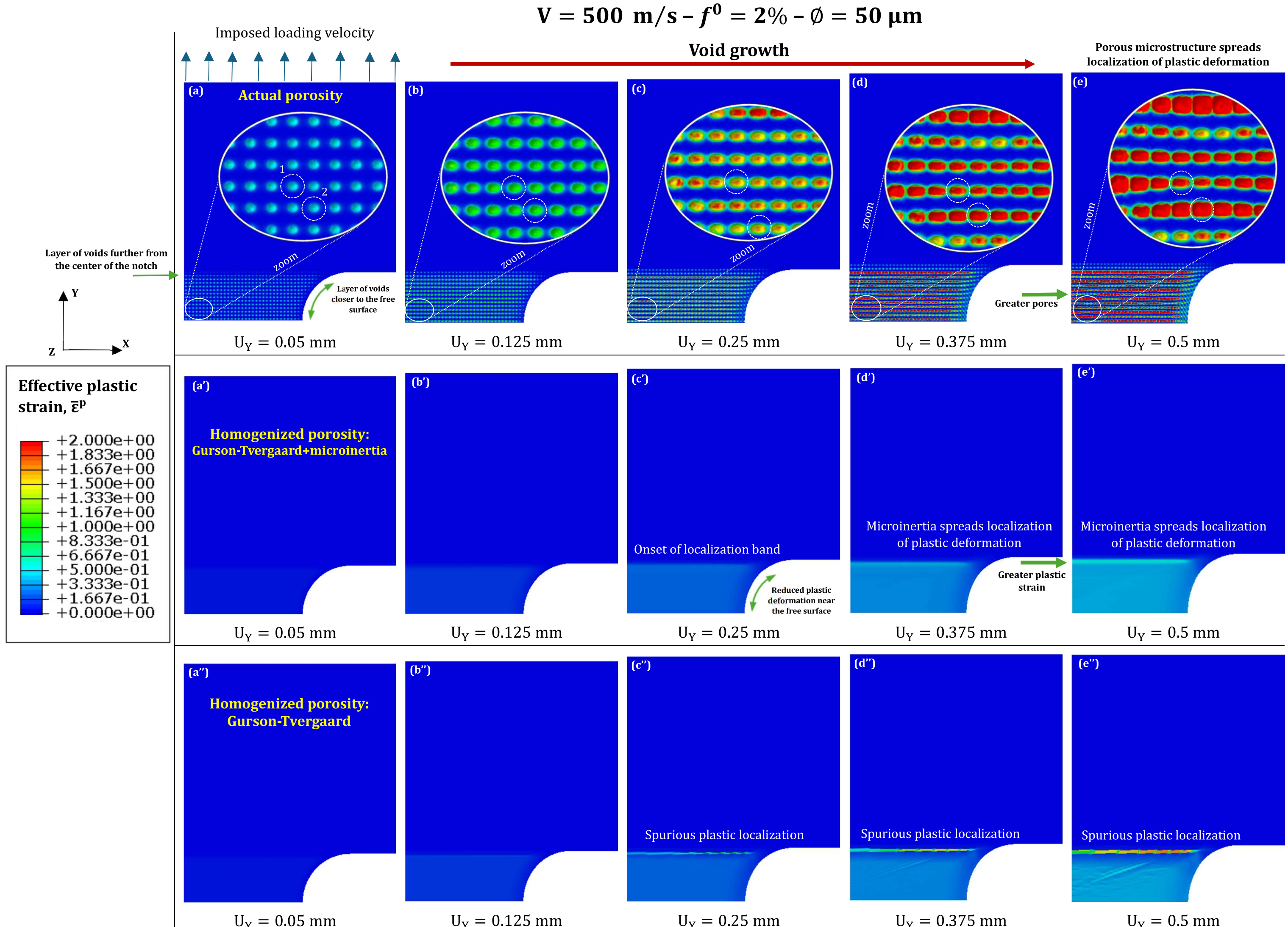

Figure 4: Finite element calculations for an imposed loading velocity $V = 500$ m/s, initial void volume fraction in the notched region $f^0 = 2\%$ and initial diameter of the voids $\phi = 50$ μm. Contours of effective plastic strain $\bar{\varepsilon}^p$ for different imposed displacement values: (a)-(a')-(a") $U_Y = 0.05$ mm, (b)-(b')-(b") $U_Y = 0.125$ mm, (c)-(c')-(c") $U_Y = 0.25$ mm, (d)-(d')-(d") $U_Y = 0.375$ mm and (e)-(e')-(e") $U_Y = 0.5$ mm. Cross-section view at $Z = -0.074$ mm. Subplots (a), ..., (e) correspond to calculation with actual pores and material modeled with von Mises plasticity. Subplots (a'), ..., (e') correspond to calculation with homogenized porosity and material modeled with Gurson-Tvergaard plasticity and microinertia effects. Subplots (a"), ..., (e") correspond to calculation with homogenized porosity and material modeled with Gurson-Tvergaard plasticity and without microinertia effects. For interpretation of the references to color in this figure legend, the reader is referred to the web version of this article.

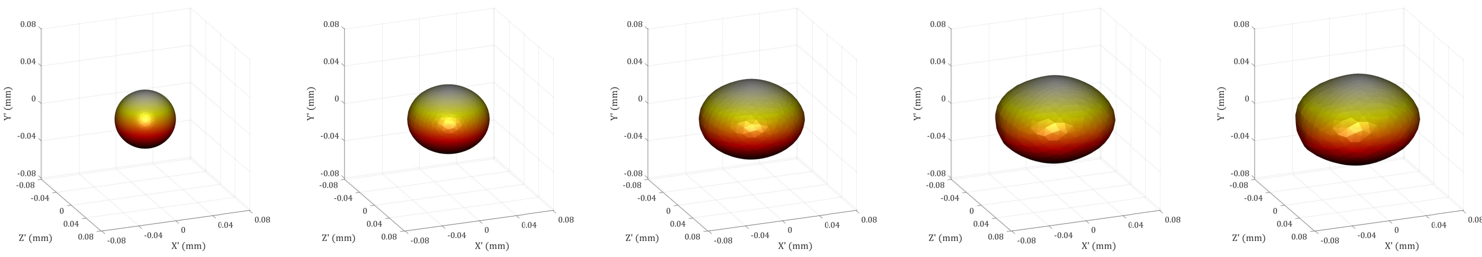

(a) (b) (c) (d) (e)

Figure 5: Finite element calculations for an imposed loading velocity $V = 500$ m/s, initial void volume fraction in the notched region $f^0 = 2\%$ and initial diameter of the voids $\phi = 50$ μm. Results obtained from simulation with actual pores and material modeled with von Mises plasticity. 3D reconstructions of the surface of void 1 indicated in Fig. 4(a) for different imposed displacement values: (a) $U_Y = 0.05$ mm, (b) $U_Y = 0.125$ mm, (c) $U_Y = 0.25$ mm, (d) $U_Y = 0.375$ mm and (e) $U_Y = 0.5$ mm. The origin of the Cartesian coordinate system (X', Y', Z') is located at the center of the void, with X', Y' and Z' being parallel to the X, Y and Z axes, respectively.

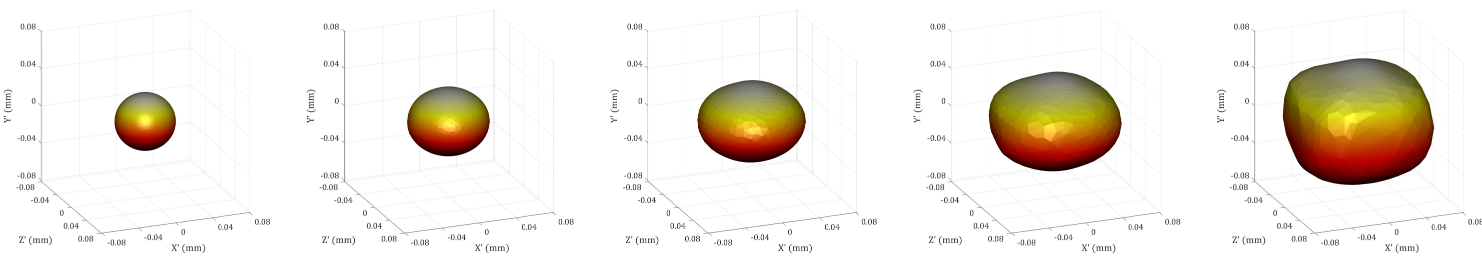

(a) (b) (c) (d) (e)

Figure 6: Finite element calculations for an imposed loading velocity $V = 500$ m/s, initial void volume fraction in the notched region $f^0 = 2\%$ and initial diameter of the voids $\phi = 50$ μm. Results obtained from simulation with actual pores and material modeled with von Mises plasticity. 3D reconstructions of the surface of void 2 indicated in Fig. 4(a) for different imposed displacement values: (a) $U_Y = 0.05$ mm, (b) $U_Y = 0.125$ mm, (c) $U_Y = 0.25$ mm, (d) $U_Y = 0.375$ mm and (e) $U_Y = 0.5$ mm. The origin of the Cartesian coordinate system (X', Y', Z') is located at the center of the void, with X', Y' and Z' being parallel to the X, Y and Z axes, respectively.

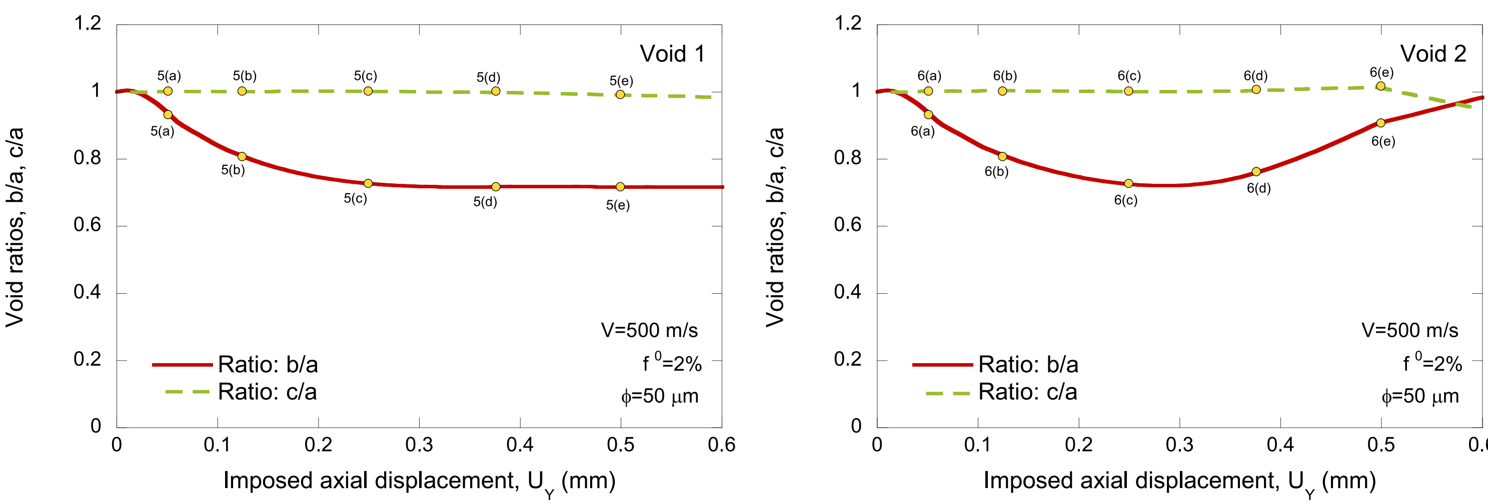

(a) (b)

Figure 7: Finite element calculations for an imposed loading velocity $V = 500$ m/s, initial void volume fraction in the notched region $f^0 = 2\%$ and initial diameter of the voids $\phi = 50$ μm. Results obtained from simulation with actual pores and material modeled with von Mises plasticity. Evolution of the void ratios, $\frac{b}{a}$ and $\frac{c}{a}$, with the imposed displacement U_Y. (a) Void 1 indicated in Fig. 4(a). (b) Void 2 indicated in Fig. 4(a). The yellow markers represent the imposed displacement values used in the 3D reconstructions of the pores shown in Figs. 5 and 6.

remaining relatively constant. However, the homogenized porosity model with microinertia effects produces slightly higher plastic strain values, approximately 10% larger than those obtained from the discrete void model and the quasi-static Gurson-Tvergaard framework.

Subplot 8(b) corresponds to an imposed displacement of 0.25 mm —see 4(c)-(c')-(c"). In the calculation with discrete voids, the effective plastic strain within the notch ranges from 0.17 to 0.26, reflecting variations in plastic deformation across different unit cells, which become significant at higher imposed displacements due to increased heterogeneity in void growth (compare 4(a) and 4(c)). The average plastic deformation within the notch for the calculation with discrete pores is slightly smaller than that observed in simulations where the material is modeled with homogenized porosity. The calculation performed using Gurson-Tvergaard plasticity and microinertia effects predicts that the plastic strain remains approximately constant at ≈ 0.22 within the notch, with a slight increase occurring at 1.7 mm from the center of the specimen due to the onset of the localization band indicated in 4(c') —refer to the enlarged image of the localization band. The calculation performed with the standard (quasi-static) Gurson-Tvergaard model produces results qualitatively similar to those from the simulation incorporating microinertia effects, with plastic strain remaining relatively constant within the notch, except for the localization band that develops at 1.7 mm from the specimen center. Note that disregarding microinertia effects leads to a significant increase in plastic strain within the localization band, which reaches a peak of nearly 0.4 —refer to the enlarged image of the localization band. Furthermore, the plastic localization is confined to a narrow region defined by a single layer of elements. These results clearly indicate that microinertia slows down and regularizes plastic localization.

Subplot 8(c) presents results for an imposed displacement of 0.5 mm —see 4(e)-(e')-(e"). Note that in the calculation with discrete pores, the oscillations in the average effective plastic strain across the cells become increasingly pronounced at higher displacements due to greater heterogeneity in void growth as the load progresses. The plastic strain variation ranges from 0.17 to 0.52, with the unit cell exhibiting the lower average effective plastic strain retaining the same value as observed at the lower displacement of 0.25 mm, indicating that it has unloaded. Furthermore, the average plastic strain in the voided cells is slightly smaller than that observed in simulations using both the standard Gurson-Tvergaard model and the dynamic homogenization approach introduced by Molinari and Mercier (2001). The calculation conducted using Gurson-Tvergaard plasticity and microinertia effects predicts that the plastic strain remains approximately constant at around 0.38, except for a surge at $Y = 1.7$ mm, caused by the formation of the plastic localization band indicated in 4(e'). Note that the band exhibits a finite thickness as a result of the regularizing effect of microinertia on plastic localization, with a peak strain of 0.61 —refer to the enlarged image of the localization band. The results obtained from the calculation using the standard version of the Gurson-Tvergaard model indicate that excluding microinertia effects causes the thickness of the plastic localization band to narrow to a single layer of elements –illustrating the occurrence of spurious localization– while the peak strain within the band increases to 0.74 (this value is lower than the peak strain within the band reported in the discussion of Fig. 4, which referred to the entire notch). Note also the difference in localization patterns between the calculations using homogenized porosity and the one incorporating discrete voids.

While homogenized porosity models predict a single, concentrated band of localized deformation, the explicitly resolved void calculations reveal pronounced oscillations in the Y direction (as mentioned before). These oscillations stem from a more diffuse localization process in the discrete void simulations, where multiple layers of voids continue to grow throughout the loading process, see Fig. 4(a)-(e).

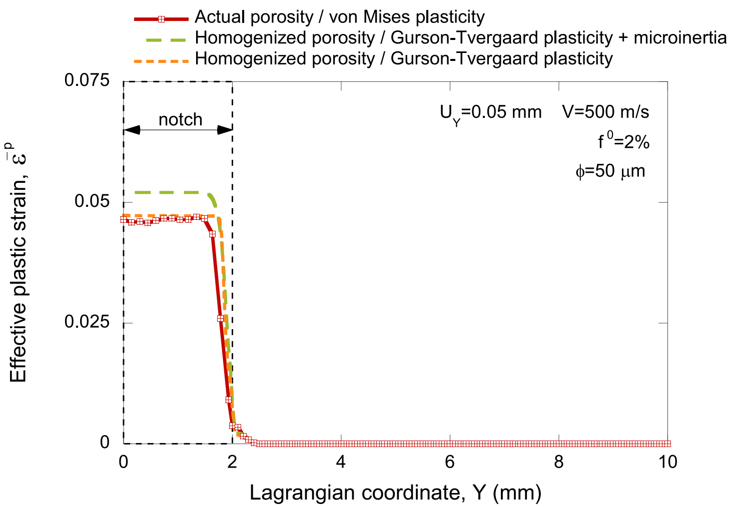

(a)

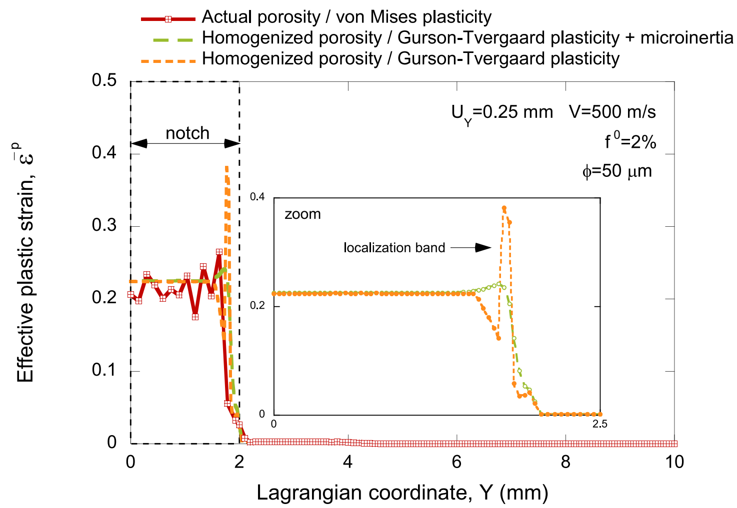

(b)

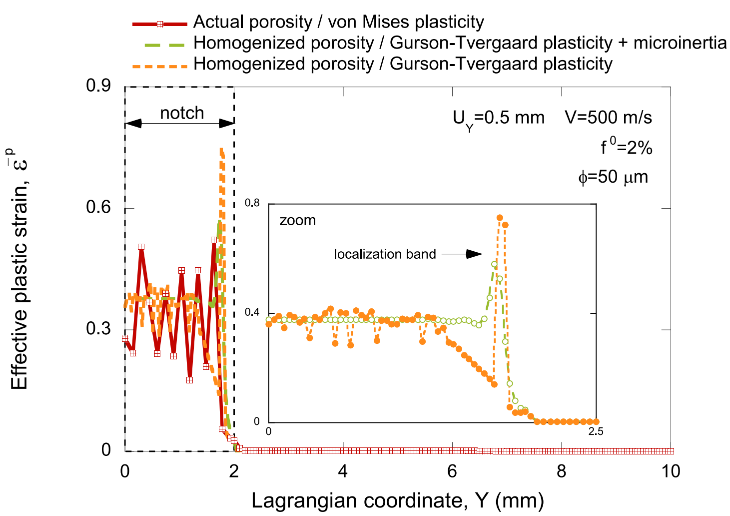

(c)

Figure 8: Finite element calculations for an imposed loading velocity $V = 500$ m/s, initial void volume fraction in the notched region $f^0 = 2\%$ and initial diameter of the voids $\phi = 50$ μm. Evolution of the macroscopic effective plastic strain $\bar{\varepsilon}^p$ with the Lagrangian coordinate Y. Comparison of results obtained with actual pores and material modeled with von Mises plasticity (red solid line), homogenized porosity and material modeled with Gurson-Tvergaard plasticity and microinertia effects (green dashed line) and homogenized porosity and material modeled with Gurson-Tvergaard plasticity and without microinertia effects (orange dotted line). The results from the calculation with actual pores represent the volume-averaged effective plastic strain in unit cells with centers located at $X = 0.074$ mm and $Z = -0.074$ mm. The results from the calculations with homogenized porosity correspond to a path along $X = Z = 0$. Data for different values of the imposed displacement: (a) $U_Y = 0.05$ mm (b) $U_Y = 0.25$ mm and (c) $U_Y = 0.5$ mm.

Figure 9(a) shows the evolution of the axial force F_Y versus the imposed axial displacement U_Y for the three calculations shown in Fig. 4. The force is measured on the $Y = 0$ surface of the specimen. The results obtained with actual pores, with homogenized porosity including microinertia effects, and with homogenized porosity without microinertia effects are represented by the red solid line, green dashed line, and orange dotted line, respectively (the same color coding used in Fig. 8). The force initially increases due to the strain hardening of the material. After reaching a peak at an imposed displacement of approximately 0.03 mm, the force begins to decrease. This reduction is caused by a combination of material softening, resulting from thermal effects and porosity growth, and geometric softening due to the thinning of the specimen (in the X direction). The oscillations observed in the F_Y-U_Y curves for simulations incorporating both actual pores and homogenized porosity with microinertia arise from the dynamic effects introduced by the porous microstructure (Jacques et al., 2012b). Following the attenuation of oscillations, the force in the simulation including microinertia matches the calculation employing the quasi-static Gurson-Tvergaard plasticity model. In contrast, the simulation incorporating actual pores exhibits a more rapid decline in force, indicative of an accelerated loss in load-bearing capacity.

Figure 9(b) displays the global normalized void volume fraction in the notch, f^{notch}/f^0, plotted against the imposed axial displacement U_Y. The results correspond to the calculations shown in Fig. 9(a), represented by the same color-coded solid, dashed, and dotted lines. The yellow markers indicate the axial displacements of the contour plots of Fig. 4. The simulations using the Gurson-Tvergaard plasticity model with and without microinertia yield different results only for values of U_Y greater than 0.25 mm. For $U_Y = 0.125$ mm, the values of f^{notch}/f^0 in the simulations using homogenized porosity with microinertia and without microinertia are 3.17 and 3.15, respectively. Microinertia leads to a minor 0.63% increase in porosity. In contrast, for $U_Y = 0.5$ mm, the corresponding values of f^{notch}/f^0 are 8.60 and 7.67, respectively, indicating a significant increase of 12.12% in average porosity in the notch when including microinertia. Moreover, the increased void volume fraction observed in the calculation incorporating discrete pores across all imposed displacement values contributes to greater material softening, which accelerates the decrease in force illustrated in Fig. 9(a) for large values of the imposed displacement. For instance, at $U_Y = 0.5$ mm the global porosity in the calculation with actual voids is 50% greater than in the simulation with homogenized porosity and without microinertia. Notably, the regularization effect of microinertia and discrete voids, which spreads plastic deformation throughout the notch, contributes to an increase in the global void volume fraction.

Figure 10 presents the local normalized void volume fraction, $f^{local}_{A,B}/f^0$, as a function of the imposed axial displacement, U_Y. For the simulation with discrete voids $f^{local}_{A,B}$ is measured within an individual unit cell of the notched region. In contrast, for the simulations employing homogenized porosity, $f^{local}_{A,B}$ is computed within a single finite element. This applies both to the case where Gurson-Tvergaard plasticity with microinertia effects is used, as well as to the case without microinertia effects. The subscripts A and B correspond to measurements taken outside and inside the plastic localization band that forms in the notch (see Fig. 4). The results correspond to the same calculations analyzed in Fig. 9, which are identified with identical colored solid, dashed, and dotted lines. The yellow markers represent the imposed displacement values used in the contour plots of Fig. 4.

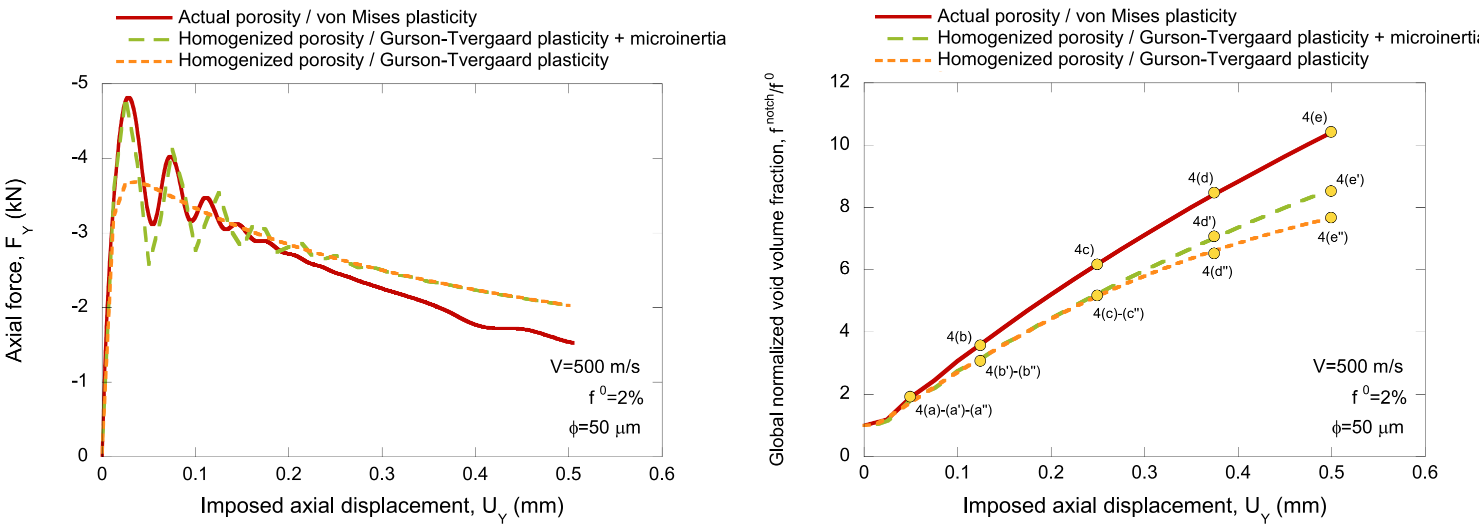

(a) (b)

Figure 9: Finite element calculations for an imposed loading velocity $V = 500$ m/s, initial void volume fraction in the notched region $f^0 = 2\%$ and initial diameter of the voids $\phi = 50$ μm. Comparison of results obtained with actual pores and material modeled with von Mises plasticity (red solid line), homogenized porosity and material modeled with Gurson-Tvergaard plasticity and microinertia effects (green dashed line) and homogenized porosity and material modeled with Gurson-Tvergaard plasticity and without microinertia effects (orange dotted line). (a) Axial force F_Y versus imposed axial displacement U_Y. The force is measured on the $Y = 0$ surface of the specimen. (b) Global normalized void volume fraction in the notch f^{notch}/f^0 versus imposed axial displacement U_Y. The yellow markers represent the imposed displacement values used in the contour plots of Fig. 4. For interpretation of the references to color in this figure legend, the reader is referred to the web version of this article.

The data in Fig. 10(a) pertain to a unit cell located outside the void layer with the fastest growth, as indicated in Fig. 4(e), and outside the plastic localization band shown in Figs. 4(e') and 4(e"). The center of the unit cell in the simulation with discrete voids is located at coordinates $X = 1.114$ mm, $Y = 1.559$ mm, and $Z = -0.074$ mm, while the finite element selected in the calculations with homogenized porosity is at coordinates $X = 1.147$ mm, $Y = 1.626$ mm, and $Z = -0.074$ mm. The measurements in the calculations with discrete voids and with homogenized porosity were taken at nearly the same location. At the onset of loading, the local void volume fraction increases nearly linearly with the imposed axial displacement, and for displacements below 0.2, the value of f_A^{local} is virtually the same for the calculation with discrete voids and the simulations with homogenized porosity. However, the value of f_A^{local} eventually ceases to increase in all three simulations. Saturation of the local normalized void volume fraction first occurs in the Gurson-Tvergaard model without microinertia effects, reaching a value of 5.4, followed by the calculation with discrete voids at 6.5, and lastly in the Gurson-Tvergaard model with microinertia effects at 9.95. The saturation marks the onset of elastic unloading, with earlier saturation indicating an earlier onset of plastic localization, occurring first when microstructural inertia is neglected.

Figure 10(b) presents results for a unit cell located immediately above the unit cell included in Fig. 10(a), which lies within the void layer exhibiting the fastest growth, as indicated in Fig. 4(e), and inside the plastic localization band shown in Figs. 4(e') and 4(e"). The center of the unit cell in the calculation with discrete voids is located at coordinates $X = 1.114$ mm, $Y = 1.708$ mm, and $Z = -0.074$ mm, while the finite element selected in the calculations with homogenized porosity is at coordinates $X = 1.128$ mm, $Y = 1.730$ mm, and $Z = -0.074$ mm. The local void volume fraction increases monotonically throughout the entire loading process in all three calculations, and the results are quantitatively very similar for values of U_Y below 0.13. For larger imposed axial displacements, the local void volume fraction increases rapidly in the simulation performed with the standard Gurson-Tvergaard model without microinertia effects, indicating a rapid development of plastic deformation. In contrast, the value of f_B^{local} in the localization band increases at a significantly slower rate in calculations utilizing discrete voids and the Gurson-Tvergaard model with microinertia effects, highlighting the stabilizing influence of microstructural inertia on plastic flow, consistent with the observations made from the contour plots in Fig. 4. The porosity evolution predicted by the homogenized model with microinertia shows good agreement with the results from simulations considering actual porosity. The comparison with Fig. 9(b) demonstrates that microstructural inertia increases global porosity within the notch by spreading plastic deformation, while simultaneously reducing local deformation within the localization band.

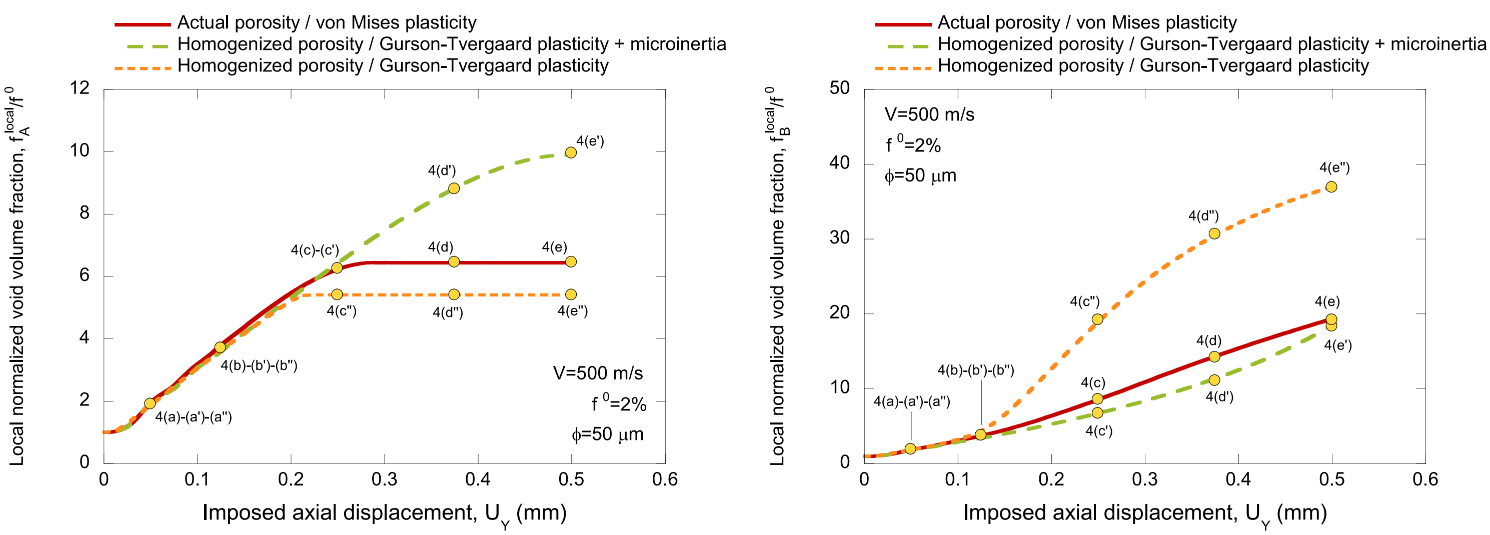

(a) (b)

Figure 10: Finite element calculations for an imposed loading velocity $V = 500$ m/s, initial void volume fraction in the notched region $f^0 = 2\%$ and initial diameter of the voids $\phi = 50$ μm. Local normalized void volume fraction $f_{A,B}^{local}/f^0$ versus imposed axial displacement U_Y. The subscripts A and B correspond to measurements taken outside and inside the plastic localization band that forms within the notch. Comparison of results obtained with actual pores and material modeled with von Mises plasticity (red solid line), homogenized porosity and material modeled with Gurson-Tvergaard plasticity and microinertia effects (green dashed line) and homogenized porosity and material modeled with Gurson-Tvergaard plasticity and without microinertia effects (orange dotted line). (a) The center of the unit cell in the calculation with discrete voids is located at coordinates $X = 1.114$ mm, $Y = 1.559$ mm, and $Z = -0.074$ mm, while the finite element selected in the calculations with homogenized porosity is at coordinates $X = 1.147$ mm, $Y = 1.626$ mm, and $Z = -0.074$ mm. (b) The center of the unit cell in the calculation with discrete voids is located at coordinates $X = 1.114$ mm, $Y = 1.708$ mm, and $Z = -0.074$ mm, while the finite element selected in the calculations with homogenized porosity is at coordinates $X = 1.128$ mm, $Y = 1.730$ mm, and $Z = -0.074$ mm. The yellow markers represent the imposed displacement values used in the contour plots of Fig. 4. For interpretation of the references to color in this figure legend, the reader is referred to the web version of this article.

4.2. The effect of loading rate

Figure 11 shows contours of effective plastic strain for different imposed displacement values: (a)-(a')-(a") $U_Y = 0.05$ mm, (b)-(b')-(b") $U_Y = 0.1$ mm, (c)-(c')-(c") $U_Y = 0.15$ mm, and (d)-(d')-(d") $U_Y = 0.2$ mm. The initial void volume fraction in the notched region is $f^0 = 2\%$ and the initial diameter of the voids is $\phi = 50$ μm. The difference from Fig. 4 is that the loading velocity has been reduced by a factor of five to $V = 100$ m/s. The color coding of the isocontours is the same used in Fig. 4. The plots display a cross-sectional view at $Z = -0.074$ mm, see the Lagrangian coordinate system in Fig. 1.

Subplots 11(a), ..., (d) correspond to a calculation involving actual pores. For an imposed displacement of $U_Y = 0.05$ mm, the pores retain their initial spherical shape, but exhibit heterogeneous growth with a gradient of increasing plastic deformation towards the center of the specimen. The maximum effective plastic strain at the surface of the void nearest the origin of the Lagrangian coordinate system —see Fig. 1— exceeds 0.5. Increasing the imposed displacement to 0.1 mm causes some voids to develop an ellipsoidal shape, elongated perpendicular to the loading direction, with reduced intervoid ligaments stretching parallel to the loading direction. Compared to the calculation shown in Fig. 4(a), ..., (e), decreasing the applied velocity to 100 m/s leads to earlier voids interaction. For a greater displacement of $U_Y = 0.15$ mm, some pores display a square-like cross-section due to intervoid ligament necking and coalescence with neighboring voids in the same $Y =$ constant plane, reaching plastic deformations exceeding 2.5 (e.g., void 1 in Fig. 11(a)). Meanwhile, other voids remain much smaller in size, are unloaded, and maintain their initially spherical shape, with a maximum plastic deformation of 0.8 (e.g., void 2 in Fig. 11(a)), indicating that the porosity evolution has (already) localized. For $U_Y = 0.2$ mm, large plastic deformation is shown by only a few voids from different $Y =$ constant planes. A more detailed depiction of the evolution in size and shape of the pores during loading is shown in Figs. 12 and 13. These figures present 3D reconstructions of the surfaces of voids 1 and 2, respectively, as indicated in Fig. 11(a). Fig. 12 illustrates that void 1 exhibits a continuous increase in volume with loading. The pore transitions from a spherical to an ellipsoidal form at a displacement of 0.1 mm. As the loading process continues to $U_Y = 0.15$ mm, the void develops a prismatic-like shape with flattened faces due to interaction with adjacent pores. For a displacement of 0.2 mm, the void can no longer stretch along the X' and Z' directions, instead elongating parallel to the loading direction. Moreover, Fig. 13 demonstrates that void 2 only shows mild deformation at the beginning of loading, developing an ellipsoidal shape for imposed displacements less than 0.15 mm. Further increases in loading up to 0.2 mm do not change the size and shape of the pore, indicating that the void is unloaded. The distinctly different behaviors of voids 1 and 2 underscore the heterogeneous deformation field in the notched sample. Compared to the simulation at 500 m/s depicted in Fig. 4(a), ..., (e), the spatial distribution of plastic deformation within the notch in Fig. 11(a), ..., (e) is less uniform (due to the non-uniform spatial distribution of voids growth). The concentration of plastic deformation in specific pores at various locations indicates a less regularized localization process due to reduced inertia effects. For the same imposed displacement of 0.2 mm, pores in the calculation performed at 500 m/s were smaller and exhibited less plastic strain on their surfaces —see Figs. 4 (a), ..., (e). This highlights the stabilizing effect of inertia which delays plastic localization and constrains void growth.

Subplots 11(a'), ..., (d') correspond to a calculation with homogenized porosity and microinertia effects. For $U_Y = 0.05$ mm, the deformation field in the specimen remains uniform, with the plastic strain not exceeding 0.05. The stress triaxiality within the notch reaches 4. Increasing the imposed displacement to 0.1 mm leads to heterogeneity in the strain field, triggering the onset of plastic deformation in a narrow strip (which corresponds to the light blue thin band indicated with a green arrow). The plastic strain within the band reaches 0.12, while in the notched section outside the band the plastic strain is 0.1. The stress triaxiality within the localization band reaches 5. At an imposed displacement of 0.15 mm, plastic localization and porosity growth concentrate within a single layer of elements (for the selected mesh size), as the reduced applied velocity —compared to the 500 m/s case in Fig. 4— weakens the regularizing effect of microinertia. For a displacement of 0.2 mm, the deformation in the band reaches 1.1, sharply dropping to 0.15 in the grid elements immediately adjacent.

Subplots 11(a”), ..., (d”) correspond to a calculation with homogenized porosity without microinertia effects. The plastic deformation contours show plastic strain concentrating within a single layer of elements for low values of the imposed displacement. This highlights the pathological mesh dependence of the localization process in calculations using standard (quasi-static) Gurson-Tvergaard plasticity. Note that for $U_Y = 0.1$ mm, the plastic deformation inside the main localization band, indicated by a green arrow, reaches 0.17, which is 30% higher than in the case including microinertia. Adjacent to this localization band, the plastic strain drops to 0.1, representing a 70% variation in plastic strain within a single layer of grid elements. Further increasing the imposed displacement to 0.15 mm and 0.2 mm results in a large rise in plastic strain within the band, while the rest of the notch remains *virtually* unloaded.

Figure 14 provides contours of effective plastic strain for different values of the imposed displacement U_Y, obtained from calculations with an initial void volume fraction of $f^0 = 2\%$ and an initial void diameter of $\phi = 50$ μm. The loading velocity has been increased by a factor of 2.5 compared to Fig. 11, reaching $V = 250$ m/s. The color coding of the isocontours is the same used in Fig. 11. The plots display a cross-sectional view at $Z = -0.074$ mm.

Subplots 14(a), ..., (e) correspond to a calculation involving discrete voids. For an imposed displacement of $U_Y =$ 0.05 mm, the pores grow homogeneously throughout the notched region while maintaining their initial spherical shape. Increasing the imposed displacement to 0.1 mm results in the pores adopting an ellipsoidal form, elongated perpendicular to the loading direction. The heterogeneity in pore shape and size becomes noticeable at an imposed displacement of 0.2 mm. Some voids have developed more pronounced elliptical shapes than others, with effective plastic strains reaching a maximum of 2.2. However, the heterogeneity in void growth is less pronounced compared to the calculation at 100 m/s (see subplots 11(d) and 14(c)), demonstrating that the increase in inertia effects with loading velocity leads to more uniform pore growth and delays localization (i.e., increasing loading velocity leads to greater microstructural inertia). A further increase in the imposed displacement to 0.3 mm results in a broad range of void sizes and shapes within the notched region, see subplot (d). Some pores exhibit a square-like cross-section due to coalescence with neighboring voids in the same $Y =$ constant plane, while others remain significantly smaller, unloaded, and retain the elliptical shape observed at lower displacements. For $U_Y = 0.35$ mm, significant plastic deformation is evident across various arrays of square-like cross-section voids from different $Y =$ constant planes, connected through plastic localization bands parallel to the loading direction. A detailed representation of the evolution in pore size and shape during loading is provided in Figs. 15 and 16 which show 3D reconstruction of voids 1 and 2 indicated in subplot 14(a) —these are the same voids

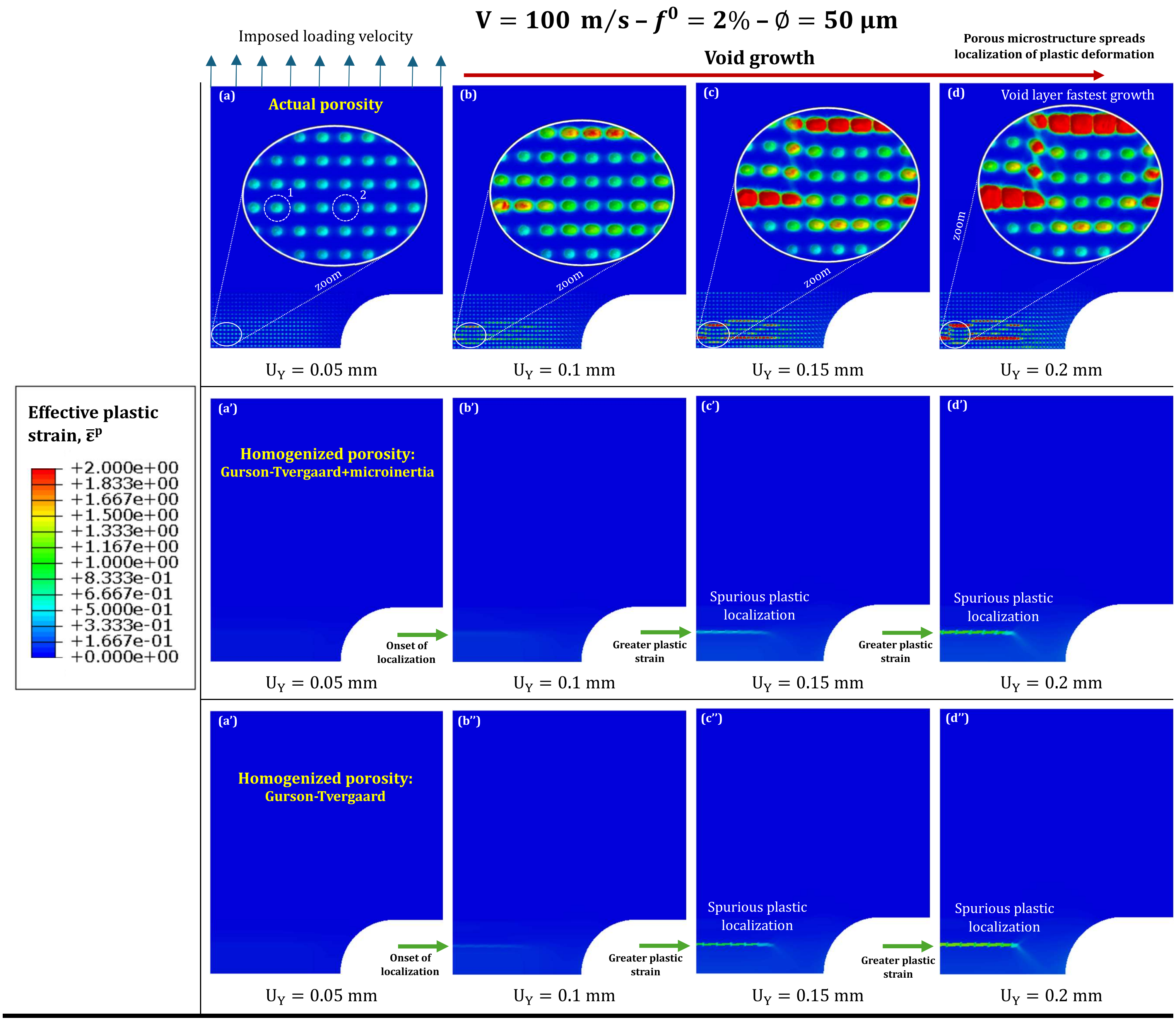

Figure 11: Finite element calculations for an imposed loading velocity $V = 100$ m/s, initial void volume fraction in the notched region $f^0 = 2\%$ and initial diameter of the voids $\phi = 50$ μm. Contours of effective plastic strain $\bar{\varepsilon}^p$ for different imposed displacement values: (a)-(a')-(a") $U_Y = 0.05$ mm, (b)-(b')-(b") $U_Y = 0.1$ mm, (c)-(c')-(c") $U_Y = 0.15$ mm, and (d)-(d')-(d") $U_Y = 0.2$ mm. Cross-section view at $Z = -0.074$ mm. Subplots (a), ..., (d) correspond to calculation with actual pores and material modeled with von Mises plasticity. Subplots (a'), ..., (d') correspond to calculation with homogenized porosity and material modeled with Gurson-Tvergaard plasticity and microinertia effects. Subplots (a"), ..., (d") correspond to calculation with homogenized porosity and material modeled with Gurson-Tvergaard plasticity and without microinertia effects. For interpretation of the references to color in this figure legend, the reader is referred to the web version of this article.

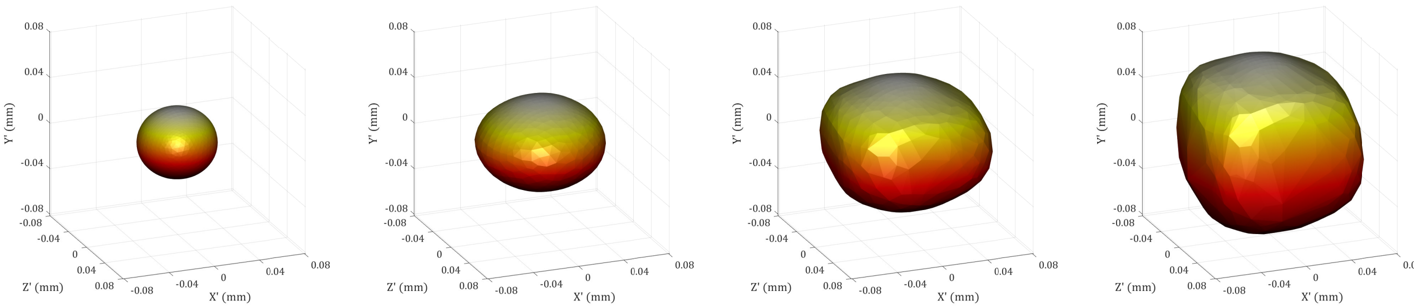

(a) (b) (c) (d)

Figure 12: Finite element calculations for an imposed loading velocity $V = 100$ m/s, initial void volume fraction in the notched region $f^0 = 2\%$ and initial diameter of the voids $\phi = 50$ μm. Results obtained from simulation with actual pores and material modeled with von Mises plasticity. 3D reconstructions of the surfaces of void 1 indicated in Fig. 11(a) for different imposed displacement values: (a) $U_Y = 0.05$ mm, (b) $U_Y = 0.1$ mm, (c) $U_Y = 0.15$ mm and (d) $U_Y = 0.2$ mm. The origin of the Cartesian coordinate system (X', Y', Z') is located at the center of the void, with X', Y' and Z' being parallel to the X, Y and Z axes, respectively.

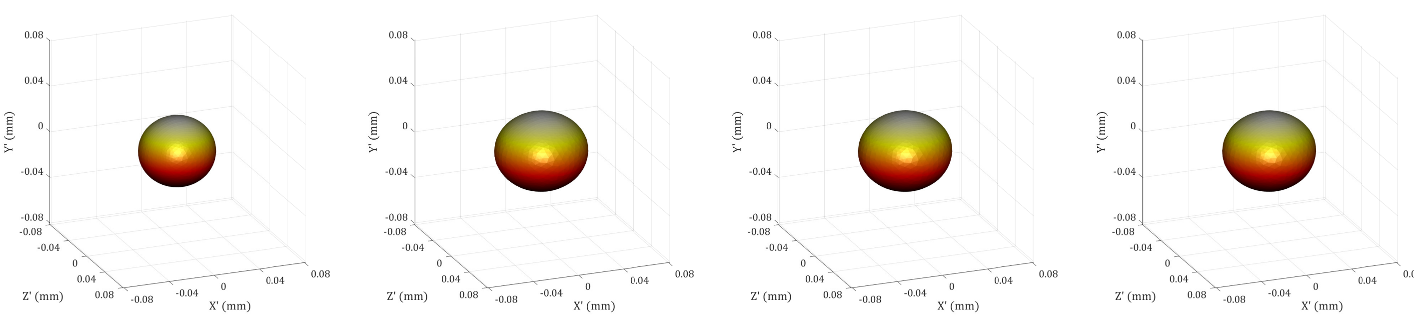

(a) (b) (c) (d)

Figure 13: Finite element calculations for an imposed loading velocity $V = 100$ m/s, initial void volume fraction in the notched region $f^0 = 2\%$ and initial diameter of the voids $\phi = 50$ μm. Results obtained from simulation with actual pores and material modeled with von Mises plasticity. 3D reconstructions of the surfaces of void 2 indicated in Fig. 11(a) for different imposed displacement values: (a) $U_Y = 0.05$ mm, (b) $U_Y = 0.1$ mm, (c) $U_Y = 0.15$ mm and (d) $U_Y = 0.2$ mm. The origin of the Cartesian coordinate system (X', Y', Z') is located at the center of the void, with X', Y' and Z' being parallel to the X, Y and Z axes, respectively.

shown in Figs. 12 and 13 for a calculation with lower imposed velocity of 100 m/s. Notice that the shape evolution of both voids is consistent with that observed at the loading rate of 100 m/s —see Figs. 15 and 16, and compare with Figs. 12 and 13. Void 1 transitions from a spherical to an ellipsoidal shape, eventually adopting a prismatic-like form at large displacements. In contrast, void 2 deforms into an ellipsoidal shape at intermediate displacements and maintains this configuration upon unloading for values of U_Y exceeding 0.2. The primary difference in void evolution between 100 m/s and 250 m/s pertains to size; increasing the loading velocity results in a reduction of void size for a given imposed displacement, attributed to the inertial effects that slows down void growth and plastic localization.

Subplots 14(a'), ..., (d') correspond to a calculation where the material is modeled using homogenized porosity and microinertia effects. For $U_Y = 0.05$ mm and 0.1 mm, the deformation field in the specimen remains uniform, with the plastic strain not exceeding 0.1. The maximum value of the stress triaxiality within the notch is approximately 5. An increase in the imposed displacement to 0.2 mm leads to the formation of a plastic localization band, indicated by the light blue region marked with a green arrow. At the same imposed displacement, but with a lower loading rate of 100 m/s, the plastic deformation band was more developed and confined to a single layer of elements –see subplots 11(d') and 14(c'). The effect of microinertia at elevated loading rates delays localization and causes plastic deformation to spread along the notch. The contour plots for larger imposed displacements of 0.3 mm and 0.35 mm, shown in subplots 14(d') and 14(e'), illustrate the gradual development of the plastic localization band, which has a finite width extending across several layers of elements within the grid due to the regularizing effect of the microstructural inertia. The maximum effective plastic strain reached for $U_Y = 0.35$ mm is approximately 0.7.

Subplots 14(a"), ..., (d") correspond to a calculation with homogenized porosity without considering microinertia effects. For an imposed displacement of 0.05 mm, the plastic deformation reaches a value of 0.045, which remains relatively constant throughout the notch, see subplot (a"). Further increase of U_Y to 0.1 mm triggers the onset of a localization band at the same position observed in the calculation with homogenized porosity and microinertia effects. The comparison of subplots 14(b') and 14(b") indicates that neglecting microstructural inertia causes the band to appear earlier in the loading process. Furthermore, neglecting microstructural inertia also accelerates the development of the plastic deformation band, which occupies a single row of elements, resulting in a spurious localization pattern that was not observed in the simulation conducted at the same speed using the dynamic homogenization model by Molinari and Mercier (2001) –compare subplots 14(c')-(d')-(e') and 14(c")-(d")-(e"). For an imposed displacement of 0.35 mm, the maximum plastic deformation within the band is approximately 1.4, which is double that observed in the simulation with homogenized porosity and microinertia effects.

Figure 17 includes contours of effective plastic strain corresponding to simulations with discrete pores, homogenized porosity including microinertia effects, and homogenized porosity without microinertia effects. The distinction between Figs. 11 and 14 lies in the loading velocity, which has been increased tenfold and fourfold, respectively, to 1000 m/s.

Subplots (a), ..., (e) correspond to a calculation involving actual pores. The imposed displacements are 0.05, 0.125,

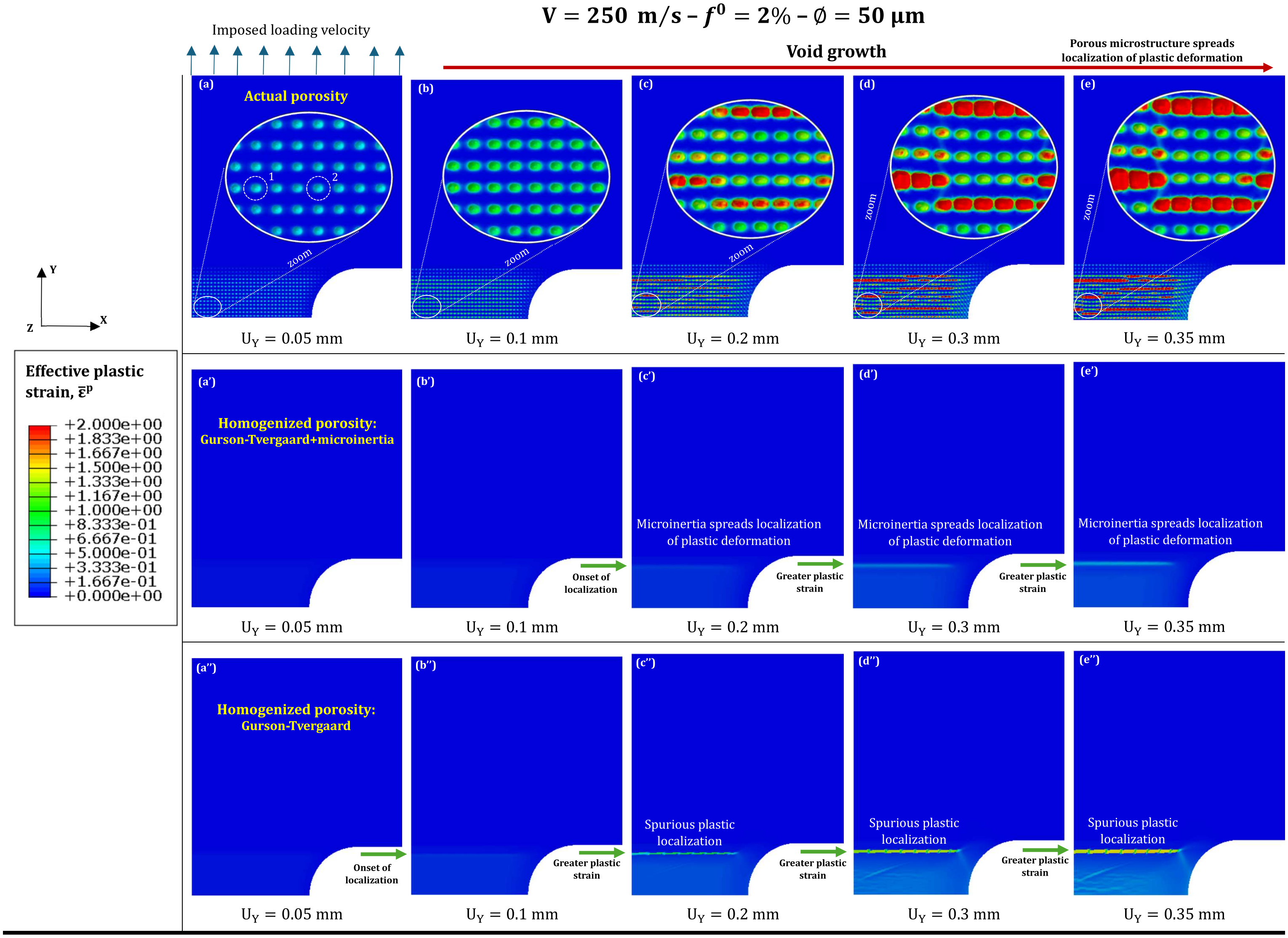

Figure 14: Finite element calculations for an imposed loading velocity $V = 250$ m/s, initial void volume fraction in the notched region $f^0 = 2\%$ and initial diameter of the voids $\phi = 50$ μm. Contours of effective plastic strain $\bar{\varepsilon}^p$ for different imposed displacement values: (a)-(a')-(a") $U_Y = 0.05$ mm, (b)-(b')-(b") $U_Y = 0.1$ mm, (c)-(c')-(c") $U_Y = 0.2$ mm, (d)-(d')-(d") $U_Y = 0.3$ mm and (e)-(e')-(e") $U_Y = 0.35$ mm. Cross-section view at $Z = -0.074$ mm. Subplots (a), ..., (d) correspond to calculation with actual pores and material modeled with von Mises plasticity. Subplots (a'), ..., (d') correspond to calculation with homogenized porosity and material modeled with Gurson-Tvergaard plasticity and microinertia effects. Subplots (a"), ..., (d") correspond to calculation with homogenized porosity and material modeled with Gurson-Tvergaard plasticity and without microinertia effects. For interpretation of the references to color in this figure legend, the reader is referred to the web version of this article.

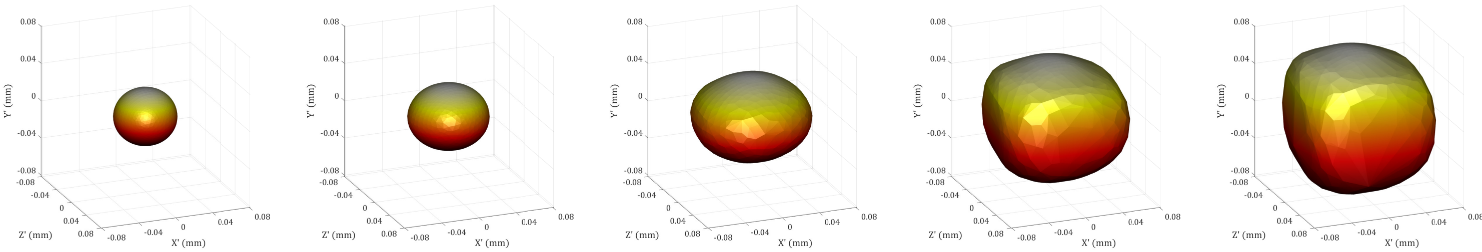

(a) (b) (c) (d) (e)

Figure 15: Finite element calculations for an imposed loading velocity $V = 250$ m/s, initial void volume fraction in the notched region $f^0 = 2\%$ and initial diameter of the voids $\phi = 50$ μm. Results obtained from simulation with actual pores and material modeled with von Mises plasticity. 3D reconstructions of the surfaces of void 1 indicated in Fig. 14(a) for different imposed displacement values: (a) $U_Y = 0.05$ mm, (b) $U_Y = 0.1$ mm, (c) $U_Y = 0.2$ mm, (d) $U_Y = 0.3$ mm and (e) $U_Y = 0.35$ mm. The origin of the Cartesian coordinate system (X', Y', Z') is located at the center of the void, with X', Y' and Z' being parallel to the X, Y and Z axes, respectively.

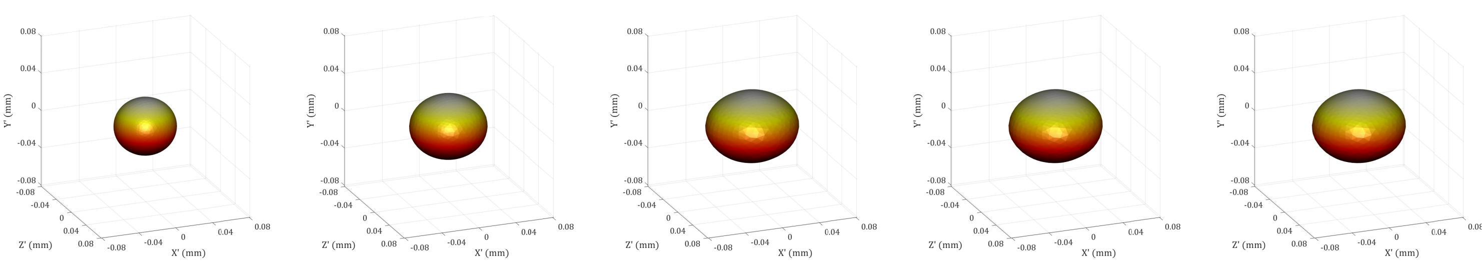

(a) (b) (c) (d) (e)

Figure 16: Finite element calculations for an imposed loading velocity $V = 250$ m/s, initial void volume fraction in the notched region $f^0 = 2\%$ and initial diameter of the voids $\phi = 50$ μm. Results obtained from simulation with actual pores and material modeled with von Mises plasticity. 3D reconstructions of the surfaces of void 2 indicated in Fig. 14(a) for different imposed displacement values: (a) $U_Y = 0.05$ mm, (b) $U_Y = 0.1$ mm, (c) $U_Y = 0.2$ mm, (d) $U_Y = 0.3$ mm and (e) $U_Y = 0.35$ mm. The origin of the Cartesian coordinate system (X', Y', Z') is located at the center of the void, with X', Y' and Z' being parallel to the X, Y and Z axes, respectively.

0.25, 0.375 and 0.5 mm, respectively. All voids grow uniformly, showing similar levels of plastic strain across all imposed displacement values. This contrasts with the findings presented in the contour plots 11(a), ..., (d) for 100 m/s, where the distribution of void sizes and plastic strains varies significantly starting from an imposed displacement of 0.1 mm. The uniform growth of pores at 1000 m/s is due to inertia, which slows down void expansion and homogenizes the distribution of plastic deformations. The comparison of subplots 11(a), ..., (d), 14(a), ..., (e) and 17(a), ..., (e) reveals that, for any given imposed displacement, there are (some) larger voids in the simulations conducted with an applied velocity of 100 m/s and 250 m/s. Figs. 18 and 19 present 3D reconstructions of the surfaces of voids 1 and 2, respectively, as indicated in Fig. 17(a). Note that these are the same pores analyzed in Figs. 12-13 and 15-16 for the lower imposed velocities of 100 m/s and 250 m/s. The shape and size of the two voids evolve similarly, with both adopting an ellipsoidal form compressed along the loading direction. Void coalescence appears to result from direct impingement rather than ligament necking (Jacques et al., 2012c), as the voids do not exhibit the flat faces characteristic of plastic localization in the intervoid ligament, as observed at lower loading velocities, see Figs. 12-13 and 15-16. The evolution of the ratios $\frac{b}{a}$ and $\frac{c}{a}$ with the imposed displacement, as shown in Figs. 20(a) and 20(b), is quantitatively the same for voids 1 and 2. These results contrast with the size and shape evolution of these two voids at a lower velocities of 100 m/s and 250 m/s (see Figs. 12-13, and Figs. 15-16), where pore 1 grew much faster and eventually developed a prism-like shape, while pore 2 remained slightly ellipsoidal and was ultimately unloaded.

Subplots (a'), ..., (e') show contour plots for a calculation with homogenized porosity and microinertia effects. The results correspond to the same imposed displacements considered for the calculation with discrete pores. Plastic deformation uniformly increases along the notch section of the specimen under loading. No plastic localization occurs for the displacements investigated. Compared to the calculations at lower loading velocities of 100 m/s and 250 m/s shown in 11(a') ..., (d') and 14(a') ..., (e'), increasing the loading rate enhances the effect of microinertia, stabilizing plastic flow and preventing localization, thereby distributing plastic deformation more uniformly. The maximum plastic deformation in the notch for $U_Y = 0.5$ mm is slightly smaller than 0.4. Moreover, the stress triaxiality in the notch for an imposed displacement of 0.5 mm reaches a value of 16. The comparison of the results obtained using the dynamic homogenization approach by Molinari and Mercier (2001) for loading rates of 100, 250, 500 m/s and 1000 m/s in the contour plots of Figs. 11, 14, 4 and 17 clearly illustrates the transition from spurious localization confined to a single layer of elements to diffuse plastic straining within the notch, attributed to the stabilizing effect of microinertia on plastic localization.

Subplots (a"), ..., (e") include contour plots for a calculation with homogenized porosity without microinertia effects. The formation of a thin band with large strains is noticeable for an imposed displacement of 0.25 mm. This band consists of only a single layer of elements, highlighting that neglecting microinertia results in spurious plastic localization across all investigated loading rates (increasing the loading rate enhances macroinertia effects, but this alone is insufficient to regularize plastic localization for the problem addressed in this paper). At a displacement of 0.375 mm, the maximum deformation within the band reaches 1.18, whereas in adjacent elements of the mesh, it drops to 0.31. As displacement increases to 0.5 mm, the difference in plastic strain between the inside and outside of the band widens. The maximum deformation inside the band rises to 1.55, while outside the band, the plastic strain has (only) increased to 0.38.

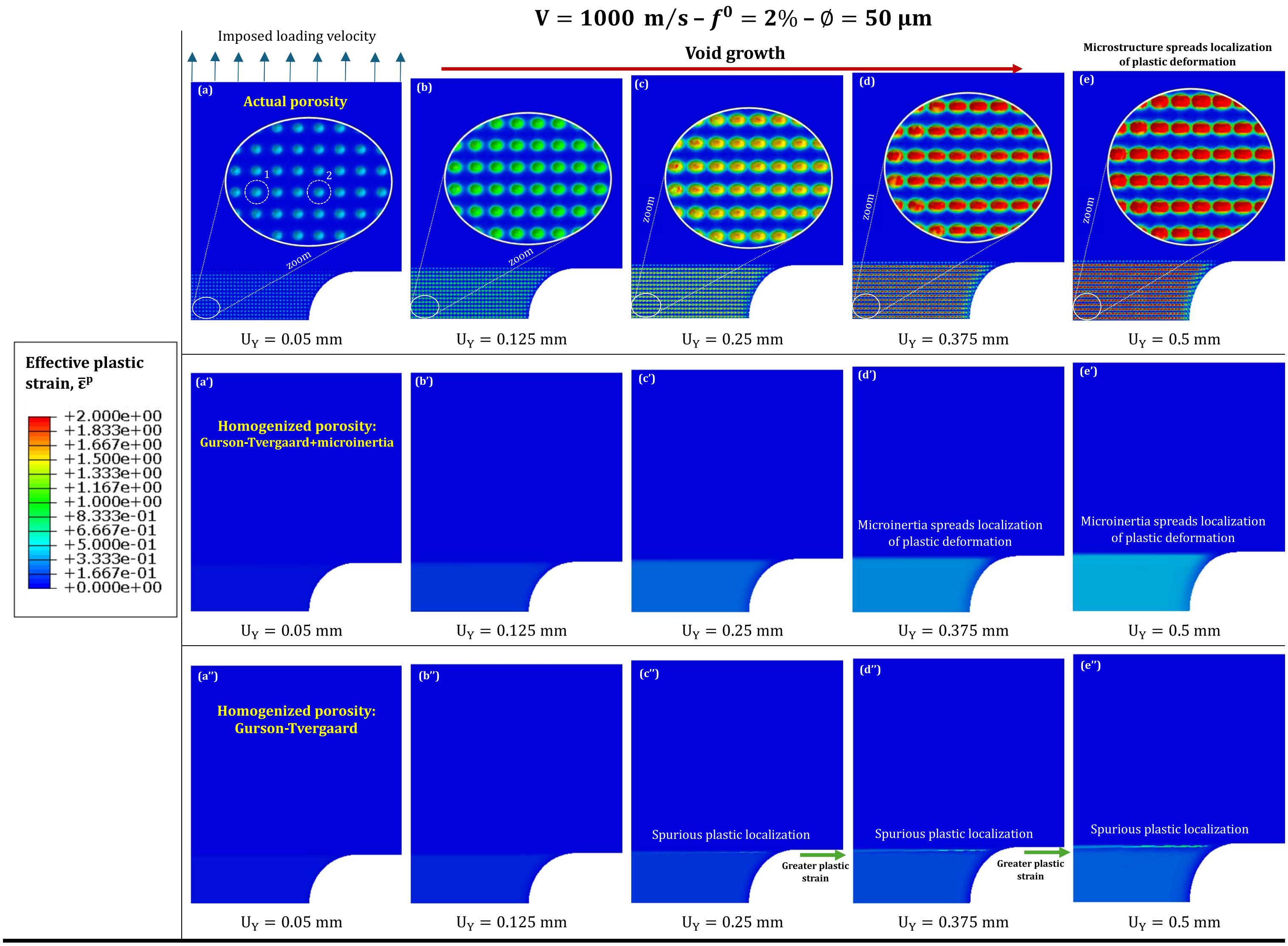

Figure 17: Contours of effective plastic strain $\bar{\varepsilon}^p$ for different imposed displacement values: (a)-(a')-(a") $U_Y = 0.05$ mm, (b)-(b')-(b") $U_Y = 0.125$ mm, (c)-(c')-(c") $U_Y = 0.25$ mm, (d)-(d')-(d") $U_Y = 0.375$ mm and (e)-(e')-(e") $U_Y = 0.5$ mm. Cross-section view at $Z = -0.074$ mm. The imposed loading velocity is $V = 1000$ m/s, the initial void volume fraction in the notched region is $f^0 = 2\%$ and the initial diameter of the voids is $\phi = 50$ μm. Subplots (a), ..., (e) correspond to calculation with actual pores and material modeled with von Mises plasticity. Subplots (a'), ..., (e') correspond to calculation with homogenized porosity and material modeled with Gurson-Tvergaard plasticity and microinertia effects. Subplots (a"), ..., (e") correspond to calculation with homogenized porosity and material modeled with Gurson-Tvergaard plasticity and without microinertia effects. For interpretation of the references to color in this figure legend, the reader is referred to the web version of this article.

Figure 21 shows the evolution of the global normalized void volume fraction in the notch f^{notch}/f^0 with the imposed axial displacement U_Y for calculations performed with discrete pores (red lines), homogenized porosity and microinertia effects (green lines), and homogenized porosity without microinertia effects (orange lines). Comparison of data from simulations carried out with imposed loading velocities of 100 m/s (solid lines) and 1000 m/s (dashed lines). The results correspond to the calculations shown in Figs. 11 and 17. The global porosity increases more rapidly with higher applied velocities due to inertia effects, which distribute plastic deformation within the notch and promote porosity growth

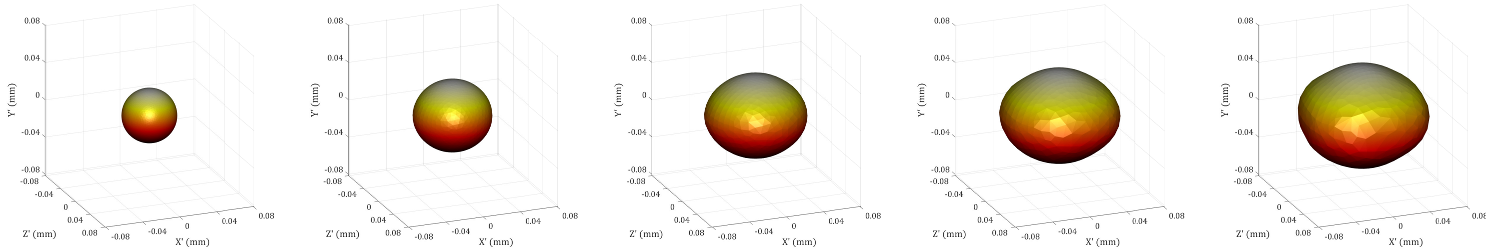

(a) (b) (c) (d) (e)

Figure 18: Finite element calculations for an imposed loading velocity $V = 1000$ m/s, initial void volume fraction in the notched region $f^0 = 2\%$ and initial diameter of the voids $\phi = 50$ μm. Results obtained from simulation with actual pores and material modeled with von Mises plasticity. 3D reconstructions of the surfaces of void 1 indicated in Fig. 17(a) for different imposed displacement values: (a) $U_Y = 0.05$ mm, (b) $U_Y = 0.125$ mm, (c) $U_Y = 0.25$ mm, (d) $U_Y = 0.375$ mm and (e) $U_Y = 0.5$ mm. The origin of the Cartesian coordinate system (X', Y', Z') is located at the center of the void, with X', Y' and Z' being parallel to the X, Y and Z axes, respectively.

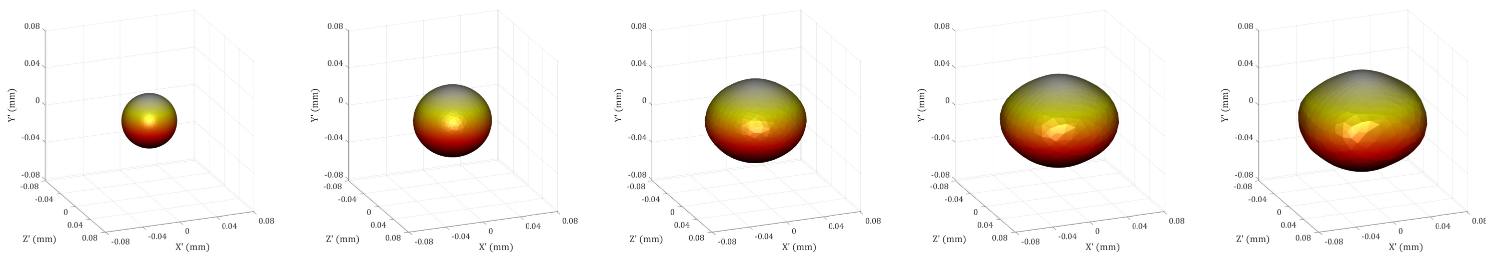

(a) (b) (c) (d) (e)

Figure 19: Finite element calculations for an imposed loading velocity $V = 1000$ m/s, initial void volume fraction in the notched region $f^0 = 2\%$ and initial diameter of the voids $\phi = 50$ μm. Results obtained from simulation with actual pores and material modeled with von Mises plasticity. 3D reconstructions of the surfaces of void 2 indicated in Fig. 17(a) for different imposed displacement values: (a) $U_Y = 0.05$ mm, (b) $U_Y = 0.125$ mm, (c) $U_Y = 0.25$ mm, (d) $U_Y = 0.375$ mm and (e) $U_Y = 0.5$ mm. The origin of the Cartesian coordinate system (X', Y', Z') is located at the center of the void, with X', Y' and Z' being parallel to the X, Y and Z axes, respectively.

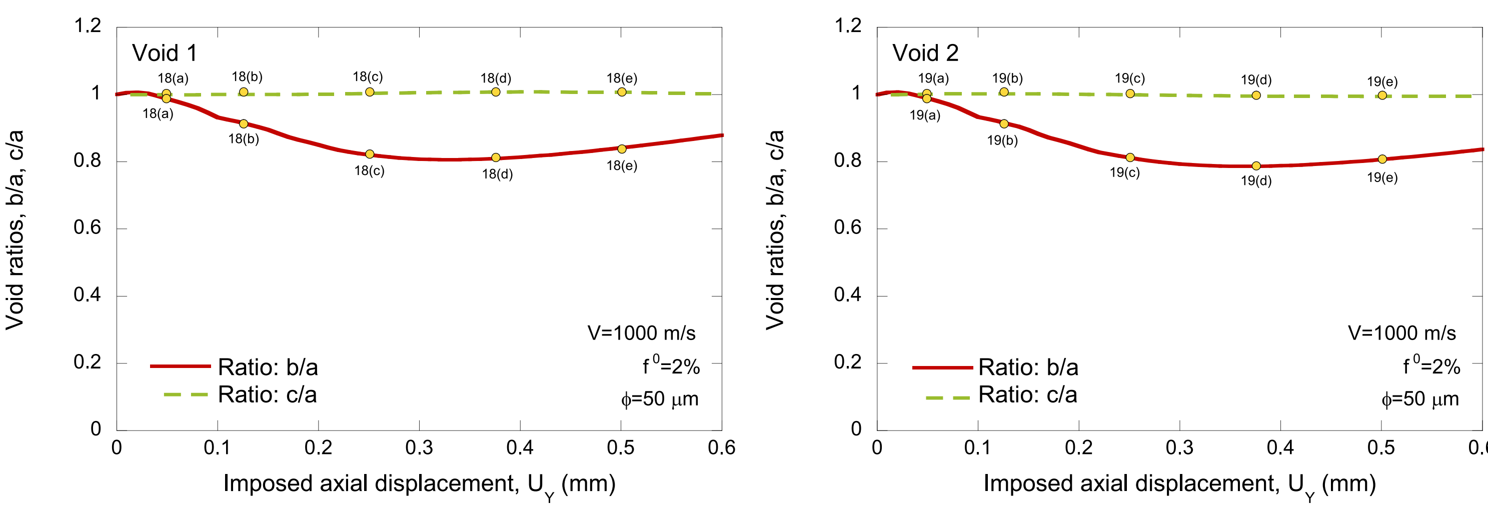

(a) (b)

Figure 20: Finite element calculations for an imposed loading velocity $V = 1000$ m/s, initial void volume fraction in the notched region $f^0 = 2\%$ and initial diameter of the voids $\phi = 50$ μm. Results obtained from simulation with actual pores and material modeled with von Mises plasticity. Evolution of the void ratios, $\frac{b}{a}$ and $\frac{c}{a}$, with the imposed displacement U_Y. (a) Void 1 indicated in Fig. 17(a). (b) Void 2 indicated in Fig. 17(a). The yellow markers represent the imposed displacement values used in the 3D reconstructions of the pores shown in Figs. 18 and 19.

throughout the entire region. Similarly, the porosity in the notch increases more rapidly in simulations with discrete voids compared to those with homogenized porosity across all considered loading velocities (see also Fig. 9(b)). This is due to the regularization effect of the explicit representation of the porous microstructure, which promotes the development of more uniform plastic deformation fields (at the macroscale) and facilitates the growth of (all) pores. Moreover, at a loading velocity of 1000 m/s, the porosity in the notch grows slightly faster for the simulation with microinertia (at large strains) compared to the calculation with the quasi-static Gurson-Tvergaard model, similar to the results obtained for 500 m/s in Fig. 9(b). Microinertia effects spread plastic deformation within the notch and promote the growth of more voids (in the same way that discrete pores do). In contrast, at 100 m/s, the trend is the opposite, and the simulation with the quasi-static Gurson-Tvergaard model predicts faster global porosity growth. For low velocities, microinertia effects are small, and plastic localization is confined within a single localization band that grows more rapidly in the case of the quasi-static Gurson-Tvergaard model, promoting faster porosity growth (see Fig. 11).

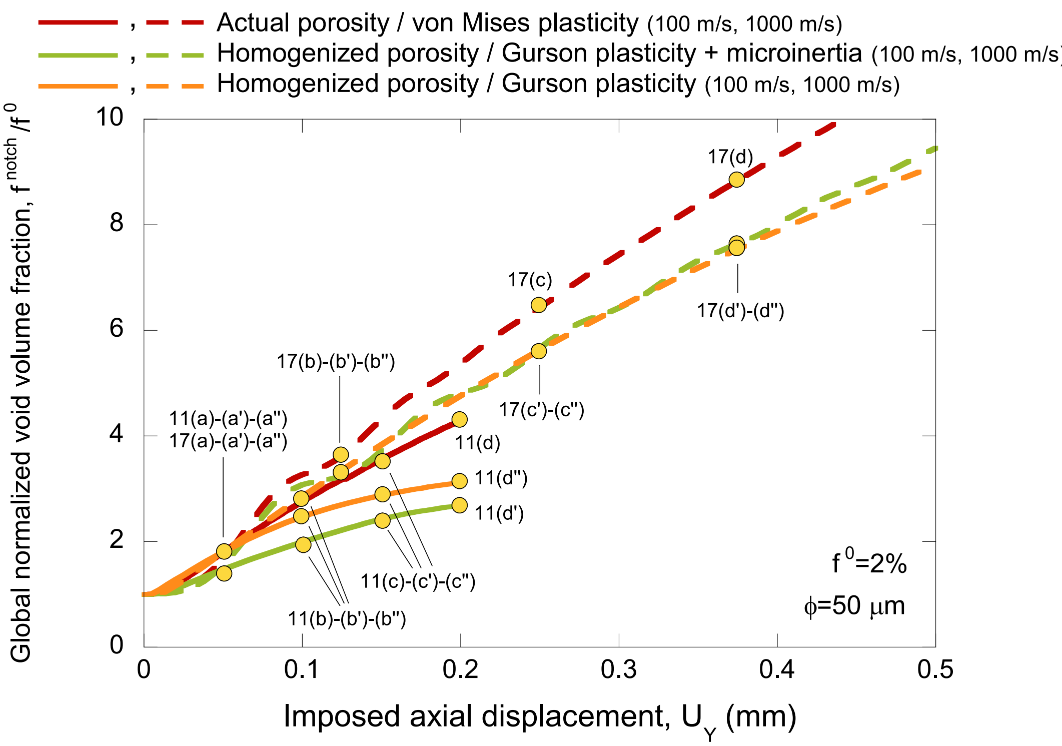

Figure 21: Comparison of results obtained with actual pores and material modeled with von Mises plasticity (red lines), homogenized porosity and material modeled with Gurson-Tvergaard plasticity and microinertia effects (green lines), and homogenized porosity and material modeled with Gurson-Tvergaard plasticity and without microinertia effects (orange lines). The initial void volume fraction in the notched region is $f^0 = 2\%$ and the initial diameter of the voids is $\phi = 50$ μm. Global normalized void volume fraction in the notch f^{notch}/f^0 versus imposed axial displacement U_Y. Results corresponding to imposed loading velocities of 100 m/s (solid lines) and 1000 m/s (dashed lines). The yellow markers represent the imposed displacement values used in the contour plots of Figs. 11 and 17. For interpretation of the references to color in this figure legend, the reader is referred to the web version of this article.

Figure 22 shows the local normalized void volume fraction $f^{local}_{A,B}/f^0$, as a function of the imposed axial displacement, U_Y, for calculations performed with loading velocity of 100 m/s. Recall from Section 4.1 that for the simulations with discrete voids, $f^{local}_{A,B}$ is measured within an individual unit cell of the notched region. In contrast, for the simulations employing homogenized porosity, $f_{A,B}^{local}$ is computed within a single finite element.

The data in Fig. 22(a) correspond to a unit cell located outside (just below) the void layer with the fastest growth, as indicated in Fig. 11(d), and to a finite element outside (just below) the plastic localization band shown in Figs. 11(d') and 11(d"). The measurements in the calculations with discrete voids and with homogenized porosity were taken at similar location. At the onset of loading, the local void volume fraction increases nearly linearly with the imposed axial displacement, and for displacements below 0.075, the value of f_{A}^{local} is very similar for the calculation with discrete voids and the simulations with homogenized porosity. However, the value of f_{A}^{local} eventually ceases to increase in all three calculations. Saturation of the local normalized void volume fraction occurs earlier in the simulation with discrete voids, reaching a value of 2.4, followed by the calculation with the standard (quasi-static) Gurson-Tvergaard model at 2.9, and by the Gurson-Tvergaard model with microinertia effects at 5.35. Note that the specific values of saturation porosity are (highly) dependent on the unit cell and finite element used for measurement, due to the heterogeneous distribution of porosity in the notch resulting from reduced inertia effects. However, irrespective of the selected unit cell and finite element, we observed that the saturation of local porosity outside the localization band occurs for a lower displacement than in the case of 500 m/s (shown in Fig. 10(a)), as reduced inertia effects lead to earlier plastic localization.

The data in Fig. 22(b) pertain to a unit cell situated inside the void layer with the fastest growth in Fig. 11(d), and to a finite element inside the plastic localization band depicted in Figs. 11(d') and 11(d"). The void volume fraction increases monotonically in all three calculations across the entire range of imposed displacements. Initially, the growth is faster in the simulation with discrete voids compared to the calculations with homogenized porosity. However, the $f_{B}^{local}/f^{0} - U_{Y}$ curves intersect at intermediate displacement values, and subsequently, the porosity within the localization band increases more rapidly in the case of the standard (quasi-static) Gurson-Tvergaard model. Neglecting microstructural inertia effects leads to more rapid localization across all loading velocities considered (Fig. 10(b) indicates that at 500 m/s, the porosity within the localization band also increases more rapidly in the Gurson-Tvergaard model without microinertia effects). Nevertheless, it is important to note that at 100 m/s, the differences in the porosity growth within the band between the calculations with and without microstructural inertia effects are smaller than at 500 m/s.

Figure 23 shows the local normalized void volume fraction $f_{A,B}^{local}/f^{0}$, as a function of the imposed axial displacement, U_{Y}, for calculations performed with loading velocity of 1000 m/s. The difference compared to the results presented in Fig. 22 is that the loading velocity is an order of magnitude greater.

The data in Fig. 23(a) are taken adjacent (outside) to the plastic localization band depicted in Fig. 17(e"). The measurements in the calculations involving discrete voids and homogenized porosity were obtained from similar locations. The void volume fraction f_{A}^{local} for the calculations conducted with discrete pores and with the Gurson-Tvergaard model which includes microinertia effects, exhibits a quasi-linear increase with the imposed displacement, reflecting sustained loading that does not result in plastic localization, see Figs. 17(e) and 17(e'). On the other hand, the simulation with the quasi-static Gurson-Tvergaard model predicts saturation of the porosity at a displacement of 0.3 due to the formation

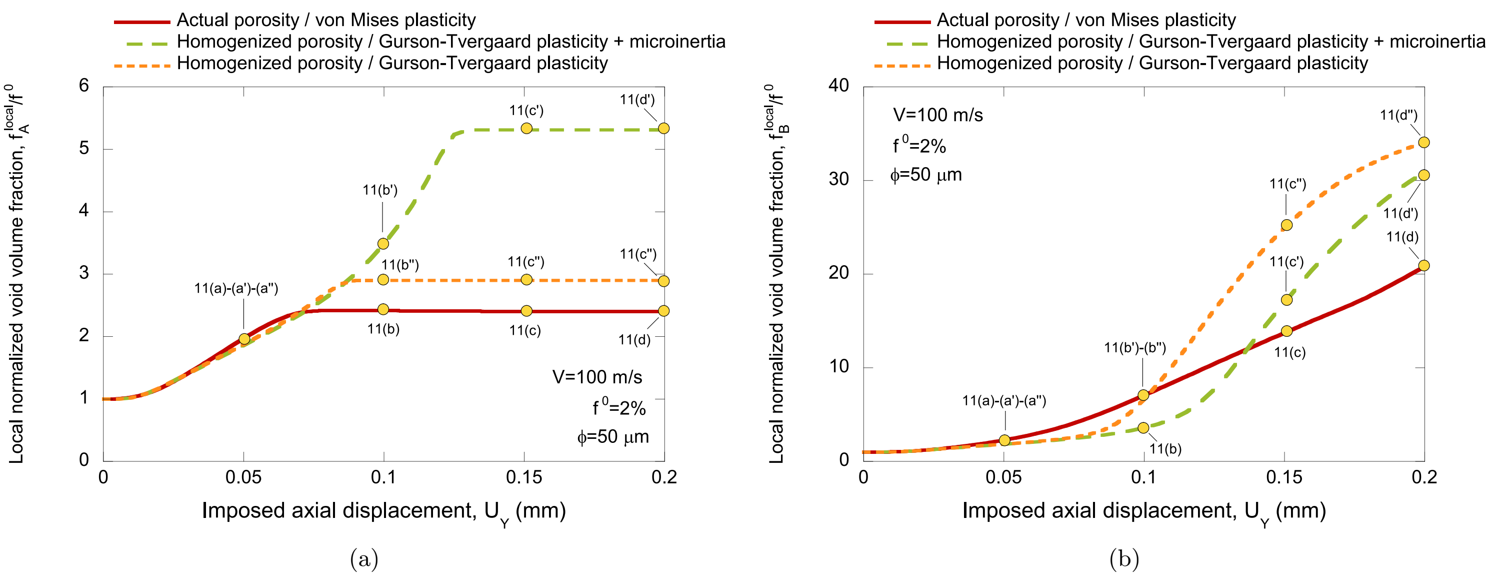

Figure 22: Finite element calculations for an imposed loading velocity $V = 100$ m/s, initial void volume fraction in the notched region $f^0 = 2\%$ and initial diameter of the voids $\phi = 50$ μm. Local normalized void volume fraction $f^{local}_{A,B}/f^0$ versus imposed axial displacement U_Y. The subscripts A and B correspond to measurements taken outside and inside the plastic localization band that forms within the notch. Comparison of results obtained with actual pores and material modeled with von Mises plasticity (red solid line), homogenized porosity and material modeled with Gurson-Tvergaard plasticity and microinertia effects (green dashed line) and homogenized porosity and material modeled with Gurson-Tvergaard plasticity and without microinertia effects (orange dotted line). (a) The center of the unit cell in the calculation with discrete voids is located at coordinates $X = 0.817$ mm, $Y = 0.668$ mm, and $Z = -0.074$ mm, while the finite element selected in the calculations with homogenized porosity is at coordinates $X = 0.956$ mm, $Y = 1.011$ mm, and $Z = -0.074$ mm. (b) The center of the unit cell in the calculation with discrete voids is located at coordinates $X = 0.817$ mm, $Y = 0.817$ mm, and $Z = -0.074$ mm, while the finite element selected in the calculations with homogenized porosity is at coordinates $X = 0.963$ mm, $Y = 1.051$ mm, and $Z = -0.074$ mm. The yellow markers represent the imposed displacement values used in the contour plots shown in Fig. 11. For interpretation of the references to color in this figure legend, the reader is referred to the web version of this article.

of a plastic localization band, see Fig. 17(e").

The data in Fig. 23(b) are taken inside the plastic localization band depicted in Fig. 17(e"). The measurements in the simulations involving discrete voids and homogenized porosity were obtained from similar locations. In the calculations utilizing discrete pores and the Gurson-Tvergaard model with microinertia effects, the void volume fraction f_B^{local} demonstrates a quasi-linear increase with the imposed displacement, which indicates sustained loading that does not induce plastic localization, see Figs. 17(e) and 17(e') —the results are *virtually* quantitatively the same as those presented in 23(a) due to the homogeneous distribution of plastic strains within the notch. However, the calculation performed with the Gurson-Tvergaard model, excluding microinertia effects, predicts a significantly faster increase in porosity, characterized by a nonlinear concave-upward shape that indicates plastic localization, see Fig. 17(e"). At 1000 m/s, the differences in the porosity growth within the band between the calculations with and without microstructural inertia effects are larger compared to the calculations carried out for 100 m/s and 500 m/s —compare subplots 10(b), 22(b) and 23(b).

The results presented in Figs. 21, 22, and 23 indicate that, although the global porosity in the notch may be higher in the calculations involving discrete voids and homogenized porosity with microinertia effects, the local porosity within the localization band is greater in the calculations using the quasi-static Gurson-Tvergaard model across the entire range of loading velocities considered because neglecting microstructural inertia leads to faster plastic localization.

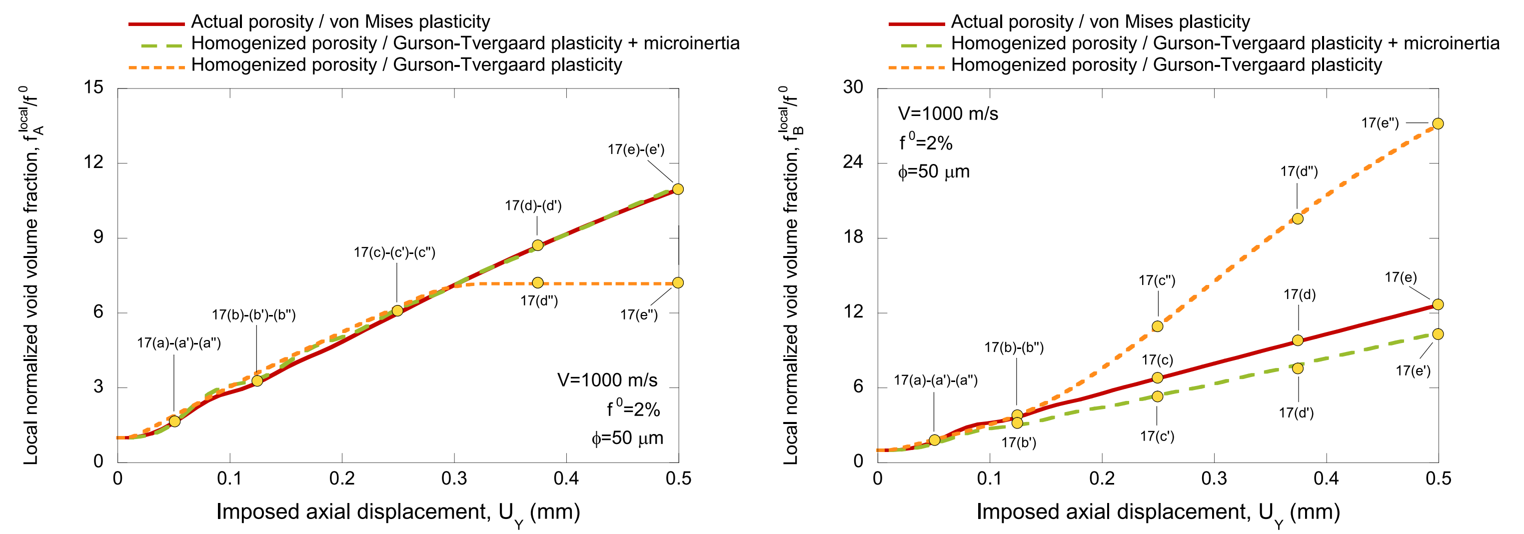

(a) (b)

Figure 23: Finite element calculations for an imposed loading velocity $V = 1000$ m/s, initial void volume fraction in the notched region $f^0 = 2\%$ and initial diameter of the voids $\phi = 50$ μm. Local normalized void volume fraction $f_{A,B}^{local}/f^0$ versus imposed axial displacement U_Y. The subscripts A and B correspond to measurements taken outside and inside the plastic localization band that forms within the notch. Comparison of results obtained with actual pores and material modeled with von Mises plasticity (red solid line), homogenized porosity and material modeled with Gurson-Tvergaard plasticity and microinertia effects (green dashed line) and homogenized porosity and material modeled with Gurson-Tvergaard plasticity and without microinertia effects (orange dotted line). (a) The center of the unit cell in the calculation with discrete voids is located at coordinates $X = 1.114$ mm, $Y = 1.856$ mm, and $Z = -0.074$ mm, while the finite element selected in the calculations with homogenized porosity is at coordinates $X = 1.096$ mm, $Y = 1.7980$ mm, and $Z = -0.074$ mm. (b) The center of the unit cell in the calculation with discrete voids is located at coordinates $X = 1.114$ mm, $Y = 1.708$ mm, and $Z = -0.074$ mm, while the finite element selected in the calculations with homogenized porosity is at coordinates $X = 1.126$ mm, $Y = 1.900$ mm, and $Z = -0.074$ mm. The yellow markers represent the imposed displacement values used in the contour plots shown in Fig. 17. For interpretation of the references to color in this figure legend, the reader is referred to the web version of this article.

4.3. The effect of void size

Figure 24 includes contours of effective plastic strain corresponding to simulations with discrete pores, homogenized porosity including microinertia effects, and homogenized porosity without microinertia effects. The difference compared to Fig. 17 is that the void diameter has been reduced to 30 μm while maintaining the same void volume fraction of 2%.

Subplots 24(a), ..., (e) correspond to a calculation involving actual pores. The imposed displacements are 0.125, 0.25, 0.5, 0.75 and 0.9 mm, respectively. For $U_Y = 0.125$ mm, all the voids have virtually the same size and plastic strain. However, increasing the imposed displacement to 0.25 mm leads to noticeable heterogeneity in the plastic strain field, causing varying growth rates among different voids. This results in a distribution of void sizes that becomes evident at a displacement of 0.5 mm. There are small ellipsoidal pores elongated perpendicular to the loading direction that remain unloaded (see white arrow), while larger spherical voids are nearing coalescence (see yellow arrow). For displacements of 0.75 and 0.9 mm, the larger pores have started to grow parallel to the loading direction due to coalescence of adjacent voids located at planes Y = constant (the intervoid ligament cannot longer stretch along the X and Z directions). Figs. 25 and 26 include 3D reconstructions of the surfaces of voids 1 and 2, respectively, as indicated in subplot 24(a). Void 1 expands and deforms into an ellipsoidal shape at a displacement of 0.5 mm, and upon further displacement, it unloads while preserving the same shape and size. In contrast, void 2 grows continuously throughout the loading process, transitioning from an initial spherical shape to an ellipsoidal shape, and eventually adopting a prismatic form due to coalescence with adjacent voids. Notice that the simulation corresponding to larger pores of $\phi = 50$ μm shown in Fig. 17 displayed a more uniform distribution of void sizes (e.g., compare 17(e) and 24(c)). This is attributed to the inertial resistance to grow of the porous microstructure, which increases with pore size. Increasing/decreasing the voids size results in a more/less consistent growth rate among all voids within the microstructure and thereby producing a more/less uniform plastic deformation field.

Subplots 24(a'), ..., (e') correspond to a calculation using the Gurson-Tvergaard model, including microinertia effects. The deformation field becomes noticeable in the specimen under an imposed displacement of 0.25 mm, showing the development of a localization band (enclosed within a dashed green box) accompanied by lower plastic strains in the notched section. At a displacement of 0.5 mm, the maximum plastic strain in the band is 0.47, while in the adjacent elements it is 0.38. The maximum stress triaxiality inside the band for this value of the imposed displacement reaches a value of 30. The deformation band spans several grid elements and the distribution of plastic strains within the band exhibits smooth profile due to the regularization effect of microinertia which stabilizes plastic flow. Nevertheless, the contrast between the deformation in the band and the deformation outside it is greater than in the simulation performed with the same applied velocity and greater voids of 50 μm (compare 17(e') and 24(c')). Decreasing the pore size diminishes the effect of microinertia —see equation (6)— and facilitates localization, consistent with the results shown in subplots 17(a), ..., (e) and subplots 24(a), ..., (e) for simulations with discrete pores. For instance, the maximum value of plastic deformation inside the band reaches 0.71 and 0.84 for imposed displacements of 0.75 mm and 0.9 mm, respectively, while in the adjacent elements the strain is significantly lower 0.51 and 0.55. The continuous increase in the difference in plastic deformation inside and outside the band illustrates the progressive localization of deformation favored by the small pores size.

Subplots 24(a”), ..., (e”) correspond to a calculation using homogenized porosity excluding microinertia effects. Recall that the Gurson-Tvergaard model does not account for the effect of void size on the constitutive behavior of the material, as porosity is represented by a single scalar variable. Thus, the results in subplots 17(a”), ..., (e”) and 24(a”), ..., (e”) are virtually the same. The difference is that in 24(a”), ..., (e”) the specimen thickness has been reduced 60% to match the sample dimensions used in the calculations performed with discrete voids and homogenized porosity accounting for microinertia effects. Plastic deformations concentrate early in the deformation process within a single layer of elements, which soon become heavily distorted, highlighting the mesh dependency of the localization process.

Figure 27 displays contours of effective plastic strain for simulations with discrete pores, homogenized porosity including microinertia effects, and homogenized porosity excluding microinertia effects. Compared to Fig. 24, the diameter of the voids has been increased fivefold to 150 μm, while maintaining the same void volume fraction of 2%.

Subplots 27(a), ..., (e) correspond to a calculation involving actual pores, with imposed displacements matching those in 24(a), ..., (e) to facilitate comparison between the two simulations differing solely in the size of the voids. Compared to Fig. 24, as the pores are larger, there are fewer pores, and the intervoid ligament is initially greater. Increasing the initial diameter of the voids enhances the inertial resistance of the porous microstructure. This results in the plastic deformation extending uniformly along the notch, causing all the pores to deform and grow similarly (notice the contrast with the heterogeneous growth of pores depicted in 24(a), ..., (e), where the initial diameter of the voids was five times smaller). For example, Figs. 28 and 29 show 3D reconstructions of the surfaces of voids 1 and 2, respectively, which are enclosed within a dashed white circle in Fig. 27(a). The shape and size of both pores remain very similar across all imposed displacement values. The pores initially elongate into an ellipsoidal shape in the direction of the load and eventually develop a rhombohedral form, characterized by flattened faces resulting from the coalescence of pores situated in planes where $Y =$ constant. Figs. 30(a) and 30(b) show the evolution of the ratios $\frac{b}{a}$ and $\frac{c}{a}$ with imposed displacement for voids 1 and 2, respectively. The results for the two pores are almost the same. The ratio $\frac{b}{a}$ monotonically increases with the loading, showing that the pores elongate parallel to the loading direction, and the ratio $\frac{c}{a}$ is nearly 1, showing that the grow of the voids along the X' and Z' directions is the same. These results contrast with the calculations performed for smaller voids (see Figs. 7 and 20) where the pores elongated along the X' direction at the beginning of loading, and only showed an increase along Y' relative to X' if coalescence occurred. These findings highlight that the size of the voids and the distance between them significantly affect the evolution of the shape of the voids during loading.

Subplots 27(a’), ..., (e’) correspond to a calculation performed with the Gurson-Tvergaard model accounting for microinertia effects. Plastic deformation extends uniformly across the entire notch section due to the increased inertia of the microstructure with large pores. In contrast to the results obtained for a pore diameter of 30 μm shown in subplots 24(a’), ..., (e’), no localization band formation is observed. The maximum plastic deformation in the notch for imposed

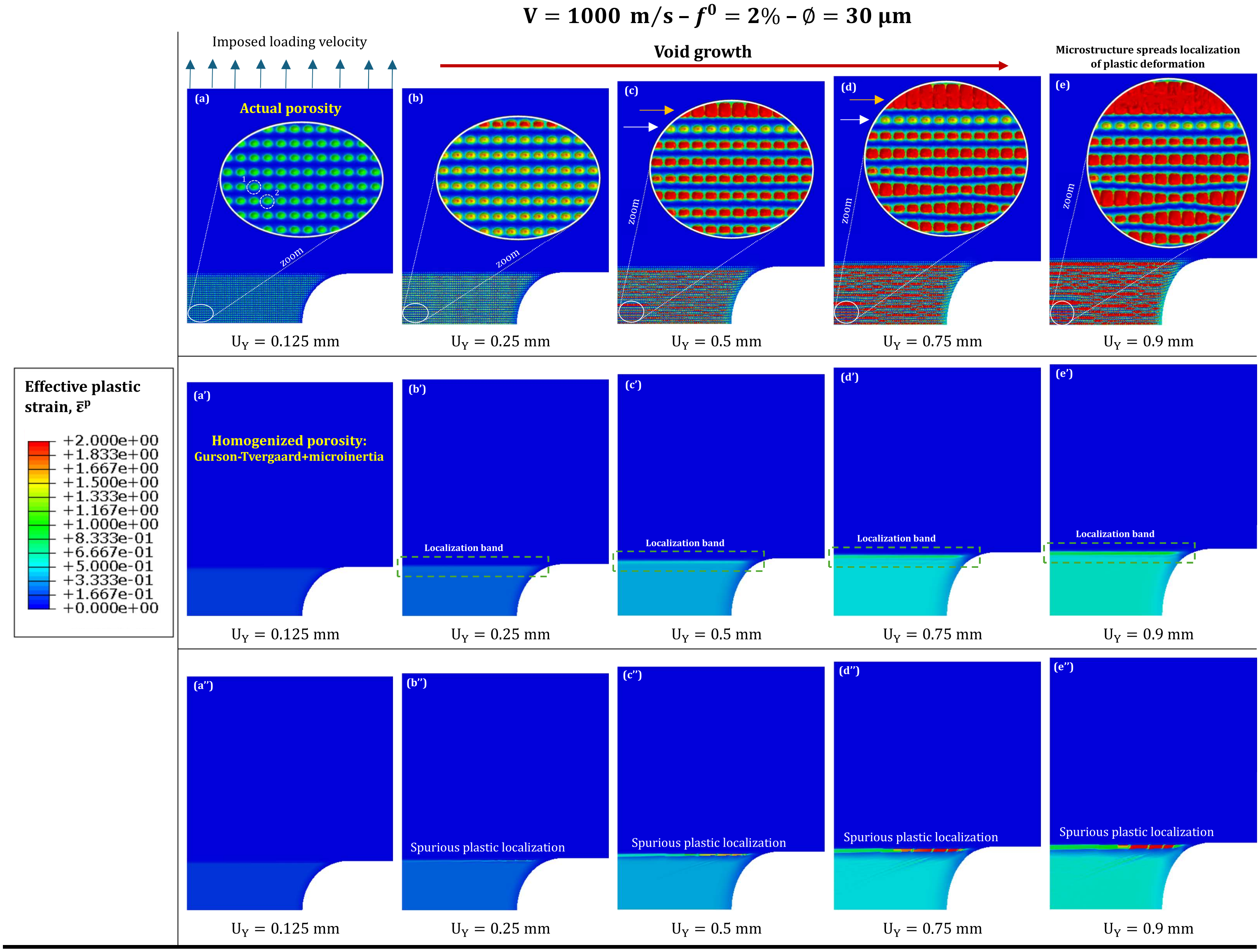

Figure 24: Contours of effective plastic strain $\bar{\varepsilon}^p$ for different imposed displacement values: (a)-(a')-(a") $U_Y = 0.125$ mm, (b)-(b')-(b") $U_Y = 0.25$ mm, (c)-(c')-(c") $U_Y = 0.5$ mm, (d)-(d') $U_Y = 0.75$ mm and (e)-(e') $U_Y = 1$ mm. Cross-section view at $Z = -0.044$ mm. The imposed loading velocity is $V = 1000$ m/s, the initial void volume fraction in the notched region is $f^0 = 2\%$ and the initial diameter of the voids is $\phi = 30$ μm. Subplots (a), ..., (e) correspond to calculation with actual pores and material modeled with von Mises plasticity. Subplots (a'), ..., (e') correspond to calculation with homogenized porosity and material modeled with Gurson-Tvergaard plasticity and microinertia effects. Subplots (a"), ..., (e") correspond to calculation with homogenized porosity and material modeled with Gurson plasticity and without microinertia effects. For interpretation of the references to color in this figure legend, the reader is referred to the web version of this article.

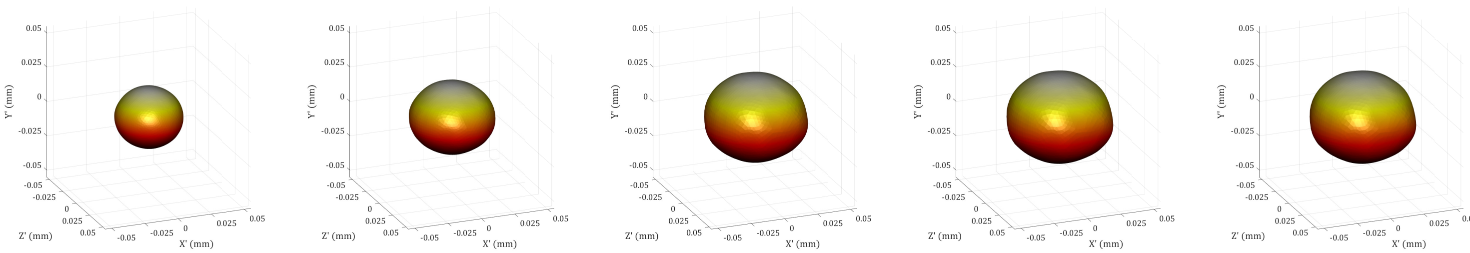

(a) (b) (c) (d) (e)

Figure 25: Finite element calculations for an imposed loading velocity $V = 1000$ m/s, initial void volume fraction in the notched region $f^0 = 2\%$ and initial diameter of the voids $\phi = 30$ μm. Results obtained from simulation with actual pores and material modeled with von Mises plasticity. 3D reconstructions of the surfaces of void 1 indicated in Fig. 24(a) for different imposed displacement values: (a) $U_Y = 0.125$ mm, (b) $U_Y = 0.25$ mm, (c) $U_Y = 0.5$ mm, (d) $U_Y = 0.75$ mm and (e) $U_Y = 0.9$ mm. The origin of the Cartesian coordinate system (X', Y', Z') is located at the center of the void, with X', Y' and Z' being parallel to the X, Y and Z axes, respectively.

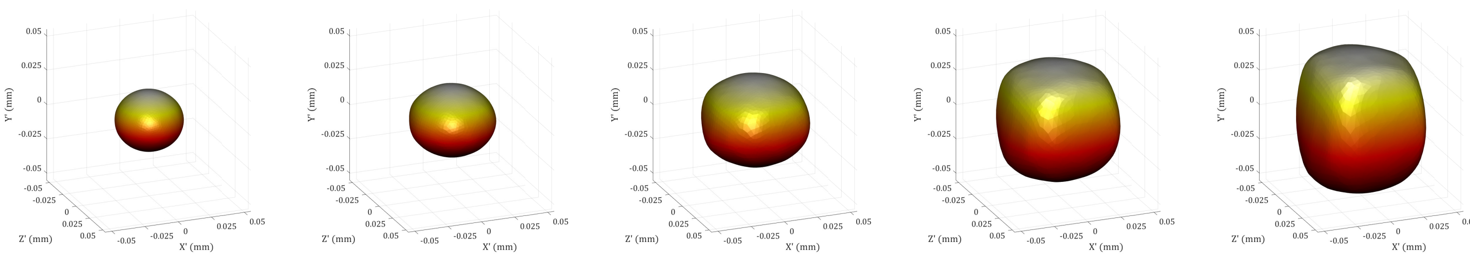

(a) (b) (c) (d) (e)

Figure 26: Finite element calculations for an imposed loading velocity $V = 1000$ m/s, initial void volume fraction in the notched region $f^0 = 2\%$ and initial diameter of the voids $\phi = 30$ μm. Results obtained from simulation with actual pores and material modeled with von Mises plasticity. 3D reconstructions of the surfaces of void 2 indicated in Fig. 24(a) for different imposed displacement values: (a) $U_Y = 0.125$ mm, (b) $U_Y = 0.25$ mm, (c) $U_Y = 0.5$ mm, (d) $U_Y = 0.75$ mm and (e) $U_Y = 0.9$ mm. The origin of the Cartesian coordinate system (X', Y', Z') is located at the center of the void, with X', Y' and Z' being parallel to the X, Y and Z axes, respectively.

displacements of 0.5 mm, 0.75 mm, and 0.9 mm is 0.43, 0.56, and 0.63, respectively. In all cases, these values are lower than those recorded for the simulation with 30 μm voids. Moreover, the maximum stress triaxiality within the notch for the same three values of the imposed displacement is 12, 7 and 5, respectively. Notice that incorporating microinertia into the Gurson-Tvergaard model captures the effect of pore size on the development of uniform deformation fields, consistent with the observations derived from calculations with discrete voids. The differences between the calculations with actual pores and those with homogeneous porosity and microinertia are mostly quantitative rather than qualitative. Specifically, modeling discrete pores results in higher maximum plastic strain values due to strain concentrations from void shapes, as calculations with actual voids and with homogenized porosity reflect different spatial scales of the material.

Subplots 27(a"), ..., (e") correspond to a calculation using homogenized porosity which does not include microinertia effects. The only difference from the calculation reported in 24(a"), ..., (c") is that the specimen thickness is increased by a factor of five to match the sample dimensions used in the simulations performed with discrete voids and homogenized porosity accounting for microinertia effects. The plastic strain fields are nearly identical in 24(a"), ..., (e") and 27(a"), ..., (e"). The analysis of results is the same for the two calculations (refer to the discussion of 24(a"), ..., (e") for detailed information).

Figure 31 shows the evolution of the global normalized void volume fraction in the notch f^{notch}/f^0 with the imposed axial displacement U_Y for calculations performed with discrete pores (red lines), homogenized porosity and microinertia effects (green lines), and homogenized porosity without microinertia effects (orange lines). Subplots 31(a) and 31(b) display the results obtained for initial void diameters of 30 μm and 150 μm, respectively, based on the calculations shown in Figs. 24 and 27. The results for both initial void sizes are very similar: the void diameter has little impact, both qualitatively and quantitatively, on the global porosity measurement within the notch (however, the void size has a greater impact on the local porosity within the plastic localization band, as discussed in the following paragraphs). The value of f^{notch}/f^0 increases more rapidly in simulations with discrete voids compared to those with homogenized porosity and microinertia effects, while the lowest rate of porosity growth is predicted by calculations using the quasi-static Gurson-Tvergaard model. Note the oscillations in porosity evolution in calculations for $\phi = 150$ μm, observed in both the actual porosity model and the homogenized porosity model incorporating microinertia, which reflect the impact of microinertia on void evolution dynamics.

Figure 32 presents the evolution of the local normalized void volume fraction, $f^{local}_{A,B}/f^0$, as a function of the imposed axial displacement, U_Y, for the set of calculations presented in Fig. 24, where the initial pore diameter was 30 μm.

The data in Fig. 32(a) correspond to a unit cell located outside (just below) the void layer with the fastest growth, indicated in Fig. 24(e) with a white arrow, and to a finite element outside (just below) the plastic localization band observed in Figs. 24(e') and 24(e"). The local void volume fraction f^{local}_{A} initially increases nearly linearly with the imposed axial displacement and subsequently saturates due to plastic deformation localization within the notch, see

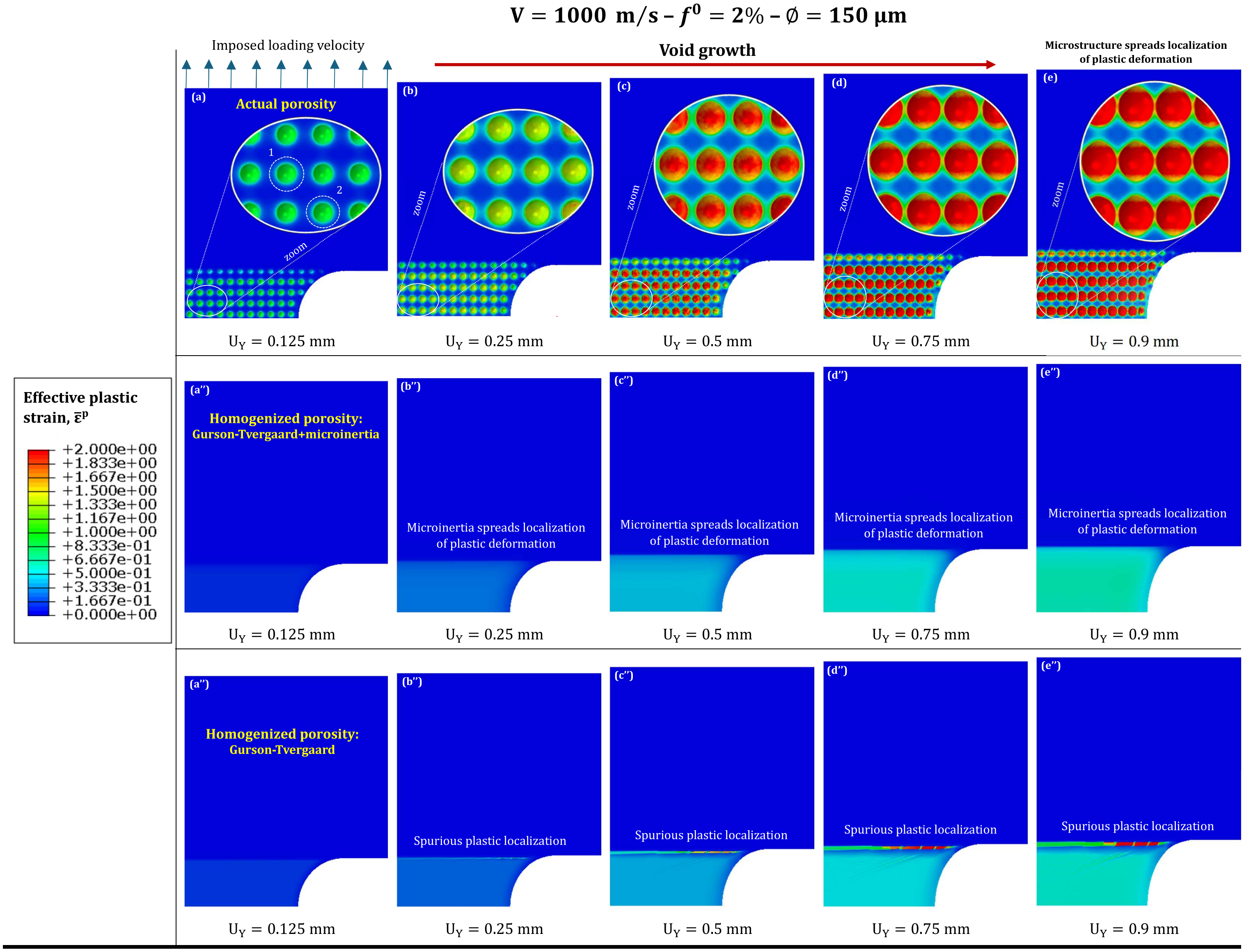

Figure 27: Contours of effective plastic strain $\bar{\varepsilon}^p$ for different imposed displacement values: (a)-(a')-(a") $U_Y = 0.125$ mm, (b)-(b')-(b") $U_Y = 0.25$ mm, (c)-(c')-(c") $U_Y = 0.5$ mm, (d)-(d') $U_Y = 0.75$ mm and (e)-(e') $U_Y = 1$ mm. Cross-section view at $Z = -0.223$ mm. The imposed loading velocity is $V = 1000$ m/s, the initial void volume fraction in the notched region is $f^0 = 2\%$ and the initial diameter of the voids is $\phi = 150$ μm. Subplots (a), ..., (e) correspond to calculation with actual pores and material modeled with von Mises plasticity. Subplots (a'), ..., (e') correspond to calculation with homogenized porosity and material modeled with Gurson-Tvergaard plasticity and microinertia effects. Subplots (a"), ..., (e") correspond to calculation with homogenized porosity and material modeled with Gurson-Tvergaard plasticity and without microinertia effects. For interpretation of the references to color in this figure legend, the reader is referred to the web version of this article.

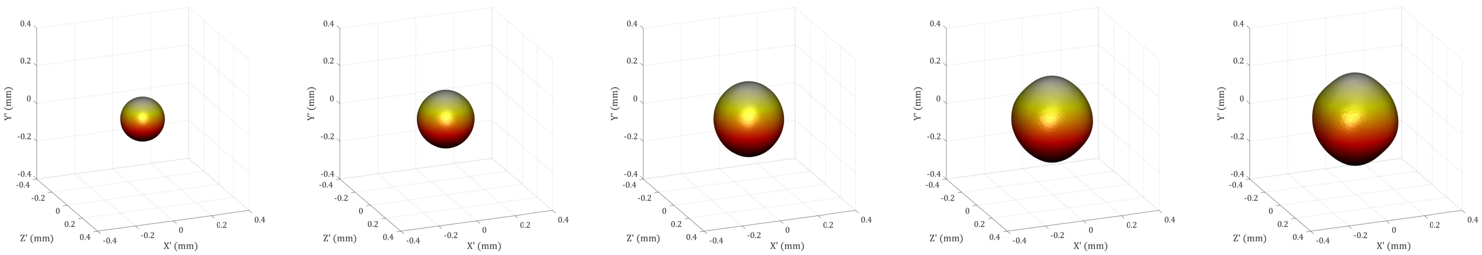

(a) (b) (c) (d) (e)

Figure 28: Finite element calculations for an imposed loading velocity $V = 1000$ m/s, initial void volume fraction in the notched region $f^0 = 2\%$ and initial diameter of the voids $\phi = 150$ μm. Results obtained from simulation with actual pores and material modeled with von Mises plasticity. 3D reconstructions of the surfaces of void 1 indicated in Fig. 27(a) for different imposed displacement values: (a) $U_Y = 0.125$ mm, (b) $U_Y = 0.25$ mm, (c) $U_Y = 0.5$ mm, (d) $U_Y = 0.75$ mm and (e) $U_Y = 0.9$ mm. The origin of the Cartesian coordinate system (X', Y', Z') is located at the center of the void, with X', Y' and Z' being parallel to the X, Y and Z axes, respectively.

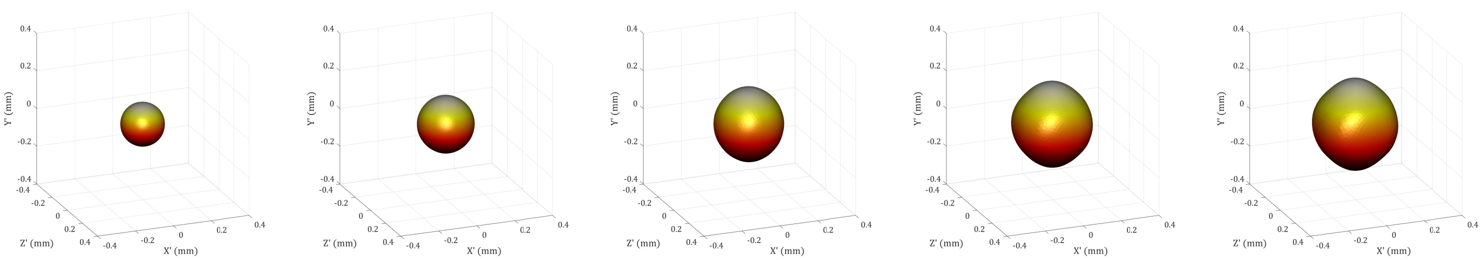

(a) (b) (c) (d) (e)

Figure 29: Finite element calculations for an imposed loading velocity $V = 1000$ m/s, initial void volume fraction in the notched region $f^0 = 2\%$ and initial diameter of the voids $\phi = 150$ μm. Results obtained from simulation with actual pores and material modeled with von Mises plasticity. 3D reconstructions of the surfaces of void 2 indicated in Fig. 27(a) for different imposed displacement values: (a) $U_Y = 0.125$ mm, (b) $U_Y = 0.25$ mm, (c) $U_Y = 0.5$ mm, (d) $U_Y = 0.75$ mm and (e) $U_Y = 0.9$ mm. The origin of the Cartesian coordinate system (X', Y', Z') is located at the center of the void, with X', Y' and Z' being parallel to the X, Y and Z axes, respectively.

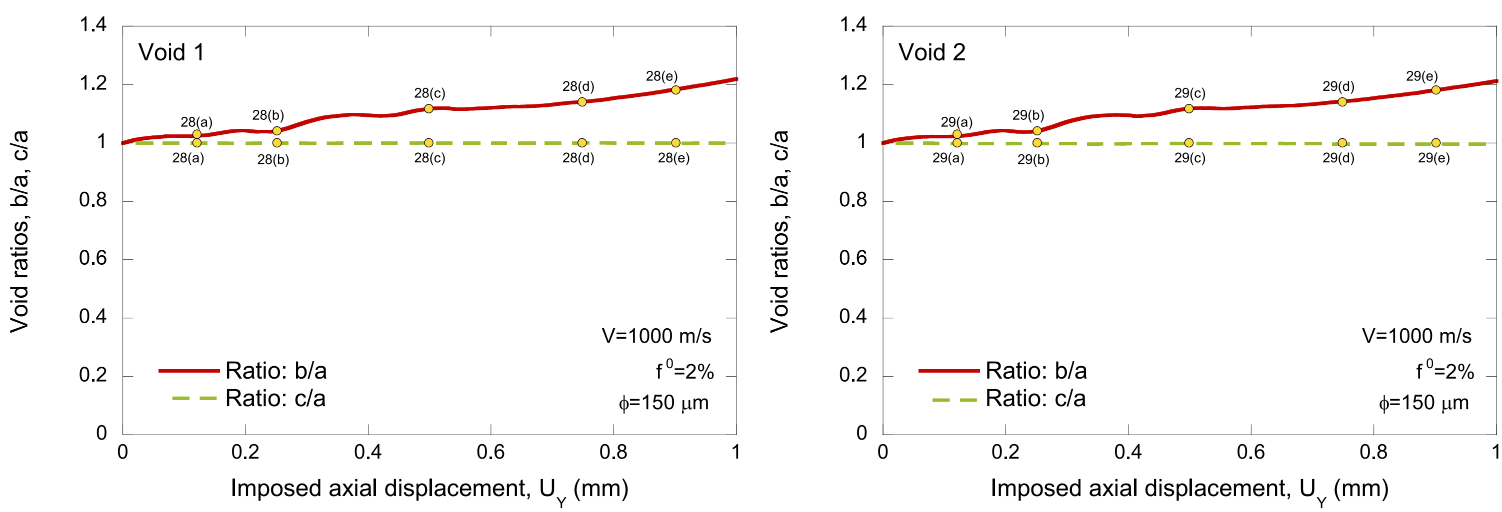

(a) (b)

Figure 30: Finite element calculations for an imposed loading velocity $V = 1000$ m/s, initial void volume fraction in the notched region $f^0 = 2\%$ and initial diameter of the voids $\phi = 150$ μm. Results obtained from simulation with actual pores and material modeled with von Mises plasticity. Evolution of the void ratios, $\frac{b}{a}$ and $\frac{c}{a}$, with the imposed displacement U_Y. (a) Void 1 indicated in Fig. 27(a). (b) Void 2 indicated in Fig. 27(a). The yellow markers represent the imposed displacement values used in the 3D reconstructions of the pores shown in Figs. 28 and 29.

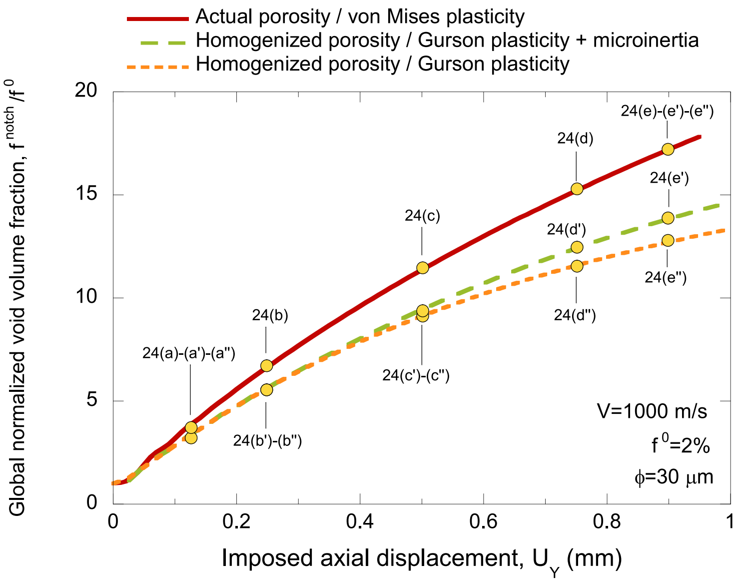

(a)

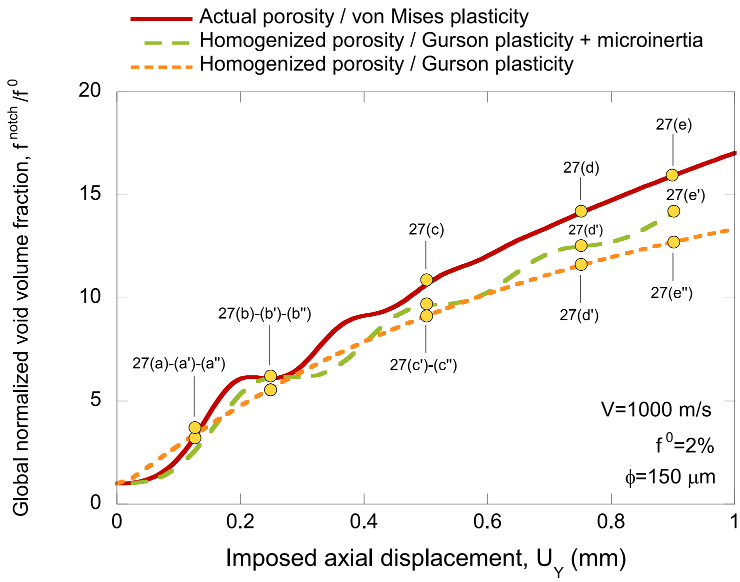

(b)

Figure 31: Comparison of results obtained with actual pores and material modeled with von Mises plasticity (red solid line), homogenized porosity and material modeled with Gurson-Tvergaard plasticity and microinertia effects (green dashed line) and homogenized porosity and material modeled with Gurson-Tvergaard plasticity and without microinertia effects (orange dotted line). The initial void volume fraction in the notched region is $f^0 = 2\%$ and the imposed loading velocity is $V = 1000$ m/s. Global normalized void volume fraction in the notch f^{notch}/f^0 versus imposed axial displacement U_Y. The initial diameter of the voids is: (a) $\phi = 30$ μm and (b) $\phi = 150$ μm. The yellow markers represent the imposed displacement values used in the contour plots of Figs. 24 and 27. For interpretation of the references to color in this figure legend, the reader is referred to the web version of this article.

contours of plastic strain 24(e)-(e')-(e"). The saturation of porosity outside the localization band occurs first in the simulation with discrete voids, followed by the standard (quasi-static) Gurson-Tvergaard model, and ultimately in the Gurson-Tvergaard model that incorporates microinertia effects.

The data in Fig. 32(b) correspond to a unit cell located inside the void layer with the fastest growth, indicated in Fig. 24(e) with a yellow arrow, and to a finite element inside the plastic localization band shown in Figs. 24(e') and 24(e"). The fastest porosity growth rate within the band is associated with the quasi-static Gurson-Tvergaard model (as in Fig. 23(b)). However, the differences in the results obtained for the void volume fraction f_B^{local} from the simulations with discrete voids, quasi-static Gurson-Tvergaard model, and homogenized porosity with microinertia are smaller than those obtained from the calculations with a void diameter of 50 μm in Fig. 23(b), as reducing the voids size favors rapid localization in the simulations with discrete voids and homogenized porosity incorporating microinertia.

Figure 33 shows the evolution of the local normalized void volume fraction, $f_{A,B}^{local}/f^0$, as a function of the imposed axial displacement, U_Y, for the set of calculations presented in Fig. 27. The difference from the data shown in Fig. 32 lies in the void diameter, which is five times larger $\phi = 150$ μm.

The results in Fig. 33(a) were obtained adjacent to (outside) the plastic localization band shown in Fig. 27(e"). Measurements for the simulations with discrete voids and homogenized porosity were taken from nearby locations. The calculation using the quasi-static Gurson-Tvergaard model predicts saturation of the void volume fraction f_A^{local}/f^0 due

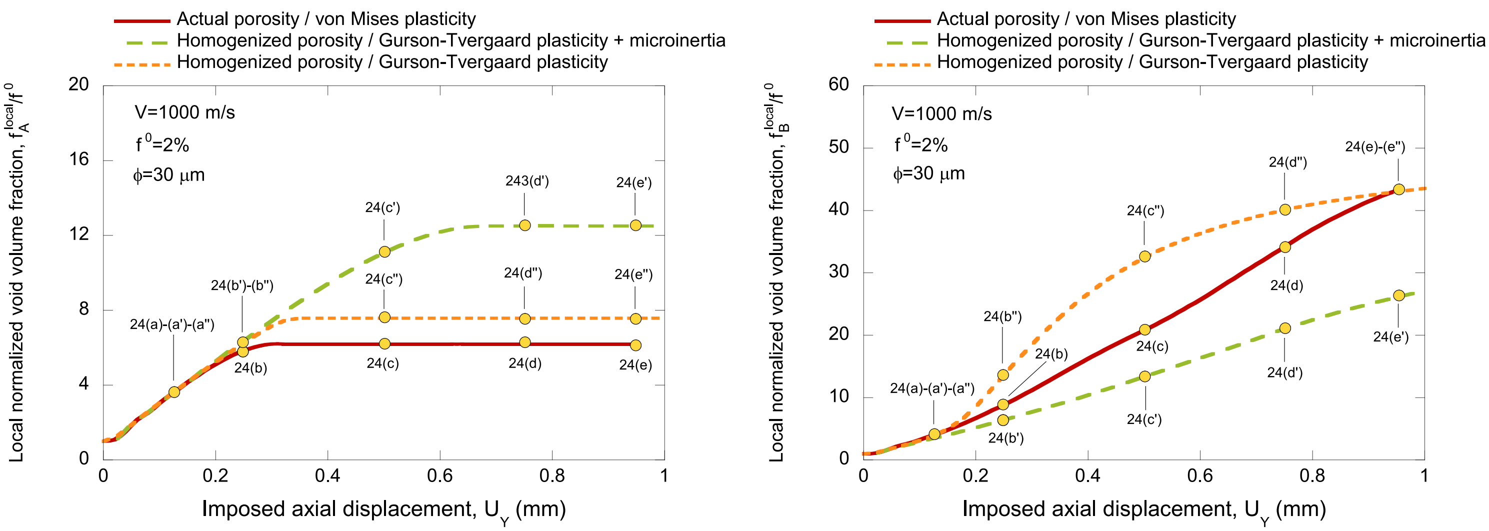

(a) (b)

Figure 32: Finite element calculations for an imposed loading velocity $V = 1000$ m/s, initial void volume fraction in the notched region $f^0 = 2\%$ and initial diameter of the voids $\phi = 30$ μm. Local normalized void volume fraction $f^{local}_{A,B}/f^0$ versus imposed axial displacement U_Y. The subscripts A and B correspond to measurements taken outside and inside the plastic localization band that forms within the notch. Comparison of results obtained with actual pores and material modeled with von Mises plasticity (red solid line), homogenized porosity and material modeled with Gurson-Tvergaard plasticity and microinertia effects (green dashed line) and homogenized porosity and material modeled with Gurson-Tvergaard plasticity and without microinertia effects (orange dotted line). (a) The center of the unit cell in the calculation with discrete voids is located at coordinates $X = 0.401$ mm, $Y = 0.579$ mm, and $Z = -0.044$ mm, while the finite element selected in the calculations with homogenized porosity is at coordinates $X = 2.102$ mm, $Y = 1.768$ mm, and $Z = -0.044$ mm. (b) The center of the unit cell in the calculation with discrete voids is located at coordinates $X = 0.401$ mm, $Y = 0.668$ mm, and $Z = -0.044$ mm, while the finite element selected in the calculations with homogenized porosity is at coordinates $X = 2.160$ mm, $Y = 1.850$ mm, and $Z = -0.044$ mm. The yellow markers represent the imposed displacement values used in the contour plots shown in Fig. 24. For interpretation of the references to color in this figure legend, the reader is referred to the web version of this article.

to plastic deformation localization within the notch. The results are similar to those presented in 32(a), as the predictions of the quasi-static Gurson-Tvergaard model are independent of void size. In contrast, the void volume fraction computed in simulations with discrete voids and with the Gurson-Tvergaard model incorporating microinertia effects shows a monotonic increase with the imposed displacement: in comparison to the results in 32(a), the increase in void size has prevented plastic flow localization in calculations accounting for microstructural inertia, see Fig. 27(a), ... (e) and 27(a'), ... (e').

The results in Fig. 33(b) were obtained inside the plastic localization band shown in Fig. 27(e"). Measurements for the simulations involving discrete voids and homogenized porosity were obtained from similar locations. The results obtained with quasi-static Gurson-Tvergaard plasticity closely resemble those shown in Fig. 32(b), as the predictions of the model do not depend on the voids size (notice the different scale used in Figs. 32(b) and 33(b)). In contrast, the rate of growth of the void volume fraction obtained from calculations with discrete voids and with homogenized porosity incorporating microinertia effects has significantly decreased with the increase in void size —compare Figs. 32(b) and 33(b). Additionally, the $f_B^{local}/f^0 - U_Y$ curves obtained from calculations with actual pores and with Gurson-Tvergaard plasticity accounting for microinertia effects are similar to the results presented in 33(a), as the increase in microstructural inertia with void size leads to uniform rise in porosity throughout the (whole) notch.

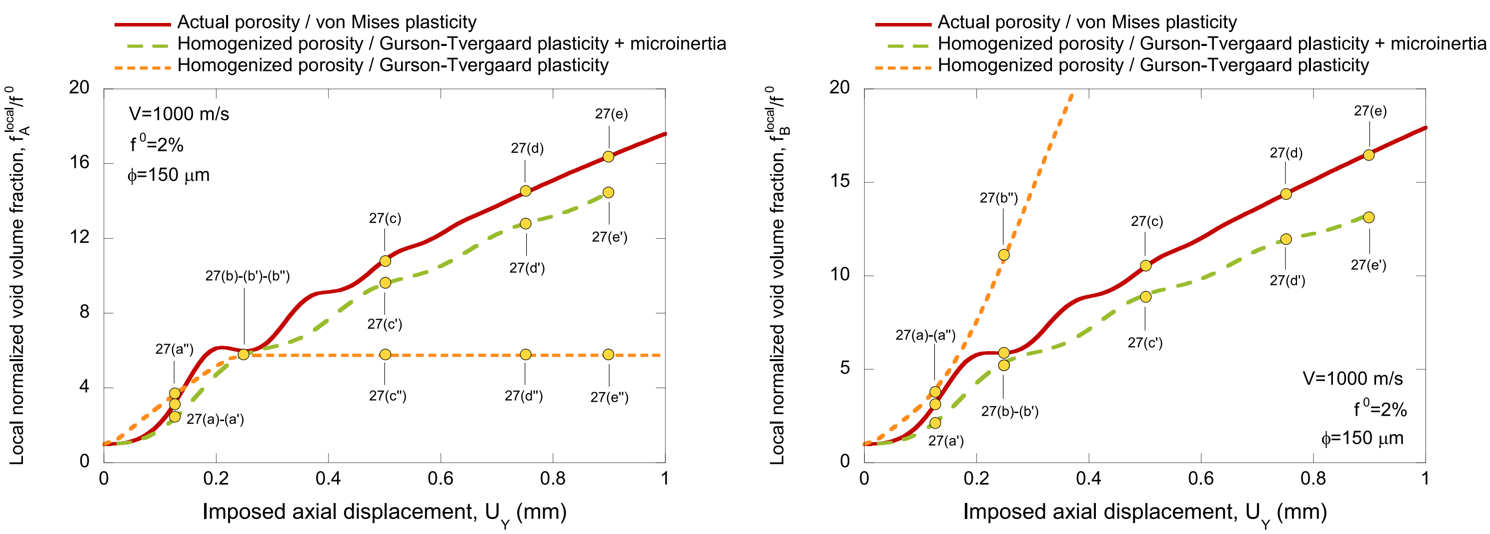

(a) (b)

Figure 33: Finite element calculations for an imposed loading velocity $V = 1000$ m/s, initial void volume fraction in the notched region $f^0 = 2\%$ and initial diameter of the voids $\phi = 150$ μm. Local normalized void volume fraction $f_{A,B}^{local}/f^0$ versus imposed axial displacement U_Y. The subscripts A and B correspond to measurements taken outside and inside the plastic localization band that forms within the notch. Comparison of results obtained with actual pores and material modeled with von Mises plasticity (red solid line), homogenized porosity and material modeled with Gurson-Tvergaard plasticity and microinertia effects (green dashed line) and homogenized porosity and material modeled with Gurson-Tvergaard plasticity and without microinertia effects (orange dotted line). (a) The center of the unit cell in the calculation with discrete voids is located at coordinates $X = 1.559$ mm, $Y = 1.113$ mm, and $Z = -0.223$ mm, while the finite element selected in the calculations with homogenized porosity is at coordinates $X = 1.528$ mm, $Y = 1.843$ mm, and $Z = -0.223$ mm. (b) The center of the unit cell in the calculation with discrete voids is located at coordinates $X = 1.559$ mm, $Y = 1.559$ mm, and $Z = -0.223$ mm, while the finite element selected in the calculations with homogenized porosity is at coordinates $X = 1.556$ mm, $Y = 1.907$ mm, and $Z = -0.223$ mm. The yellow markers represent the imposed displacement values used in the contour plots shown in Fig. 27. For interpretation of the references to color in this figure legend, the reader is referred to the web version of this article.

The results presented in Figs. 31, 32, and 33 indicate that, although the global void volume fraction within the notch may be greater for calculations performed with actual pores across the entire range of void diameters investigated (for the loading velocity 1000 m/s), increasing the void size enhances microstructural inertia, which slows down the development of plastic localization and reduces the local void volume fraction within the plastic localization band. In addition, increasing void size leads to greater discrepancies between the predictions of porosity growth within the plastic localization band derived from calculations that account for microstructural inertia and those obtained from simulations utilizing the quasi-static Gurson-Tvergaard model.

4.4. The effect of void volume fraction

Figure 34 shows contours of effective plastic strain from simulations with discrete pores and homogenized porosity including microinertia effects. The difference compared to Fig. 27 is that the void volume fraction has been reduced to 0.5%, while maintaining a void size of 150 μm. For the sake of brevity, the results for homogenized porosity without microinertia effects are not included.

Subplots 34(a), ..., (e) correspond to a calculation involving actual pores. The imposed displacements are 0.1, 0.2, 0.4, 0.6 and 0.75 mm, respectively. Compared to Fig. 27, as the void volume fraction is less, there are fewer pores, and the intervoid ligament is initially greater. All pores expand at a consistent rate and display nearly identical changes in shape and size as loading progresses. The significant inertia effects due to the large pore size and high applied velocity result in a uniform void growth within the notch. Fig. 35 presents the 3D reconstruction of void 1, which is enclosed within a dashed white line in subplot 34(a). The pore elongates in the loading direction, adopting an ellipsoidal shape. Fig. 38(a) shows the evolution of the ratios $\frac{b}{a}$ and $\frac{c}{a}$ with the imposed displacement. Note that $\frac{c}{a}$ remains approximately 1 throughout the entire loading process, showcasing uniform growth in both the X' and Z' directions. On the other hand, the ratio $\frac{b}{a}$ shows a continuous increase upon loading, similar to the calculation with initial void volume fraction of 2%, as seen in Fig. 30. This contrasts with the simulations shown in Figs. 17 and 24, where smaller pore sizes and larger void volume fractions resulted in more rapid initial growth of the voids perpendicular to the loading direction. These results underscore the impact of void spacing on the evolution of pore shape and size during loading.

Subplots 34(a'), ..., (e') include contour plots for a simulation performed with homogenized porosity and microinertia effects. Consistent with the results obtained from the calculation with discrete voids, the important inertia effects resulting from the large pore size and high applied velocity produce a uniform plastic strain field within the notch. No plastic localization is observed over the range of imposed displacements investigated.

Figure 36 shows contours of effective plastic strain from simulations with discrete pores and homogenized porosity including microinertia effects. The sole difference from Fig. 34 is the fourfold increase in void volume fraction to 4%, resulting in a significant reduction in the distance between pores.

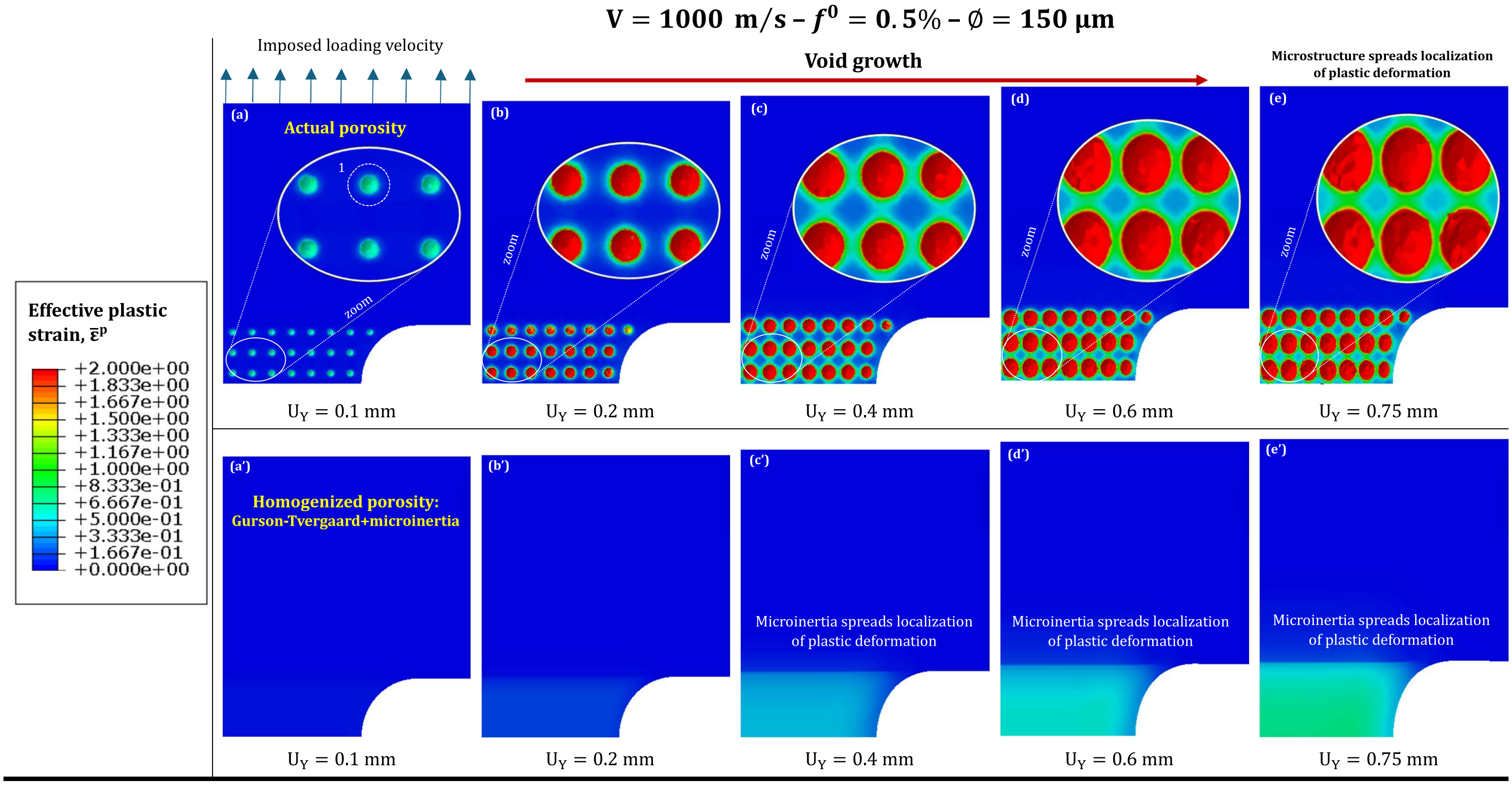

Figure 34: Contours of effective plastic strain $\bar{\varepsilon}^p$ for different imposed displacement values: (a)-(a')-(a") $U_Y = 0.1$ mm, (b)-(b')-(b") $U_Y = 0.2$ mm, (c)-(c')-(c") $U_Y = 0.4$ mm, (d)-(d')-(d") $U_Y = 0.6$ mm and (e)-(e')-(e") $U_Y = 0.75$ mm. Cross-section view at $Z = -0.353$ mm. The imposed loading velocity is $V = 1000$ m/s, the initial void volume fraction in the notched region is $f^0 = 0.5\%$ and the initial diameter of the voids is $\phi = 150$ μm. Subplots (a), ..., (e) correspond to calculation with actual pores and material modeled with von Mises plasticity. Subplots (a'), ..., (e') correspond to calculation with homogenized porosity and material modeled with Gurson-Tvergaard plasticity and microinertia effects. For interpretation of the references to color in this figure legend, the reader is referred to the web version of this article.

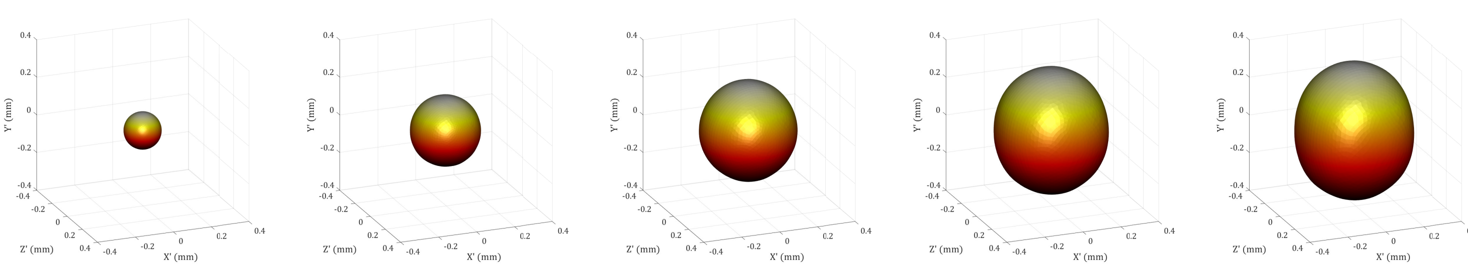

Figure 35: Finite element calculations for an imposed loading velocity $V = 1000$ m/s, initial void volume fraction in the notched region $f^0 = 0.5\%$ and initial diameter of the voids $\phi = 150$ μm. Results obtained from simulation with actual pores and material modeled with von Mises plasticity. 3D reconstructions of the surfaces of void 1 indicated in Fig. 34(a) for different imposed displacement values: (a) $U_Y = 0.1$ mm, (b) $U_Y = 0.2$ mm, (c) $U_Y = 0.4$ mm, (d) $U_Y = 0.6$ mm and (e) $U_Y = 0.75$ mm. The origin of the Cartesian coordinate system (X', Y', Z') is located at the center of the void, with X', Y' and Z' being parallel to the X, Y and Z axes, respectively.

Subplots 36(a), ..., (e) correspond to the calculation with discrete voids. Similar to the simulations with initial porosities of 0.5% and 2% shown in Figs. 34 and 27 (where the applied velocity and pore size are the same), the large size of the pores and the high loading velocity enhance inertial effects, resulting in a uniform void growth within the notch, with all pores maintaining the same shape. The difference compared to the calculations involving lower void volume fractions is that pores grow more slowly and coalesce earlier due to their closer spatial proximity. Fig. 37 presents the 3D reconstruction of void 1, which is enclosed within a dashed white circle in subplot 36(a). The evolution of the void shape is similar to that of the pores shown in Figs. 28 and 29 for $f^0 = 2\%$. Initially, the void elongates into an slightly ellipsoidal shape in the direction of the load, eventually developing a rhombohedral form characterized by flattened faces, resulting from the coalescence of pores located in planes where $Y =$ constant. The difference compared to simulations with void volume fractions of 0.5% and 2%, as shown in Figs. 35 and 28–29, is that for 4% void volume fraction, the pores exhibit reduced growth and a more distinct rhombohedral shape due to earlier coalescence. Fig. 38(b) shows the evolution of the ratios $\frac{b}{a}$ and $\frac{c}{a}$ with the imposed displacement. The ratio $\frac{c}{a}$ is nearly 1, showing that the grow of the voids along the X' and Z' directions is the same. The ratio $\frac{b}{a}$ also remains nearly constant at 1 throughout the entire deformation. The comparison with Figs. 30 and 38(a) illustrates that as the void volume fraction increases, pores expand less along the loading direction, resulting in a more pronounced rhombohedral shape. In contrast, decreasing the void volume fraction allows voids to deform *more freely*, leading to shapes elongated parallel to the loading direction and forming an ellipsoidal shape.

Subplots 36(a'), ..., (e') present contour plots for a simulation performed with homogenized porosity and microinertia effects. The plastic strain distribution within the notch is relatively uniform; however, for imposed displacements exceeding 0.5 mm, a diffuse localization band indicated with a white arrow in 36(a'), ..., (c') begins to form. In comparison to the results shown in 34(a'), ..., (c'), these findings indicate that an increased void volume fraction promotes plastic localization in simulations with homogenized porosity.

5. Summary and conclusions

This study analyzed the impact of microinertia on plastic localization, void growth, and coalescence in ductile porous materials subjected high strain rates. Finite element simulations were conducted on a flat, double-notched specimen under dynamic plane strain tension, employing three distinct modeling approaches: (1) discrete porosity within a matrix material described by von Mises plasticity; (2) homogenized porosity using standard quasi-static Gurson-Tvergaard plasticity and (3) homogenized porosity using Gurson-Tvergaard plasticity extended by Molinari and Mercier (2001) to account for microinertia effects. The porous microstructures used in the simulations were representative of additive manufactured metals, with initial void volume fractions between 0.5% and 4% and pore diameters from 30 μm to 150 μm. All calculations were performed under considering uniform void size distributions. The applied tensile velocities ranged from 100 m/s to 1000 m/s, resulting in strain rates between 10^5 s^{-1} and 10^6 s^{-1}, and stress triaxiality values from 4 to 30. The primary conclusions drawn from this research are as follows:

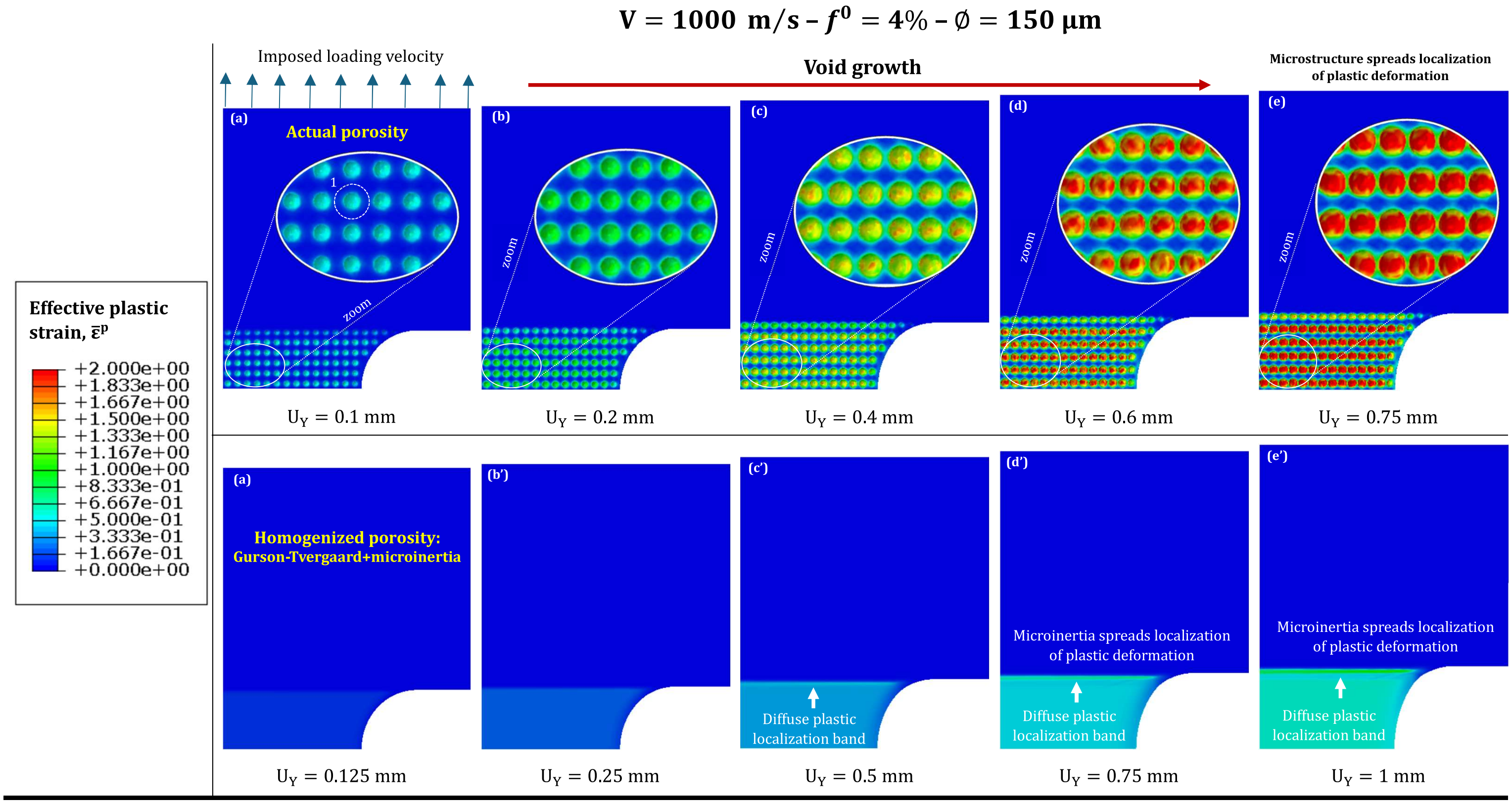

Figure 36: Contours of effective plastic strain $\bar{\varepsilon}^p$ for different imposed displacement values: (a)-(a')-(a") $U_Y = 0.1$ mm, (b)-(b')-(b") $U_Y = 0.2$ mm, (c)-(c')-(c") $U_Y = 0.4$ mm, (d)-(d')-(d") $U_Y = 0.6$ mm and (e)-(e')-(e") $U_Y = 0.75$ mm. Cross-section view at $Z = -0.177$ mm. The imposed loading velocity is $V = 1000$ m/s, the initial void volume fraction in the notched region is $f^0 = 4\%$ and the initial diameter of the voids is $\phi = 150$ μm. Subplots (a), ..., (e) correspond to calculation with actual pores and material modeled with von Mises plasticity. Subplots (a'), ..., (e') correspond to calculation with homogenized porosity and material modeled with Gurson-Tvergaard plasticity and microinertia effects. Subplots (a"), ..., (e") correspond to calculation with homogenized porosity and material modeled with Gurson-Tvergaard plasticity and without microinertia effects. For interpretation of the references to color in this figure legend, the reader is referred to the web version of this article.

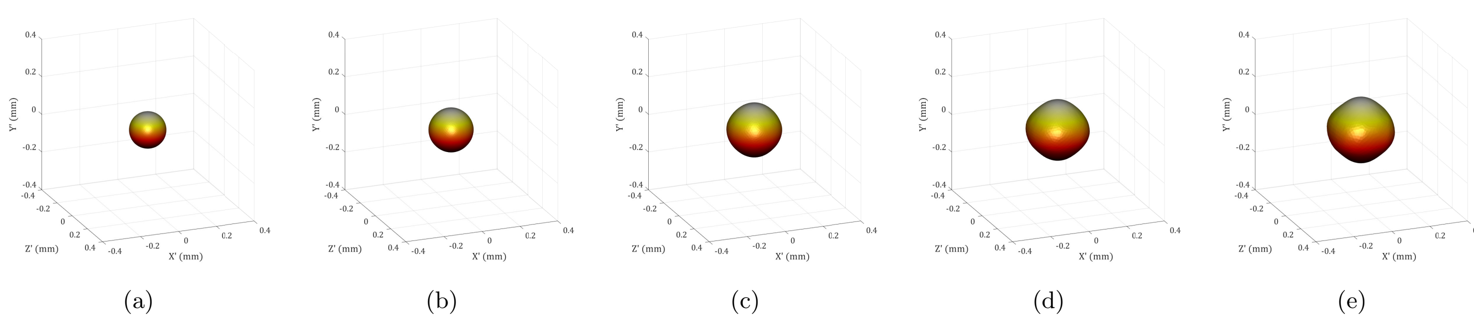

Figure 37: Finite element calculations for an imposed loading velocity $V = 1000$ m/s, initial void volume fraction in the notched region $f^0 = 4\%$ and initial diameter of the voids $\phi = 150$ μm. Results obtained from simulation with actual pores and material modeled with von Mises plasticity. 3D reconstructions of the surfaces of void 1 indicated in Fig. 36(a) for different imposed displacement values: (a) $U_Y = 0.1$ mm, (b) $U_Y = 0.2$ mm, (c) $U_Y = 0.4$ mm, (d) $U_Y = 0.5$ mm and (e) $U_Y = 0.75$ mm. The origin of the Cartesian coordinate system (X', Y', Z') is located at the center of the void, with X', Y' and Z' being parallel to the X, Y and Z axes, respectively.

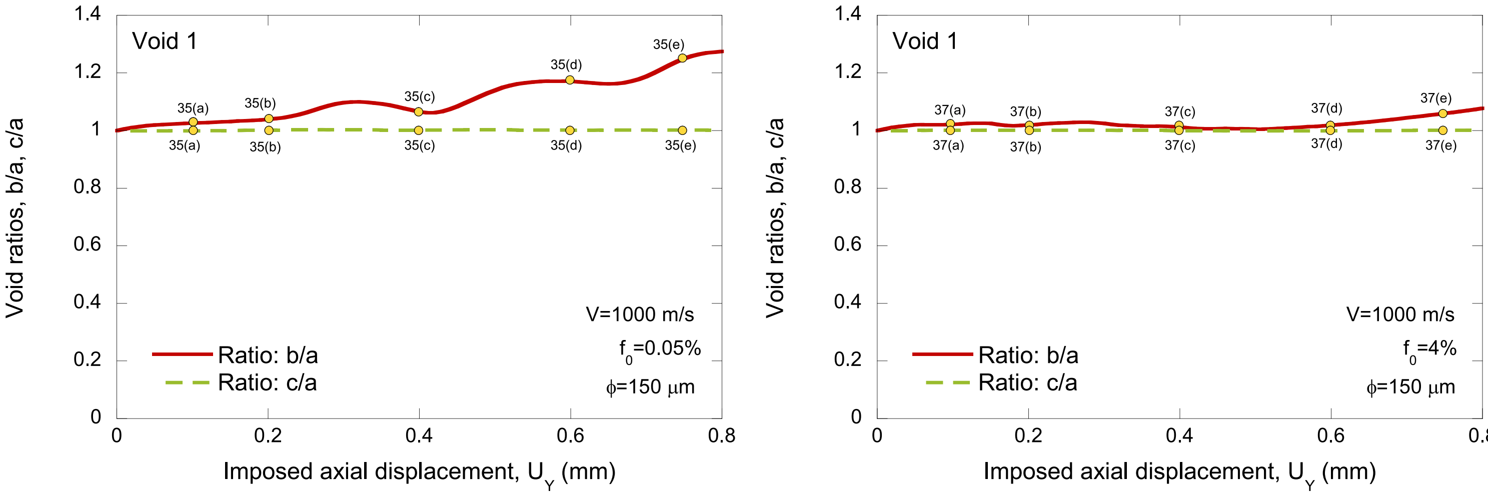

(a) (b)

Figure 38: Finite element calculations for an imposed loading velocity $V = 1000$ m/s and initial diameter of the voids $\phi = 150$ μm. Results obtained from simulation with actual pores and material modeled with von Mises plasticity. Evolution of the void ratios, $\frac{b}{a}$ and $\frac{c}{a}$, with the imposed displacement U_Y. (a) Void 1 indicated in Fig. 34(a) which corresponds to a calculation with initial void volume fraction in the notched region $f^0 = 0.5\%$. (b) Void 1 indicated in Fig. 36(a) which corresponds to a calculation with initial void volume fraction in the notched region $f^0 = 4\%$. The yellow markers represent the imposed displacement values used in the 3D reconstructions of the pores shown in Figs. 35 and 37.

- The explicit modeling of the porous microstructure regularizes plastic localization, eliminating mesh sensitivity in the finite element results by controlling localization size through void dimensions across the entire range of loading velocities examined.

- The calculations performed using the standard quasi-static Gurson-Tvergaard plasticity model result in spurious plastic behavior throughout the full spectrum of loading rates investigated, due to the formation of a localization band confined to a single layer of elements within the mesh discretization.

- The simulations employing the dynamic homogenization model proposed by Molinari and Mercier (2001) demonstrate the regularizing effect of microinertia, mitigating discretization sensitivity and producing mesh independent results for plastic localization (except for the lowest applied loading velocity).

- The computations incorporating discrete pores indicate that increasing loading rate and void size delays and slows down the formation and development of plastic localization. The same trend is observed using the dynamic homogenization approach of Molinari and Mercier (2001). In contrast, the simulations employing standard Gurson-Tvergaard plasticity do not account for the influence of void size on plastic localization and exhibit limited sensitivity to loading rate.

- In the simulations with discrete voids and homogenized porosity accounting for microinertia effects, plastic deformation is spread throughout the notch, resulting in a global porosity that exceeds that observed in analyses using the standard Gurson-Tvergaard model. In contrast, the earlier and more rapid localization observed in simulations employing standard Gurson-Tvergaard plasticity leads to higher local porosity values within the plastic localization band.

- The increased porosity growth within the localization band observed in the simulations using the standard Gurson-Tvergaard model becomes more pronounced compared to the results obtained with discrete voids and homogenized porosity accounting for microinertia effects as the loading rate and void size increase.

- The analysis of discrete pore simulations reveals that increases in loading rate and void size reduce the rate of void growth, resulting in uniform expansion and consistent shape evolution across all voids within the notch, in agreement with the predictions of the dynamic homogenization approach proposed by Molinari and Mercier (2001). Furthermore, decreases in loading rate and void size in the calculations involving discrete pores lead to heterogeneous distributions of void growth, along with variations in void shape and size, which contribute to earlier coalescence.

- In the calculations involving discrete pores, an increase in the initial void volume fraction decreases the distance between voids, restricting their growth and promoting coalescence for smaller values of the imposed displacement. This behavior consistent with the results obtained from the dynamic homogenization approach proposed by Molinari and Mercier (2001), which predicts that a higher initial void volume fraction promotes plastic localization.

The systematic comparison of calculations performed with explicitly resolved porosity and homogenized porosity demonstrates that accounting for microstructural inertia is critical for accurately capturing the influence of loading rate and void size on void growth and plastic localization in porous materials subjected to high strain rates. This underscores the effectiveness and advantages of the constitutive model introduced by Molinari and Mercier (2001) for simulating engineering problems involving porous ductile materials subjected to high velocity impacts. However, the dynamic homogenization approach used in this work does not account for coalescence, which presents an opportunity for improvement in the model of Molinari and Mercier (2001) to effectively capture the transition from ligament necking to direct impingement observed in discrete void calculations as the loading rate increases. Future computational research should also focus on investigating porous microstructures with varying void sizes, while also conducting experimental validation of the effects of microinertia on plastic localization and dynamic fracture using additive manufactured materials with characterized / controlled porous microstructures. These research efforts are currently underway.

Funding

The research leading to these results has received funding from the European Research Council (ERC) under the European Union's Horizon 2020 research and innovation programme. Project PURPOSE, grant agreement 758056.

This research has been supported by a 2021 Leonardo Grant for Researchers and Cultural Creators, BBVA Foundation. Project MIRROR, grant agreement IN[21]_ING_ING_0052.

Conflict of interest

The authors declare that they have no known competing financial interests or personal relationships that could have appeared to influence the work reported in this paper.

Author contributions

N Hosseini: Conceptualization; Data curation; Formal analysis; Investigation; Methodology; Software; Validation; Writing - review & editing. **T. Virazels**: Conceptualization; Data curation; Formal analysis; Investigation; Methodology; Software; Writing - review & editing. **N. Jacques**: Conceptualization; Formal analysis, Investigation; Methodology; Software; Writing - review & editing. **J. A. Rodríguez-Martínez**: Conceptualization; Formal analysis; Funding acquisition; Investigation; Methodology; Project administration; Resources; Supervision; Validation; Writing - original draft; Writing - review & editing.

References

ABAQUS/Explicit, 2019. Abaqus Explicit v6.16 User's Manual. version 6.16 ed., ABAQUS Inc., Richmond, USA.

Bao, Y., Wierzbicki, T., 2004. On fracture locus in the equivalent strain and stress triaxiality space. International Journal of Mechanical Sciences 46, 81–98.

Barber, C.B., Dobkin, D.P., Huhdanpaa, H., 1996. The quickhull algorithm for convex hulls. ACM Transactions on Mathematical Software (TOMS) 22, 469–483.

Barsoum, I., Faleskog, J., 2007. Rupture mechanisms in combined tension and shear—Experiments. International Journal of Solids and Structures 44, 1768–1786.

Beachem, C.D., 1963. An electron fractographic study of the influence of plastic strain conditions upon ductile rupture processes in metals. Transaction of the American Society of Metals 56.

Beese, A.M., Luo, M., Li, Y., Bai, Y., Wierzbicki, T., 2010. Partially coupled anisotropic fracture model for aluminum sheets. Engineering Fracture Mechanics 77, 1128–1152.

Benallal, A., Desmorat, R., Fournage, M., 2014. An assessment of the role of the third stress invariant in the Gurson approach for ductile fracture. European Journal of Mechanics A/Solids 47, 400–414.

Benzerga, A.A., Besson, J., 2001. Plastic potentials for anisotropic porous solids. European Journal of Mechanics A/Solids 20, 397–434.

Benzerga, A.A., Leblond, J.B., 2010. Ductile fracture by void growth to coalescence. Advances in Applied Mechanics 44, 169–305.

Benzerga, A.A., Leblond, J.B., Needleman, A., Tvergaard, V., 2016. Ductile failure modeling. International Journal of Fracture 201, 29–80.

Carroll, M.M., Holt, A., 1972. Static and dynamic pore-collapse relations for ductile porous materials. Journal of Applied Physics 43, 1626–1636.

Chu, C.C., Needleman, A., 1980. Void nucleation effects in biaxially stretched sheets. Journal of Engineering Materials and Technology 102, 249–256.

Czarnota, C., Jacques, N., Mercier, S., Molinari, A., 2008. Modelling of dynamic ductile fracture and application to the simulation of plate impact tests on tantalum. Journal of the Mechanics and Physics of Solids 56, 1624–1650.

Czarnota, C., Mercier, S., Molinari, A., 2006. Modelling of nucleation and void growth in dynamic pressure loading, application to spall test on tantalum. International Journal of Fracture 141, 177–194.

Czarnota, C., Molinari, A., Mercier, S., 2017. The structure of steady shock waves in porous metals. Journal of the Mechanics and Physics of Solids 107, 204–228.

Czarnota, C., Molinari, A., Mercier, S., 2020. Steady shock waves in porous metals: Viscosity and micro-inertia effects. International Journal of Plasticity 135, 102816.

Duva, J.M., 1986. A constitutive description of nonlinear materials containing voids. Mechanics of Materials 5, 317–329.

Ghahremaninezhad, A., Ravi-Chandar, K., 2011. Ductile failure in polycrystalline OFHC copper. International Journal of Solids and Structures 48, 3299–3311.

Ghahremaninezhad, A., Ravi-Chandar, K., 2012. Ductile failure behavior of polycrystalline Al 6061-T6. International Journal of Fracture 174, 177–202.

Ghahremaninezhad, A., Ravi-Chandar, K., 2013. Ductile failure behavior of polycrystalline Al 6061-T6 under shear dominant loading. International Journal of Fracture 180, 23–39.

Glennie, E., 1972. The dynamic growth of a void in a plastic material and an application to fracture. Journal of the Mechanics and Physics of Solids 20, 415–429.

Gologanu, M., Leblond, J.B., Perrin, G., Devaux, J., 1997. Recent extensions of Gurson's model for porous ductile metals. P. Suquet (Ed.), Continuum Micromechanics, Springer-Verlag, New York , 61–130.

Gross, A.J., Ravi-Chandar, K., 2016. On the deformation and failure of Al 6061-T6 at low triaxiality evaluated through in situ microscopy. International Journal of Fracture 200, 185–208.

Gărăjeu, M., Michel, J.C., Suquet, P., 2000. A micromechanical approach of damage in viscoplastic materials by evolution in size, shape and distribution of voids. Computer Methods in Applied Mechanics and Engineering 183, 223–246.

Gurland, J., Plateau, J., 1963. The mechanism of ductile rupture of metals containing inclusions. Technical Report. Brown University, Providence.

Gurson, A., 1977. Continuum theory of ductile rupture by void nucleation and growth. Part I: Yield criteria and flow rules for porous ductile media. ASME Journal of Engineering Materials and Technology 99, 2–15.

Haltom, S., Kyriakides, S., Ravi-Chandar, K., 2013. Ductile failure under combined shear and tension. International Journal of Solids and Structures 50, 1507–1522.

Hancock, J.W., Mackenzie, A.C., 1976. On the mechanisms of ductile failure in high-strength steels subjected to multi-axial stress-states. Journal of the Mechanics and Physics of Solids 24, 147–160.

Jackiewicz, J., 2011. Use of a modified Gurson model approach for the simulation of ductile fracture by growth and coalescence of microvoids under low, medium and high stress triaxiality loadings. Engineering Fracture Mechanics 78, 487–502.

Jacques, N., Czarnota, C., Mercier, S., Molinari, A., 2010. A micromechanical constitutive model for dynamic damage and fracture of ductile materials. International Journal of Fracture 162, 159–175.

Jacques, N., Mercier, S., Molinari, A., 2012a. Effects of microscale inertia on dynamic ductile crack growth. Journal of the Mechanics and Physics of Solids 60, 665–690.

Jacques, N., Mercier, S., Molinari, A., 2012b. Multiscale modelling of voided ductile solids with micro-inertia and application to dynamic crack propagation. Procedia IUTAM 3, 53–66.

Jacques, N., Mercier, S., Molinari, A., 2012c. Void coalescence in a porous solid under dynamic loading conditions. International Journal of Fracture 173, 203–213.

Jacques, N., Mercier, S., Molinari, A., 2015. A constitutive model for porous solids taking into account microscale inertia and progressive void nucleation. Mechanics of Materials 80, 311–323. Special Issue: IUTAM Symposium on Materials and Interfaces under High Strain Rate and Large Deformation.

Johnson, G.R., Cook, W.H., 1985. Fracture characteristics of three metals subjected to various strains, strain rates, temperatures and pressures. Engineering Fracture Mechanics 21, 31–48.

Kanel, G.I., 2010. Spall fracture: methodological aspects, mechanisms and governing factors. International Journal of Fracture 163, 173–191.

Kanel, G.I., Razorenov, S.V., Fortov, V.E., 1984. Kinetics of spallation rupture in the aluminum alloy AMg6M. Journal of Applied Mechanics and Technical Physics 25, 707–711.

Klöcker, H., Montheillet, F., 1991. Influence of flow rule and inertia on void growth in a rate sensitive material. Le Journal de Physique IV 1, C3–733.

Kong, X., Helfen, L., Hurst, M., Hänschke, D., Missoum-Benziane, D., Besson, J., Baumbach, T., Morgeneyer, T.F., 2022. 3d in situ study of damage during a 'shear to tension'load path change in an aluminium alloy. Acta Materialia 231, 117842.

Leblond, J.B., Perrin, G., Devaux, J., 1995. An improved Gurson-type model for hardenable ductile metals. European Journal of Mechanics A/Solids 14, 499–527.

Marvi-Mashhadi, M., Vaz-Romero, A., Sket, F., Rodríguez-Martínez, J.A., 2021. Finite element analysis to determine the role of porosity in dynamic localization and fragmentation: Application to porous microstructures obtained from additively manufactured materials. International Journal of Plasticity 143, 102999.

McClintock, F.A., 1968. A criterion for ductile fracture by the growth of holes. Journal of Applied Mechanics 35, 363–371.

von Mises, R., 1928. Mechanik der plastischen formänderung von kristallen. ZAMM-Journal of Applied Mathematics and Mechanics/Zeitschrift für Angewandte Mathematik und Mechanik 8, 161–185.

Molinari, A., Jacques, N., Mercier, S., Leblond, J.B., Benzerga, A.A., 2015. A micromechanical model for the dynamic behavior of porous media in the void coalescence stage. International Journal of Solids and Structures 71, 1–18.

Molinari, A., Mercier, S., 2001. Micromechanical modelling of porous materials under dynamic loading. Journal of the Mechanics and Physics of Solids 49, 1497–1516.

Monchiet, V., Bonnet, G., 2013. A Gurson-type model accounting fot void size effects. International Journal of Solids and Structures 50, 320–327.

Morgeneyer, T.F., Besson, J., 2011. Flat to slant ductile fracture transition: Tomography examination and simulations using shear-controlled void nucleation. Scripta Materialia 65, 1002–1005.

Morgeneyer, T.F., Taillandier-Thomas, T., Buljac, A., Helfen, L., Hild, F., 2016. On strain and damage interactions during tearing: 3D in situ measurements and simulations for a ductile alloy (AA2139-T3). Journal of the Mechanics and Physics of Solids 96, 550–571.

Morin, D., Hopperstad, O.S., Benallal, A., 2018. On the description of ductile fracture in metals by the strain localization theory. International Journal of Fracture 209, 27–51.

Nahshon, K., Hutchinson, J.W., 2008. Modification of the Gurson model for shear failure. European Journal of Mechanics A-Solid 27, 1–17.

Needleman, A., 1972. A numerical study of necking in circular cylindrical bar. Journal of the Mechanics and Physics of Solids 20, 111–127.

Needleman, A., 1991. The effect of material inertia on neck development. Topics in Plasticity. AM Press, Ann Arbor, MI , 151–160.

Needleman, A., Rice, J.R., 1978. Limits to ductility set by plastic flow localization, in: Mechanics of Sheet Metal Forming: Material Behavior and Deformation Analysis, pp. 237–267.

Needleman, A., Tvergaard, V.F., 1984. An analysis of ductile rupture in notched bars. Journal of the Mechanics and Physics of Solids 32, 461–490.

Nieto-Fuentes, J.C., Espinoza, J., Sket, F., Rodríguez-Martínez, J.A., 2023. High-velocity impact fragmentation of additively-manufactured metallic tubes. Journal of the Mechanics and Physics of Solids 174, 105248.

Nieto-Fuentes, J.C., Jacques, N., Marvi-Mashhadi, M., N'souglo, K.E., Rodríguez-Martínez, J.A., 2022. Modeling dynamic formability of porous ductile sheets subjected to biaxial stretching: Actual porosity versus homogenized porosity. International Journal of Plasticity 158, 103418.

Ortiz, M., Molinari, A., 1992. Effect of strain hardening and rate sensitivity on the dynamic growth of a void in a plastic material. Journal of Applied Mechanics 59, 48–53.

Rice, J.R., Tracey, D.M., 1969. On the ductile enlargement of voids in triaxial stress fields. Journal of the Mechanics and Physics of Solids 17, 201–217.

Rogers, H., 1960. The tensile fracture of ductile metals. Metal. Soc. AIME 218, 498–506.

Romanchenko, V.I., Stepanov, G.V., 1980. Dependence of the critical stresses on the loading time parameters during spall in copper, aluminum, and steel. Journal of Applied Mechanics and Technical Physics 21, 555–561.

Roth, C.C., Morgeneyer, T.F., Cheng, Y., Helfen, L., Mohr, D., 2018. Ductile damage mechanism under shear-dominated loading: In-situ tomography experiments on dual phase steel and localization analysis. International Journal of Plasticity 109, 169–192.

Roy, G., 2003. Vers une modélisation approfondie de l'endommagement ductile dynamique: investigation expérimentale d'une nuance de tantale et développements théoriques. Ph.D. thesis. Poitiers.

Scales, M., Tardif, N., Kyriakides, S., 2016. Ductile failure of aluminum alloy tubes under combined torsion and tension. International Journal of Solids and Structures 97-98, 116–128.

Stewart, J., Cazacu, O., 2011. Analytical yield criterion for an anisotropic material containing spherical voids and exhibiting tension–compression asymmetry. International Journal of Solids and Structures 48 (2), 357–373.

Tancogne-Dejean, T., Roth, C.C., Morgeneyer, T.F., Helfen, L., Mohr, D., 2021. Ductile damage of AA2024-T3 under shear loading: Mechanism analysis through in-situ laminography. Acta Materialia 205, 116556.

Tekoğlu, C., Hutchinson, J.W., Pardoen, T., 2015. On localization and void coalescence as a precursor to ductile fracture. Philosophical Transactions of the Royal Society A: Mathematical, Physical and Engineering Sciences 373, 20140121.

Thomason, P., 1985. A three-dimensional model for ductile fracture by the growth and coalescence of microvoids. Acta Metallurgica 33 (6), 1087–1095.

Tong, W., Ravichandran, G., 1993. Dynamic pore collapse in viscoplastic materials. Journal of Applied Physics 74, 2425–2435.

Tong, W., Ravichandran, G., 1995. Inertial Effects on Void Growth in Porous Viscoplastic Materials. Journal of Applied Mechanics 62, 633–639.

Tvergaard, V., 1982. On localization in ductile materials containing spherical voids. International Journal of Fracture 18, 237–252.

Tvergaard, V., Needleman, A., 1984. Analysis of the cup-cone fracture in a round tensile bar. Acta Metallurgica 32, 157–169.

Ueda, T., Helfen, L., Morgeneyer, T.F., 2014. In situ laminography study of three-dimensional individual void shape evolution at crack initiation and comparison with Gurson–Tvergaard–Needleman-type simulations. Acta Materialia 78, 254–270.

Vadillo, G., Reboul, J., Fernández-Sáez, J., 2016. A modified Gurson model to account for the influence of the Lode parameter at high triaxialities. European Journal of Mechanics-A/Solids 56, 31–44.

Vaz-Romero, A., Rodríguez-Martínez, J.A., Arias, A., 2015. The deterministic nature of the fracture location in the dynamic tensile testing of steel sheets. International Journal of Impact Engineering 86, 318–335.

Vaz-Romero, A., Rotbaum, Y., Rodríguez-Martínez, J.A., Rittel, D., 2016. Necking evolution in dynamically stretched bars: New experimental and computational insights. Journal of the Mechanics and Physics of Solids 91, 216–239.

Versino, D., Bronkhorst, C.A., 2018. A computationally efficient ductile damage model accounting for nucleation and micro-inertia at high triaxialities. Computer Methods in Applied Mechanics and Engineering 333, 395–420.

Vishnu, A.R., Marvi-Mashhadi, M., Nieto-Fuentes, J.C., Rodríguez-Martínez, J.A., 2022a. New insights into the role of porous microstructure on dynamic shear localization. International Journal of Plasticity 148, 103150.

Vishnu, A.R., Nieto-Fuentes, J.C., Rodríguez-Martínez, J.A., 2022b. Shear band formation in porous thin-walled tubes subjected to dynamic torsion. International Journal of Solids and Structures 252, 111837.

Vishnu, A.R., Vadillo, G., Rodríguez-Martínez, J.A., 2023. Void growth in ductile materials with realistic porous microstructures. International Journal of Plasticity 167, 103655.

Wang, Z.P., 1994a. Growth of voids in porous ductile materials at high strain rate. Journal of Applied Physics 76, 1535–1542.

Wang, Z.P., 1994b. Void growth and compaction relations for ductile porous materials under intense dynamic general loading conditions. International Journal of Solids and Structures 31, 2139–2150.

Wang, Z.P., 1997. Void-containing nonlinear materials subject to high-rate loading. Journal of Applied Physics 81, 7213–7227.

Wang, Z.P., Jiang, Q., 1997. A Yield Criterion for Porous Ductile Media at High Strain Rate. Journal of Applied Mechanics 64, 503–509.

Wen, J., Huang, Y., Hwang, K., Kiu, C., Li, M., 2005. The modified Gurson model accounting for the void size effect. International Journal of Plasticity 21, 381–395.

Wilkerson, J.W., 2017. On the micromechanics of void dynamics at extreme rates. International Journal of Plasticity 95, 21–42.

Wilkerson, J.W., Ramesh, K.T., 2014. A dynamic void growth model governed by dislocation kinetics. Journal of the Mechanics and Physics of Solids 70, 262–280.

Wright, T.W., Ramesh, K.T., 2008. Dynamic void nucleation and growth in solids: a self-consistent statistical theory. Journal of the Mechanics and Physics of Solids 56, 336–359.

Xue, Z., Vaziri, A., Hutchinson, J.W., 2008. Material aspects of dynamic neck retardation. Journal of the Mechanics and Physics of Solids 56, 93–113.